$$\begin{aligned}\dot{A}_1\cos\theta+\dot{B}_1\sin\theta=&\ \omega(t)A_1\sin\theta-\omega(t)B_1\cos\theta\\&-aA_1\cos\theta-aB_1\sin\theta\\&-\hat{\omega}(t)A_2\cos\theta-\hat{\omega}(t)B_2\sin\theta\\&+aA(t)\cos\theta\end{aligned}\tag{9.20}$$

$$\begin{aligned}\dot{A}_2\cos\theta+\dot{B}_2\sin\theta=&\ \omega(t)A_2\sin\theta-\omega(t)B_2\cos\theta\\&+\hat{\omega}(t)A_1\cos\theta-\hat{\omega}(t)B_1\sin\theta\end{aligned}\tag{9.21}$$

Because of the orthogonality of $\cos\theta$ and $\sin\theta$, it is possible to decompose these equations into:

$$\dot{A}_1=-\omega(t)B_1-aA_1-\hat{\omega}(t)A_2+aA(t)\tag{9.22}$$

$$\dot{B}_1=\omega(t)A_1-aB_1-\hat{\omega}(t)B_2\tag{9.23}$$

$$\dot{A}_2=-\omega(t)B_2+\hat{\omega}(t)A_1\tag{9.24}$$

$$\dot{B}_2=\omega(t)A_2+\hat{\omega}(t)B_1\,.\tag{9.25}$$

This can be expressed more compactly as

$$\dot{\tilde{\mathbf{x}}}=\underbrace{\begin{bmatrix}-a&-\omega(t)&-\hat{\omega}(t)&0\\ \omega(t)&-a&0&-\hat{\omega}(t)\\ \hat{\omega}(t)&0&0&-\omega(t)\\ 0&-\hat{\omega}(t)&\omega(t)&0\end{bmatrix}}_{\tilde{\mathbf{A}}(t)}\tilde{\mathbf{x}}+\underbrace{\begin{bmatrix}a\\0\\0\\0\end{bmatrix}}_{\tilde{\mathbf{b}}}\tilde{u}(t)\tag{9.26}$$

where $\tilde{\mathbf{x}}=\begin{bmatrix}A_1 & B_1 & A_2 & B_2\end{bmatrix}^T$ and $\tilde{u}(t)=A(t)$. Thus, the equilibrium trajectory of (9.11) is described by (8) and (9) where the coefficients evolve according to (9.26).

9.3.2.1.1. Global Exponential Stability of Equilibrium Trajectory System

The stability of the equilibrium trajectory system can be understood by consideration of the following Lyapunov function:

$$\tilde{\mathbf{V}}(\tilde{\mathbf{x}})=\tilde{\mathbf{x}}^T\underbrace{\begin{bmatrix}1&0&\tilde{k}&0\\ 0&1&0&\tilde{k}\\ \tilde{k}&0&1&0\\ 0&\tilde{k}&0&1\end{bmatrix}}_{\tilde{\mathbf{P}}}\tilde{\mathbf{x}}\tag{9.27}$$

where

$$\tilde{k}=4\alpha a\min_{\hat{\omega}\in[\hat{\omega}_{\min},\hat{\omega}_{\max}]}\frac{\hat{\omega}}{4\hat{\omega}^2+a^2}\tag{9.28}$$

and $\alpha \in [0,1]$. The nature of the objective function in (9.28) is such that the minimum occurs at one of the endpoints. Also, $\tilde{k} > 0$. Suppose $\exists\ \hat{\omega}$ such that

$$\frac{4a\hat{\omega}}{4\hat{\omega}^2 + a^2} > 1 \tag{9.29}$$

Then,

$$4a\hat{\omega} > 4\hat{\omega}^2 + a^2 \tag{9.30}$$

$$0 > 4\hat{\omega}^2 - 4a\hat{\omega} + a^2 \tag{9.31}$$

$$0 > (2\hat{\omega} - a)^2 \tag{9.32}$$

which is impossible. Thus, $\tilde{k} < 1$. The positive definiteness of symmetric $\tilde{\mathbf{P}}$ can be assessed through its eigenvalues, which are $1 \pm \tilde{k}$, each with multiplicity two. Each of these are positive for $\tilde{k} \in [0,1]$. Therefore, $\tilde{\mathbf{V}}(.)$ is a positive-definite function. Furthermore,

$$(1-\tilde{k})\|\tilde{\mathbf{x}}\|_2^2 \le \mathbf{V}(\tilde{\mathbf{x}}) \le (1+\tilde{k})\|\tilde{\mathbf{x}}\|_2^2 \tag{9.33}$$

The stability of the unforced equilibrium trajectory system ($\tilde{u}(t)=0$) is assessed by examining the time derivative of the Lyapunov function $\tilde{\mathbf{V}}(.)$:

$$\dot{\tilde{\mathbf{V}}} = \tilde{\mathbf{x}}^T \tilde{\mathbf{A}}^T(t)\tilde{\mathbf{P}}\tilde{\mathbf{x}} + \tilde{\mathbf{x}}^T \tilde{\mathbf{P}}\tilde{\mathbf{A}}(t)\tilde{\mathbf{x}} \tag{9.34}$$

$$\dot{\tilde{\mathbf{V}}} = -\tilde{\mathbf{x}}^T \tilde{\mathbf{Q}}(t)\tilde{\mathbf{x}} \tag{9.35}$$

where

$$\tilde{\mathbf{Q}}(t) = -\left(\tilde{\mathbf{A}}^T(t)\tilde{\mathbf{P}} + \tilde{\mathbf{P}}\tilde{\mathbf{A}}(t)\right) \tag{9.36}$$

$$\tilde{\mathbf{Q}}(t) = \begin{bmatrix} 2a - 2\tilde{k}\hat{\omega}(t) & 0 & a\tilde{k} & 0 \\ 0 & 2a - 2\tilde{k}\hat{\omega}(t) & 0 & a\tilde{k} \\ a\tilde{k} & 0 & 2\tilde{k}\hat{\omega}(t) & 0 \\ 0 & a\tilde{k} & 0 & 2\tilde{k}\hat{\omega}(t) \end{bmatrix} \tag{9.37}$$

The positive definiteness of symmetric $\tilde{\mathbf{Q}}(t)$ can be assessed through its eigenvalues, which are $a \pm \sqrt{a^2 + 4\tilde{k}^2\hat{\omega}^2(t) + a^2\tilde{k}^2 - 4a\tilde{k}\hat{\omega}(t)}$, each with multiplicity two. Each of these is positive for $4\tilde{k}^2\hat{\omega}^2(t) + a^2\tilde{k}^2 - 4a\tilde{k}\hat{\omega}(t) < 0$. Suppose $\exists \hat{\omega} \in [\hat{\omega}_{\min}, \hat{\omega}_{\max}]$ such that $4\tilde{k}^2\hat{\omega}^2(t) + a^2\tilde{k}^2 - 4a\tilde{k}\hat{\omega}(t) \ge 0$. Then,

$$\left(4\tilde{k}\hat{\omega}^2 + a^2\tilde{k} - 4a\hat{\omega}\right)\tilde{k} \ge 0 \tag{9.38}$$

$$4\tilde{k}\hat{\omega}^2 + a^2\tilde{k} - 4a\hat{\omega} \geq 0 \tag{9.39}$$

$$4\tilde{k}\hat{\omega}^2 + a^2\tilde{k} \geq 4a\hat{\omega} \tag{9.40}$$

$$\left(4\hat{\omega}^2 + a^2\right)\tilde{k} \geq 4a\hat{\omega} \tag{9.41}$$

$$\tilde{k} \geq \frac{4a\hat{\omega}}{4\hat{\omega}^2 + a^2} \tag{9.42}$$

which is impossible over $[\hat{\omega}_{\min}, \hat{\omega}_{\max}]$ by (20). Therefore, $\tilde{\mathbf{Q}}(t)$ is positive definite. Further, let

$$\tilde{\lambda} = a - \sqrt{a^2 + \max_{\hat{\omega}\in[\hat{\omega}_{\min},\hat{\omega}_{\max}]} \left(4\tilde{k}\hat{\omega}^2 + a^2\tilde{k} - 4a\hat{\omega}\right)\tilde{k}} \tag{9.43}$$

The nature of the objective function in (35) is such that the maximum occurs at one of the endpoints. From above, $\tilde{\lambda}>0$ is a lower bound on the eigenvalues of $\tilde{\mathbf{Q}}(t)$ and

$$\dot{\tilde{\mathbf{V}}} = -\tilde{\mathbf{x}}^T\tilde{\mathbf{Q}}(t)\tilde{\mathbf{x}} \leq -\tilde{\lambda}\|\tilde{\mathbf{x}}\|_2^2. \tag{9.44}$$

The global exponential stability of the equilibrium trajectory system is demonstrated:

$$\dot{\tilde{\mathbf{V}}} \leq -\tilde{\lambda}\|\tilde{\mathbf{x}}\|_2^2 \tag{9.45}$$

$$\dot{\tilde{\mathbf{V}}} \leq \frac{-\tilde{\lambda}}{1+\tilde{k}}\tilde{\mathbf{V}}(\tilde{\mathbf{x}}) \tag{9.46}$$

$$\tilde{\mathbf{V}}(\tilde{\mathbf{x}}(t)) \leq \tilde{\mathbf{V}}(\tilde{\mathbf{x}}(t_0))e^{\frac{-\tilde{\lambda}}{1+\tilde{k}}(t-t_0)} \tag{9.47}$$

$$\|\tilde{\mathbf{x}}(t)\|_2 \leq \sqrt{\frac{\tilde{\mathbf{V}}(\tilde{\mathbf{x}}(t))}{1-\tilde{k}}} \tag{9.48}$$

$$\|\tilde{\mathbf{x}}(t)\|_2 \leq \sqrt{\frac{\tilde{\mathbf{V}}(\tilde{\mathbf{x}}(t))}{1-\tilde{k}}e^{\frac{-\tilde{\lambda}}{1+\tilde{k}}(t-t_0)}} \tag{9.49}$$

$$\|\tilde{\mathbf{x}}(t)\|_2 \leq \sqrt{\frac{(1+\tilde{k})\|\tilde{\mathbf{x}}(t_0)\|_2^2}{1-\tilde{k}}e^{\frac{-\tilde{\lambda}}{1+\tilde{k}}(t-t_0)}} \tag{9.50}$$

$$\|\tilde{\mathbf{x}}(t)\|_2 \leq \sqrt{\frac{1+\tilde{k}}{1-\tilde{k}}}\|\tilde{\mathbf{x}}(t_0)\|_2 e^{\frac{-\tilde{\lambda}}{2(1+\tilde{k})}(t-t_0)} \tag{9.51}$$

9.3.2.2. Dynamics about Equilibrium Trajectory

Having established the equilibrium trajectory of the tracking filter above, it is possible to examine the filter's dynamics about the equilibrium trajectory. Let $\mathbf{z} = \mathbf{x} - \mathbf{x}^*$ where $x^* = [x_1^* \quad x_2^*]^T$. Also, observe that $v(t) = u(t) - u^*(t)$. Then,

$$\dot{\mathbf{z}} = \dot{\mathbf{x}} - \dot{\mathbf{x}}^* = \mathbf{A}(t)\mathbf{z} + \mathbf{b}v(t). \tag{9.52}$$

This error system describes the evolution of the state variable errors with respect to the equilibrium trajectory

8.3.2.2.1. Global Exponential Stability of Error System

The stability of the error system can be understood by consideration of the following Lyapunov function:

$$\mathbf{V}(\mathbf{z}) = \mathbf{z}^T \underbrace{\begin{bmatrix} k & 1 \\ 1 & k \end{bmatrix}}_{\mathbf{P}} \mathbf{z} \tag{9.53}$$

where

$$k = \max_{\hat{\omega} \in [\hat{\omega}_{\min}, \hat{\omega}_{\max}]} \left(\frac{a}{4\hat{\omega}} + \frac{\hat{\omega}}{a} \right) + \varepsilon \tag{9.54}$$

and $\varepsilon > 0$. The nature of the objective function in (46) is such that the maximum occurs at one of the endpoints. Suppose $\exists \hat{\omega} > 0$ such that

$$\frac{a}{4\hat{\omega}} + \frac{\hat{\omega}}{a} < 1. \tag{9.54}$$

Then,

$$a^2 + 4\hat{\omega}^2 < 4a\hat{\omega} \tag{9.55}$$

$$a^2 - 4a\hat{\omega} + 4\hat{\omega}^2 < 0 \tag{9.56}$$

$$(a - 2\hat{\omega})^2 < 0 \tag{9.57}$$

which is impossible. Thus, $k > 1$. The positive definiteness of symmetric P can be assessed with Sylvester's criterion by examining its leading principal minors, which are k and $k^2 - 1$. Each of these are positive for $k > 1$. Therefore, $\mathbf{V}(.)$ is a positive-definite function. The eigenvalues of $\mathbf{P}$ are $k \pm 1$ so

$$(k-1)\|\mathbf{z}\|_2^2 \le \mathbf{V}(\mathbf{z}) \le (k+1)\|\mathbf{z}\|_2^2 \tag{9.58}$$

The stability of the undisturbed error system ($v(t)=0$) is assessed by examining the time derivative of the Lyapunov function $\mathbf{V}(.)$:

$$\dot{\mathbf{V}} = \mathbf{z}^T \mathbf{A}^T(t)\mathbf{P}\mathbf{z} + \mathbf{z}^T \mathbf{P}\mathbf{A}(t)\mathbf{z} \tag{9.59}$$

$$\dot{\mathbf{V}} = \mathbf{z}^T \mathbf{Q}(t)\mathbf{z} \tag{9.60}$$

where

$$\mathbf{Q}(t) = -(\mathbf{A}^T(t)\mathbf{P} + \mathbf{P}\mathbf{A}(t)) \tag{9.61}$$

$$\mathbf{Q}(t) = \begin{bmatrix} 2ak - 2\hat{\omega} & a \\ a & 2\hat{\omega} \end{bmatrix}. \tag{9.62}$$

The positive definiteness of symmetric $\mathbf{Q}(t)$ can be assessed with Sylvester's criterion by examining its leading principal minors, which are $2ak - 2\hat{\omega}$ and $-a^2 + 4ak\hat{\omega} - 4\hat{\omega}^2$. Suppose $\exists \hat{\omega} \in [\hat{\omega}_{\min}, \hat{\omega}_{\max}]$ such that

$$2ak - 2\hat{\omega} \le 0 \tag{9.63}$$

Then,

$$2a\left(\frac{a}{4\hat{\omega}} + \frac{\hat{\omega}}{a}\right) - 2\hat{\omega} < 0 \tag{9.64}$$

$$\frac{a^2}{2\hat{\omega}} < 0 \tag{9.65}$$

which is impossible. Thus, the first leading principal minor of $\mathbf{Q}(t)$ is positive for $\hat{\omega} \in [\hat{\omega}_{\min}, \hat{\omega}_{\max}]$. Suppose $\exists \hat{\omega} \in [\hat{\omega}_{\min}, \hat{\omega}_{\max}]$ such that

$$-a^2 + 4ak\hat{\omega} - 4\hat{\omega}^2 \le 0. \tag{9.66}$$

Then,

$$-a^2 + 4a\left(\frac{a}{4\hat{\omega}} + \frac{\hat{\omega}}{a}\right)\hat{\omega} - 4\hat{\omega}^2 \le 0 \tag{9.67}$$

$$-a^2 + a^2 + 4\hat{\omega}^2 - 4\hat{\omega}^2 < 0 \tag{9.68}$$

$$0 < 0 \tag{9.69}$$

which is impossible. Thus, the second leading principal minor of Q(t) is positive for $\hat{\omega} \in [\hat{\omega}_{\min}, \hat{\omega}_{\max}]$, and $\mathbf{Q}(t)$ is positive definite. The eigenvalues of $\mathbf{Q}(t)$ are $ak \pm \sqrt{a^2k^2 + a^2 - 4ak\hat{\omega} + 4\hat{\omega}^2}$. Let

$$\lambda = ak - \sqrt{a^2k^2 + \max_{\hat{\omega} \in [\hat{\omega}_{\min}, \hat{\omega}_{\max}]} \left(a^2 - 4ak\hat{\omega} + 4\hat{\omega}^2\right)}. \tag{9.70}$$

The nature of the objective function in (63) is such that the maximum occurs at one of the endpoints. From above, $\lambda > 0$ is a lower bound on the eigenvalues of Q(t) and

$$\dot{\mathbf{V}} = -\mathbf{z}^T \mathbf{Q}(t)\mathbf{z} \le -\lambda \|\mathbf{z}\|_2^2. \tag{9.71}$$

The global exponential stability of the error system is demonstrated:

$$\dot{\mathbf{V}} \le -\lambda \|\mathbf{z}\|_2^2 \tag{9.72}$$

$$\dot{\mathbf{V}} \le \frac{-\lambda}{k+1}\mathbf{V}(\mathbf{z}) \tag{9.73}$$

$$\mathbf{V}(\mathbf{z}(t)) \le \mathbf{V}(\mathbf{z}(t_0))e^{\frac{-\lambda}{k+1}(t-t_0)} \tag{9.74}$$

$$\|\mathbf{z}(t)\|_2 \le \sqrt{\frac{\mathbf{V}(\mathbf{z}(t))}{k-1}} \tag{9.75}$$

$$\|\mathbf{z}(t)\|_2 \le \sqrt{\frac{\mathbf{V}(\mathbf{z}(t_0))}{k-1}e^{\frac{-\lambda}{k+1}(t-t_0)}} \tag{9.76}$$

$$\|\mathbf{z}(t)\|_2 \le \sqrt{\frac{(k+1)\|\mathbf{z}(t_0)\|_2^2}{k-1}e^{\frac{-\lambda}{k+1}(t-t_0)}} \tag{9.77}$$

$$\|\mathbf{z}(t)\|_2 \le \sqrt{\frac{k+1}{k-1}}\|\mathbf{z}(t_0)\|_2 e^{\frac{-\lambda}{2(k+1)}(t-t_0)} \tag{9.78}$$

I don't see why we need 9.3.2.1. Simply show (9.16 & 9.17) are ≤ steady-state solution to (9.14) with (9.1c) as an input. This section then shows stability.

9.3.3. Selection of parameter "*a*"

The only numerical constraint defined for a is that it has to be greater than 0. Besides that, any other constraint is qualitative in nature. The trade-off that has to occur is between the selectivity of the filter and the initialization or rapidness with which state x_1 will reach steady-state. Both, selectivity and initialization are application dependent. The application for this dissertation is tracking the 3rd harmonic of the current sourced by the CMV of a drive in a system with HRG grounding. The sampling time for the tracking filter implementation is fixed at 250 μs. Then, the maximum frequency to be tracked is determined to be 400 Hz (i.e., the maximum operating frequency of the inverter considered is 133.3 Hz). This ensures that at least 10 samples will be used to reconstruct the tracked signal. At 4 KHz carrier frequency, as discussed in Chapter 5, the overlap between sidebands of the carrier and frequencies 1/10 the carrier is negligible. Therefore, the only harmonic that requires to be filtered out is the 9th of the current sourced by the inverter CMV. For the lower bound, it is easy to demonstrate that the tracking filter falls apart if the required signal to be tracked is a constant. Without further discussion, no inverter operating frequency below 1 Hz is considered. The frequency to be tracked for this limit case is 3 Hz while the frequency that requires filtering is 9 Hz.

Without the loss of generality, to quantify initialization of state x_1, (9.4) can be solved for $\hat{\omega}(t) = \omega_0$. This is presented in (9.79). If the input, u, is defined as $u(t) = A\cos(\omega_0 t + \phi)$, the response in time of the resonator to this input can be found as in (9.79). The first term matches the input. The second term is a transient whose decay rate depends on a. The more selective the resonator, the smaller a is set. The smaller a is set, the longer the transient term takes to decay.

This comes from where?

$$y(t) = x_1(t) = A\left(\begin{array}{l}\cos(\omega_0 t + \phi) + \\ -e^{-\frac{at}{2}}\cos(\phi)\left(\cosh\left(t\sqrt{\frac{a^2}{4} - \omega_0^2}\right) - \frac{\sinh\left(t\sqrt{\frac{a^2}{4} - \omega_0^2}\right)\left(\frac{a}{2} + \omega_0\tan(\phi)\right)}{\sqrt{\frac{a^2}{4} - \omega_0^2}}\right)\end{array}\right) \quad (9.79)$$

defined as?

It can be demonstrated that the positive envelope of (9.79) is monotonically increasing. Then, steady-state has been defined as the moment in which x_1 equals 99% of the amplitude of the input. The attenuation can be quantified for the same case, $\hat{\omega}(t) = \omega_0$.

In Table 9.1, the initialization time and the attenuation factor are given for several values of the parameter a. The resonant frequency has no attenuation (i.e., attenuation factor equals 1). When the input is filtered, the amplitude of the 9th harmonic with respect to the 3rd harmonic is given as the relative amplitude of the 9th harmonic to the 3rd harmonic times the attenuation factor.

From (4.14), the 9th harmonic has an amplitude of 1/10 the amplitude of the 3rd harmonic of the CMV. If the amplitude of the 3rd harmonic is normalized to 1, when filtered, the amplitude of the 9th harmonic corresponds to the last column of Table 9.1.

For this dissertation, the criterion to choose the parameter a is no more than 6% of 9th harmonic present in the filtered output and no more than 1 s allowed for initialization time for operating frequencies of the inverter equal or greater than 1 Hz. This is an engineering design criterion that could be tighter or more relaxed as the application demands. The value of a, therefore, is chosen as 40.

Table 9.1. Initialization time, attenuation factor and amplitude of 9th harmonic.

a	Tss	Atten. Factor	Amplitude of 9th Harm (V or A)

a has units of Hz. Correct is 1/4 A

How can 1/40 relate the

(rad/s)	(s)		(3^{rd} Harm=1)
0.1	82.7	0.002	0.0002
1	9.31	0.019	0.002
5	1.98	0.1	0.01
10	0.98	0.19	0.02
20	0.64	0.37	0.04
40	0.48	0.62	0.06
80	0.30	0.84	0.08

9.3.4. Comparison of proposed tracking filter and QSG-SOGI

In this section, the proposed tracking system which is compactly expressed in (9.4) and the QSG-SOGI, presented in (9.5), are compared qualitatively and quantitavely for the case in which the actual and estimated frequencies of the harmonic to be extracted from a noisy signal are the same.

In Fig. 9.10, the input is a 60 Hz sinusoid which frequency is disturbed by a normally (Gaussian) distributed noise of mean 0 and variance 50 rad/s. The noise is sampled and held every 0.1 ms. The direct-axis, state x_1, of the proposed filter and the QSG-SOGI are compared with the input in portion a) of Fig. 9.10. In portion b), a 90° phase shift is artificially added to the non-disturbed input signal and it is compared to the q-axis of both the proposed filter and the QSG-SOGI.

While Fig. 9.10 corresponds to the initialization of the tracking filter for the case which has been described in the previous paragraph, Fig. 9.11 corresponds to a comparison in steady-state for the same case. The proposed filter is ~~said~~ seen to be better than the QSG-SOGI.

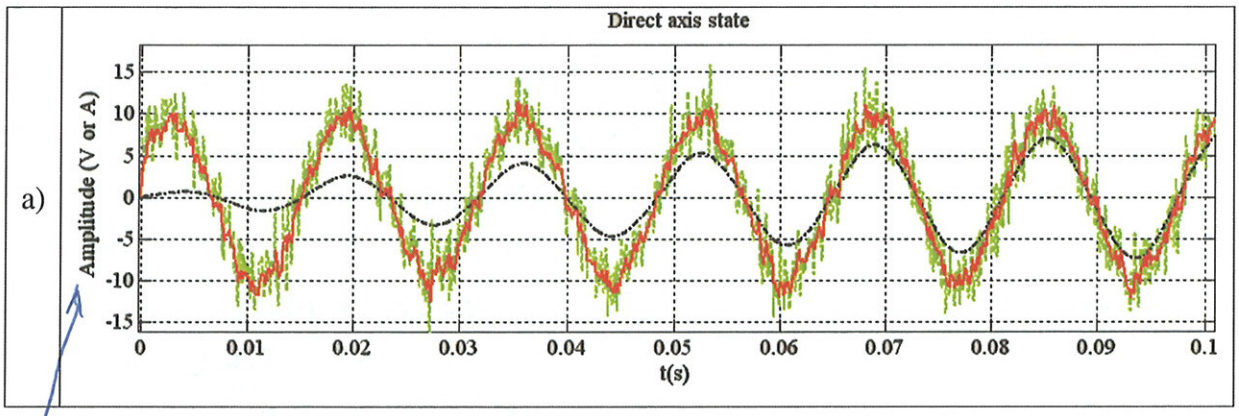

this is not amplitude.

You have not defined d and q axis. (I assume you ~~ref~~ refer to $X_1(t_3)$ ~~cos~~ ~~Coefficients~~

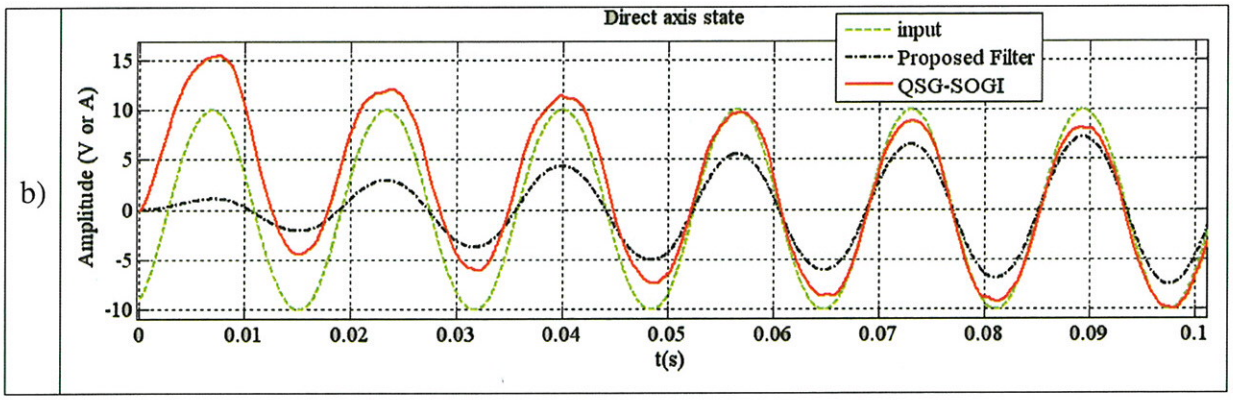

Fig. 9.10. Initialization: Comparison of input which frequency is disturbed by normally distributed high Freq. noise (mean=0, σ^2=50 rad/s, T_s = 0.1 ms) and state x_1 given in (9.4-5)

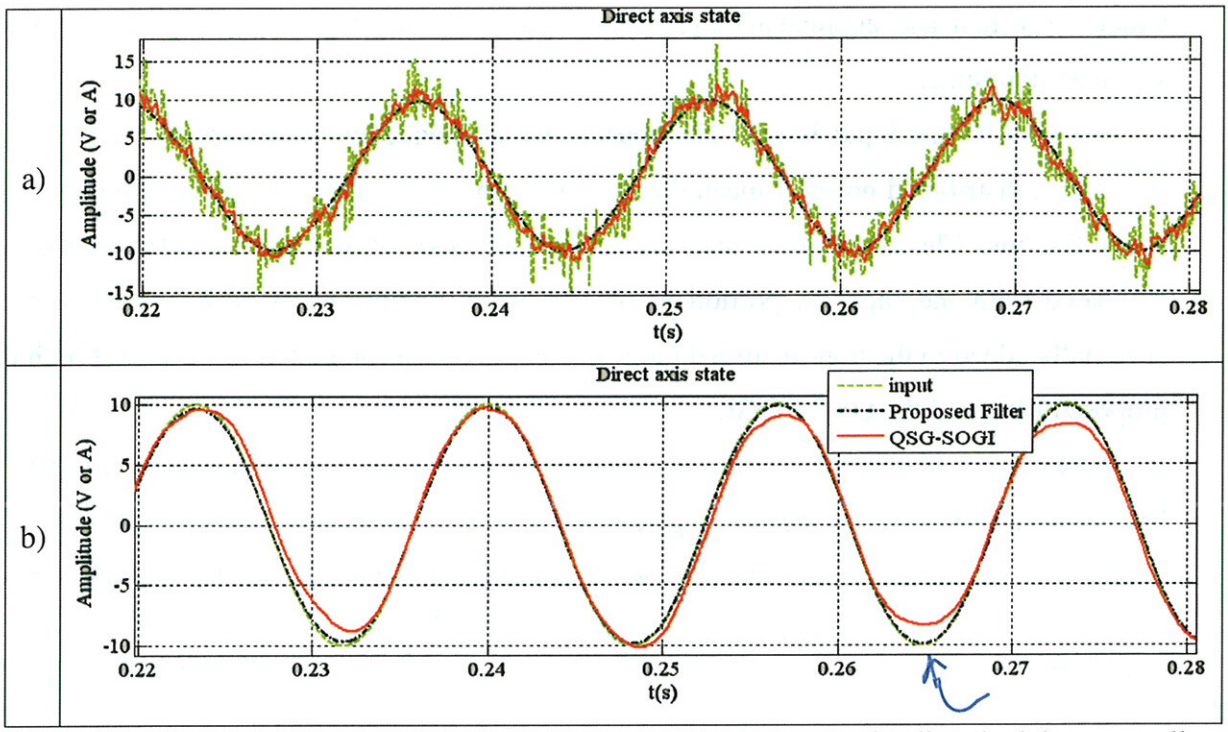

Fig. 9.11. Steady-state: Comparison of input which frequency is disturbed by normally distributed high Freq. noise (mean=0, σ^2=50 rad/s, T_s = 0.1 ms) and state x_1 given in (9.4-5)

The description is not adequate.

In Fig. 9.12, the input is a 60 Hz sinusoid which frequency is disturbed by a similar noise than the one described for the previous case. The difference is that the noise is sampled and held every 10 ms. State x_1 of the proposed filter and the QSG-SOGI are compared with the input in steady-state. Also, a comparison of the q-axis of artificially created, non-contaminated input, proposed tracking filter and QSG-SOGI is presented. Once, again, the proposed filter is said to be better than the QSG-SOGI. Passed the initialization time, the selectivity of the proposed filter far exceed that one of the QSG-SOGI.

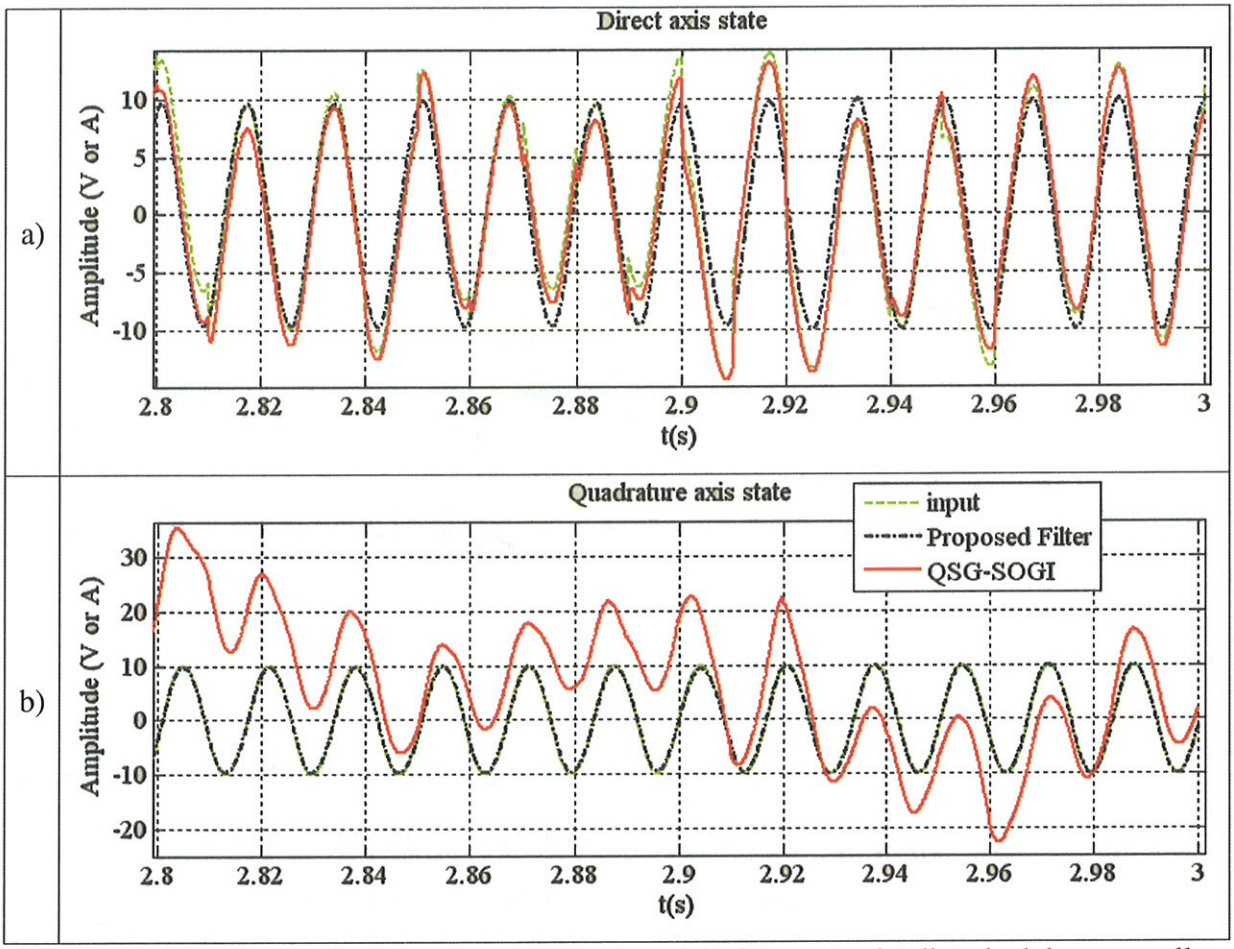

Fig. 9.12. Steady-state: Comparison of input which frequency is disturbed by normally distributed high Freq. noise (mean=0, variance=50 rad/s, T_s = 10 ms) and state x_1 of filters given in (9.4-5)

9.3.5. Some results of the equilibrium trajectory of the tracking filter (9.26)

In this section, the equilibrium trajectory presented in (9.26) is solved for the case in which the actual frequency (frequency of the input) and the estimated frequency (tracking filter) are not equal. In Figs. 9.14-16 equilibrium trajectory coefficients and the reconstructed direct-axis and quadrature-axis waveforms are presented for the case in which the frequency of the input is 60 Hz and the estimated frequency used by the tracking frequency is 59.4 Hz. The delay of the reconstructed quadrature-axis waveform due to this error is 400 μs and the attenuation is 2.12% as illustrated in Fig. 9.16.

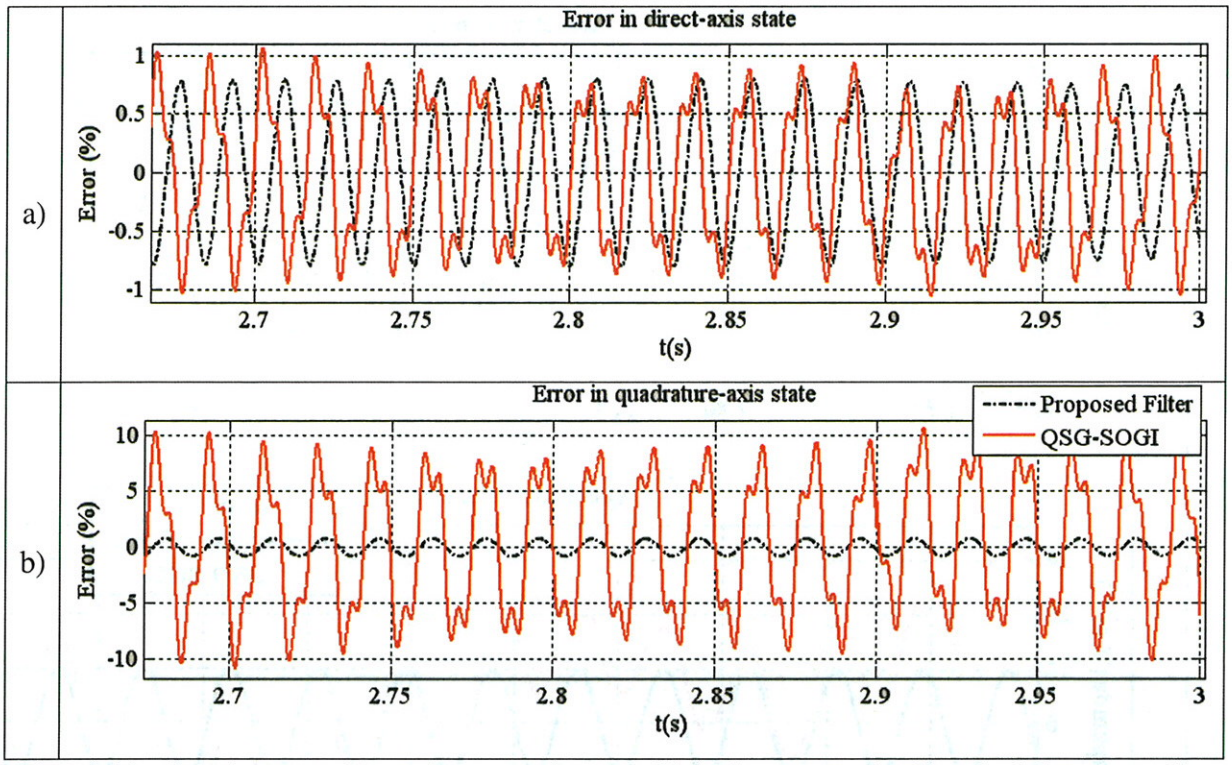

Fig. 9.13. Steady-state: Error between input which frequency is disturbed by normally distributed high Freq. noise (mean=0, σ^2=50 rad/s, T_s = 10 ms) and state x_1 given in (9.4-5)

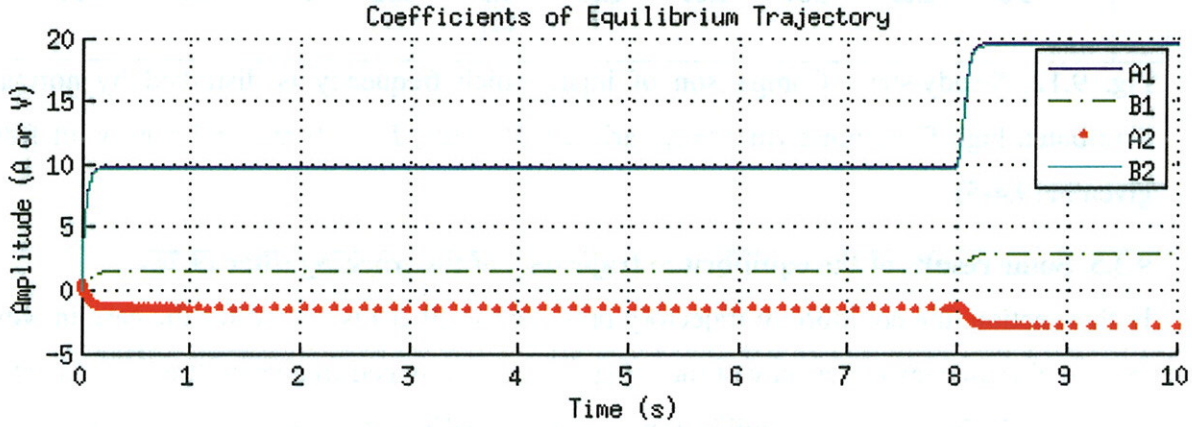

Fig. 9.14. Coefficients of the equilibrium trajectory (9.26) for ω=60 Hz, $\hat{\omega}$=59.4 Hz

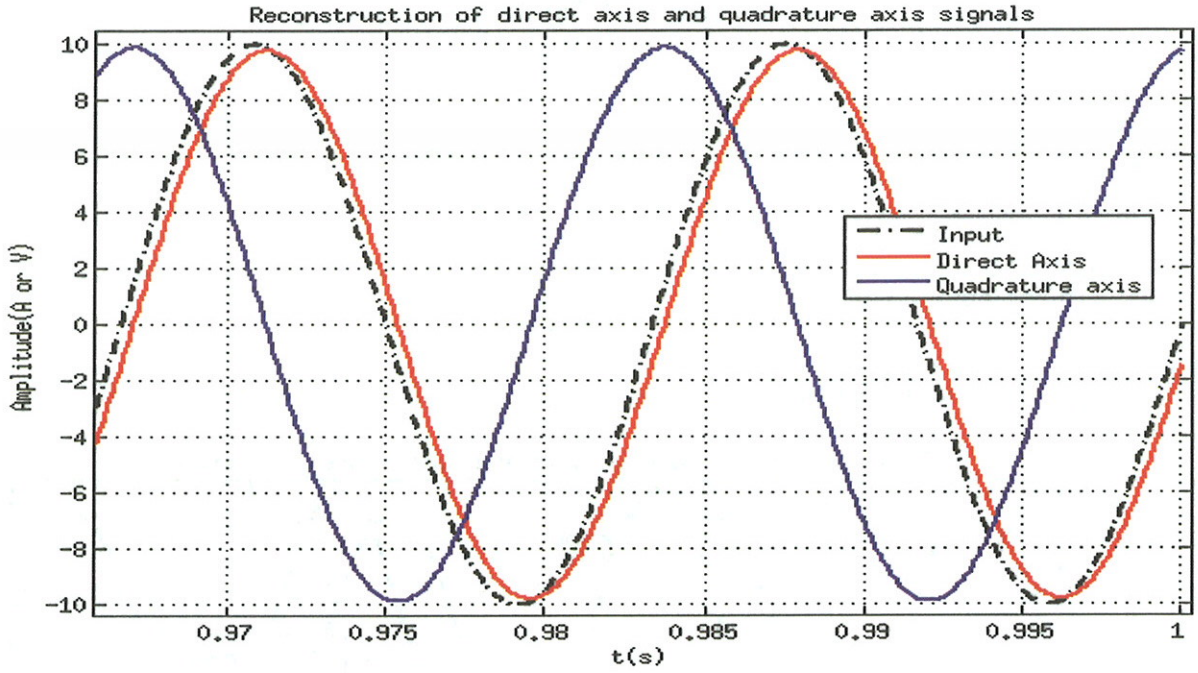

Fig. 9.15. Reconstructed q-axis and d-axis waveforms for ω=60 Hz, $\hat{\omega}$=59.4 Hz

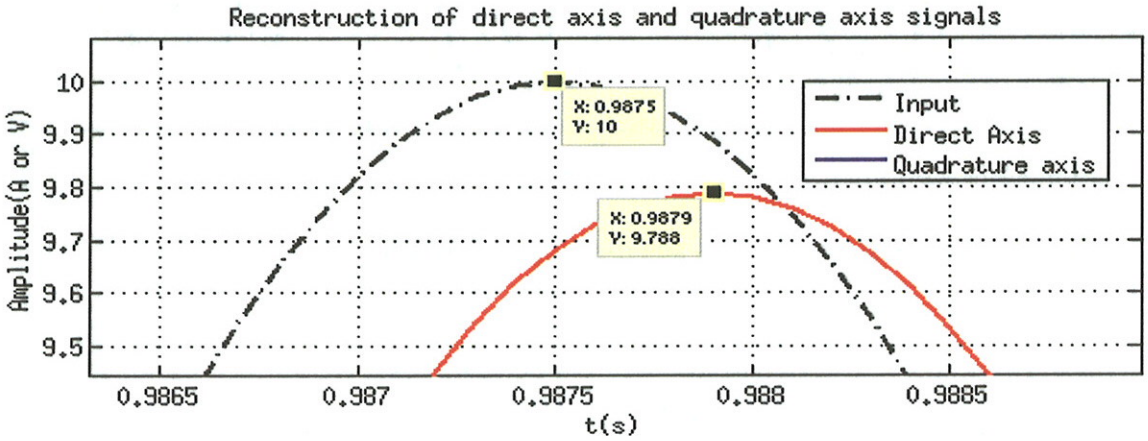

Fig. 9.15. Comparison input and q-axis waveform for ω=60 Hz, $\hat{\omega}$=59.4 Hz

In Figs. 9.17, the coefficients of the equilibrium trajectory given in (9.26) for actual frequency, ω=180 Hz, and estimated frequency, $\hat{\omega}$=178.2 Hz are illustrated. In Fig. 9.18, the reconstructed waveforms for the q-axis and d-axis are compared with the input for the same case. The delay is found to be 400 μs, similar to the previous case, while the attenuation is about 14%. These results have been used in Chapter 5 to determine the threshold of the current sourced by the 3rd harmonic of the inverter CMV.

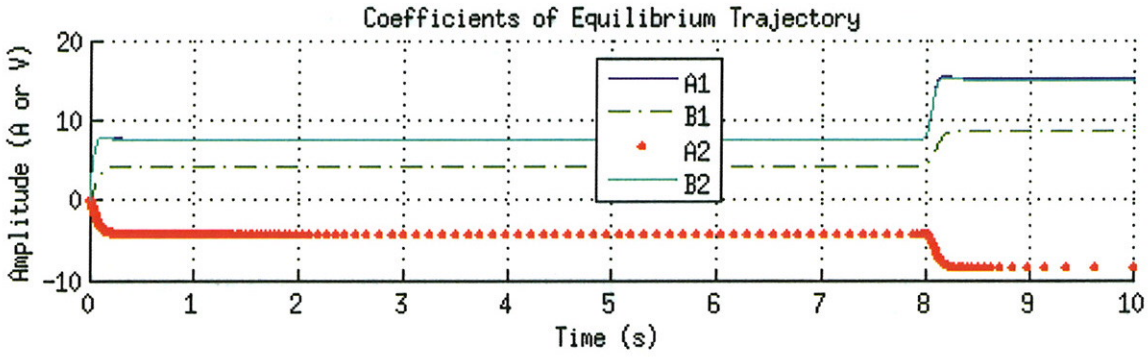

Fig. 9.17. Coefficients of the equilibrium trajectory (9.26) for ω=180 Hz, $\hat{\omega}$=178.2 Hz

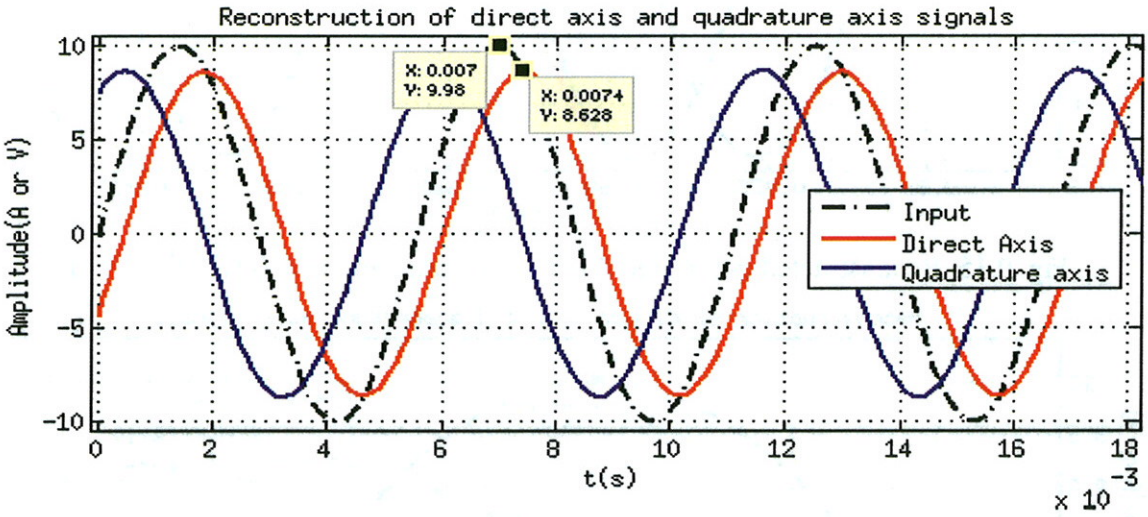

Fig. 9.18. Reconstructed q-axis and d-axis waveforms for ω=180 Hz, $\hat{\omega}$=178.2 Hz

It would be good to show how this performs when this is a small signal relative to remaining frequency content (the intended application).

10. EXPERIMENTAL RESULTS

The experimental results presented in this chapter encompass:

1) Experimental results with long cables: The experimental setup utilized for this case was described in Chapter 3, 10 HP diode-rectifier-inverter system. The cable utilized was the 12 AWG Alcatel PVC Cable Shielded Asymmetrical, 4-conductor cable which parameters are given in Appendix A. Two different lengths of this cable were considered (100 ft and 800 ft). A line-to-ground fault was introduced at the inverter terminals, 100 ft from the inverter terminals or at the motor terminals.
2) Experimental results with 2 ASDs in parallel: The setups utilized for this case are 2 of setup #1 kind. The 2 ASDs are connected such that they share the AC input power. One of the setups was connected to a long cable, the 12 AWG Alcatel PVC Cable Shielded Asymmetrical, 4-conductor. The line-to-ground fault is asserted in only one of the setups. To amplify the effects of stray capacitance, the setup to which the long cable was connected was not the one on which the fault was introduced.

The commissioning stage to determine a threshold, as described in Chapter 5, was implemented in the setup on which terminals a line-to-ground fault was asserted.

10.1. Experimental results with long cables

Two cable lengths (100 ft and 800 ft), hard and softer conditions, R_f =42 Ω, R_f = 10 Ω, R_f = 7 Ω are considered. Also, different operating frequencies, 17 Hz, 37 Hz, 47 Hz, 60 Hz are considered for these experiments.

Due to limitations of dSPACE hardware, data collected from scope shots (inverter operating frequency, current through faulted phase, sum of the 3 phase currents and current through artificially created fault paht) is post-processed together with internally data saved using the dSPACE data logger. An example of the data saved from scope shots, which corresponds to the first test case described below is depicted in Fig. 10.1.

Test 1: the operating frequency of the inverter was set at 60 Hz. The length of the electric cables was 800 ft. A fault was asserted at 100 ft from the inverter terminals. The fault path resistance was set to 42 Ω. The record length was 1 s and the fault occurred at t=0.3008 s. Description of each result is provided below each Fig. From Fig. 10.2, notice that before the fault, the energy content in the higher frequency range is larger than after the fault. Higher frequency content indicates current circulating through stray capacitances.

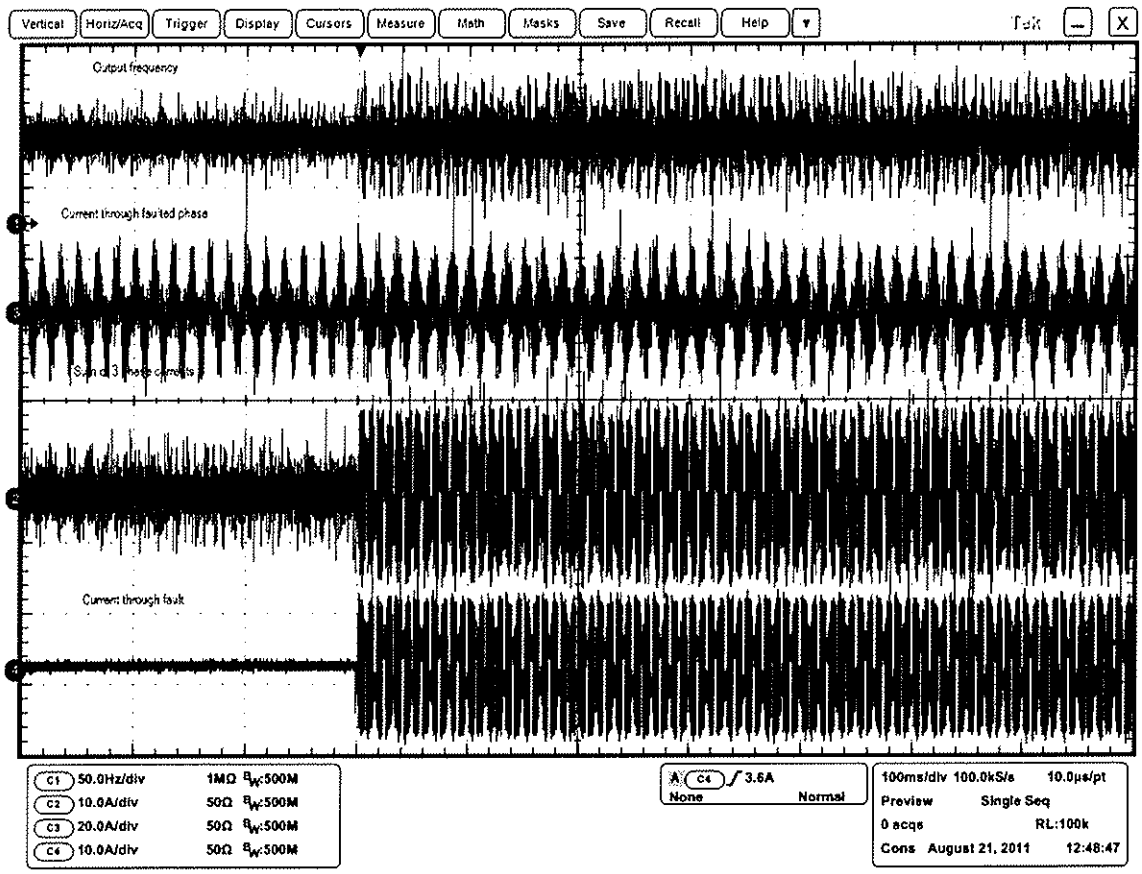

Fig. 10.1. Test 1: Scope shot that illustrates measured signals: Output frequency, current through faulted phase, sum of the 3 currents and current through fault path

In Fig. 10.2 and in Fig. 10.4, more data that was acquired in scope shots is presented. In Fig. 10.2, the sum of the 3 output currents and the corresponding magnitude and phase spectrums are presented (before the occurrence of the line-to-ground fault in black and after the occurrence of the line-to-ground fault in red). Details of Fig. 10.2 are depicted in Fig. 10.4. Herein, the focus is in the low-frequency range, fundamental and 3rd harmonic with some presence of 5th harmonic. The information found in the phase spectrum before and after the occurrence of the line-to-ground fault at low-frequency is hard to compare. This is because effectively there are no frequency components at such low-frequencies before the occurrence of the fault. In Fig. 10.3, the 3rd harmonic of the sum of the 3 output currents and the fault indicator as processed by dSPACE are depicted.

The tracking filter detects the occurrence of the line-to-ground fault just a couple of milliseconds after its occurrence as indicated by the fault indicator. The setting of the threshold was initially attempted at levels given in Chapter 6. It was found that only by delaying the detection of the fault by up to 100 milliseconds and adjusting the threshold given in Chapter 6 by up to 5 mA this was possible.

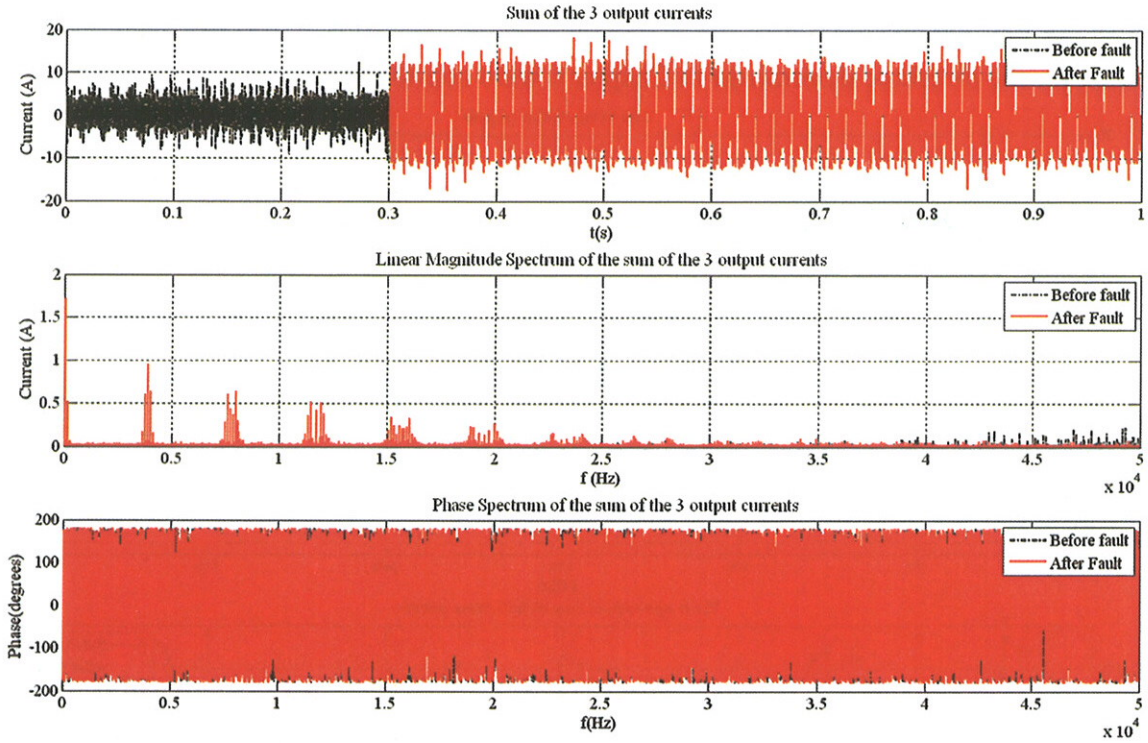

Fig. 10.2. Test 1: Sum of 3 inverter output currents, magnitude spectrum and phase spectrum of the sum of 3 inverter output currents before and after the fault

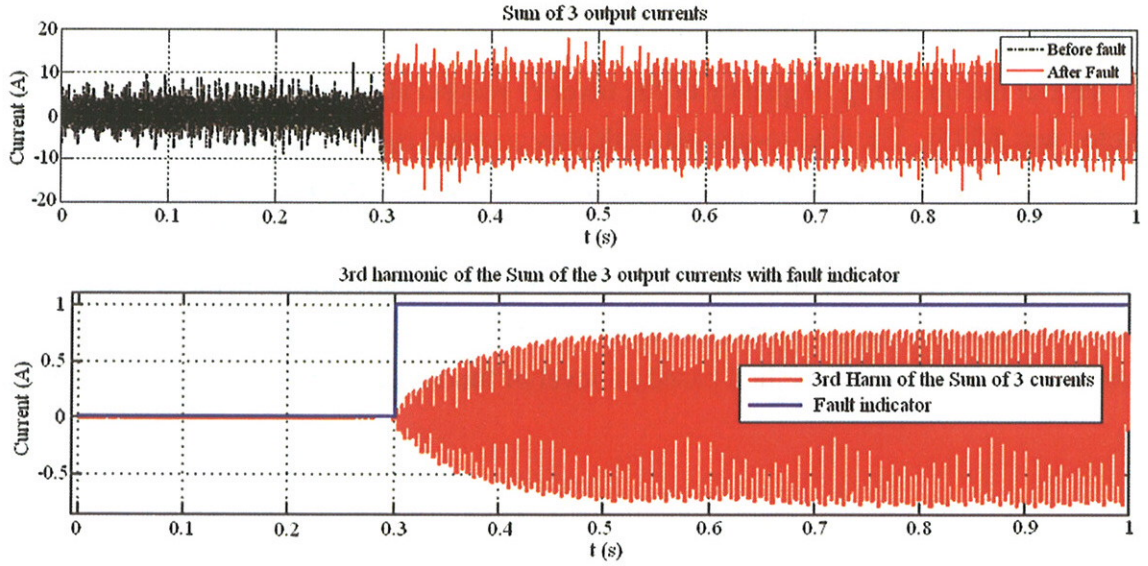

Fig. 10.3. Test 1: Sum of the 3 output currents, extracted 3rd harmonic of the sum of the 3 output currents and fault indicator

Figures need to appear in order discussed

From Fig. 10.23 and/or Fig. 10.25 is appreciated that the tracking filter has an overshoot at the moment of initialization. It is less than 50 mA, but it is large enough to compromise the accuracy of detecting the fault, hence, the delay in the detection of the fault right after the initialization of the tracking filter is important. No proved hypothesis of why the filter behaves like this has been proved at this moment, but it speculated that is due to numerical

error. In the implementation of the detection method, therefore, a 100 ms delay and 5 mA offset for the threshold determined in Chapter 6 were considered.

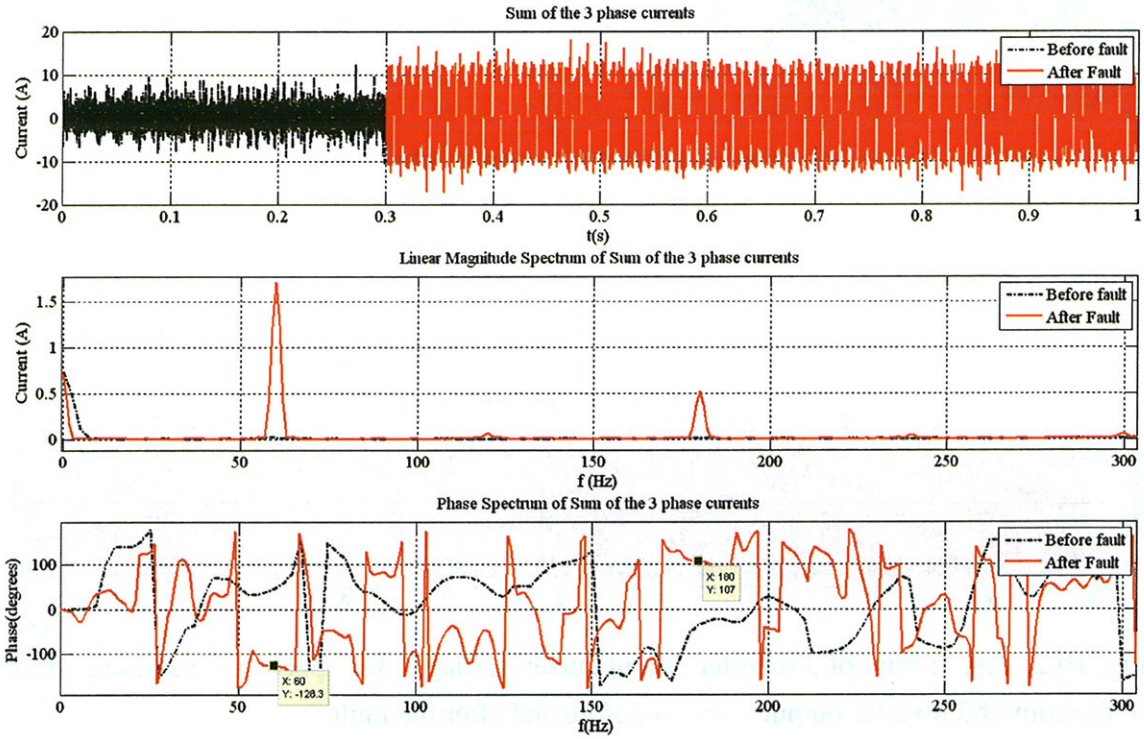

Fig. 10.4. Test 1: Detail of Fig. 10.2 for low-frequency range

Test 2: the operating frequency of the inverter was set at 60 Hz. The length of the electric cables was 800 ft. The line-to-ground fault was asserted right at the terminals of the motor. The fault path resistance was set to 42 Ω. The record length was 1 s and the fault occurred at t=0.3008 s. Notice that the fault is detected in about 2 ms, as depicted in Fig. 10.6

From Fig. 10.6, notice that the sum of the 3 output currents of the inverter when the fault occurs is such that the 3rd harmonic added to the fundamental limits the magnitude of the fundamental. A detection method based on level of fundamental should account for this fact.

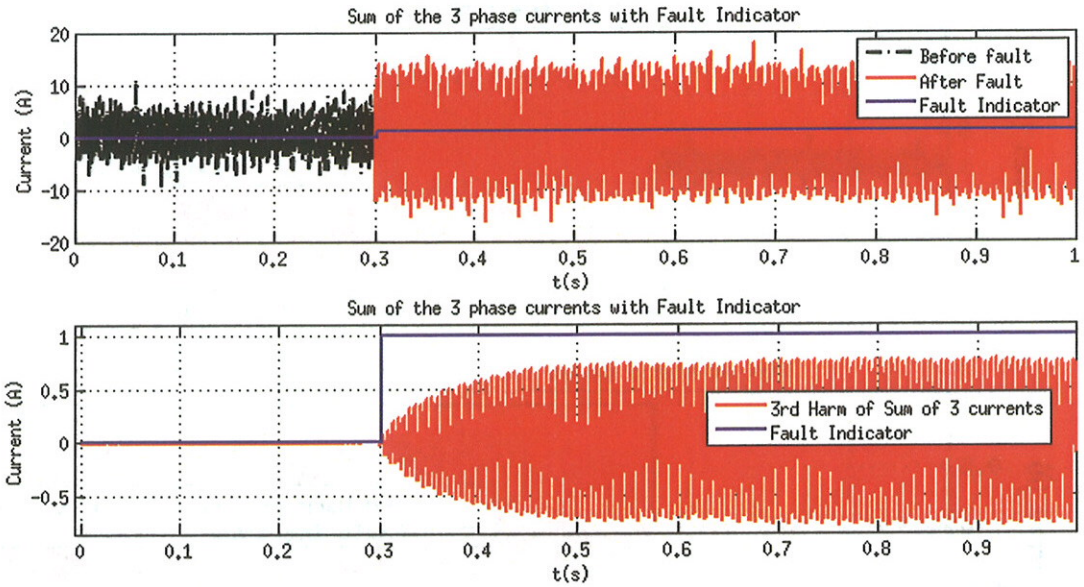

Fig. 10.5. Test 2: Sum of 3 output currents with fault indicator, 3rd harmonic of the sum of the 3 currents extracted by tracking filter with fault indicator

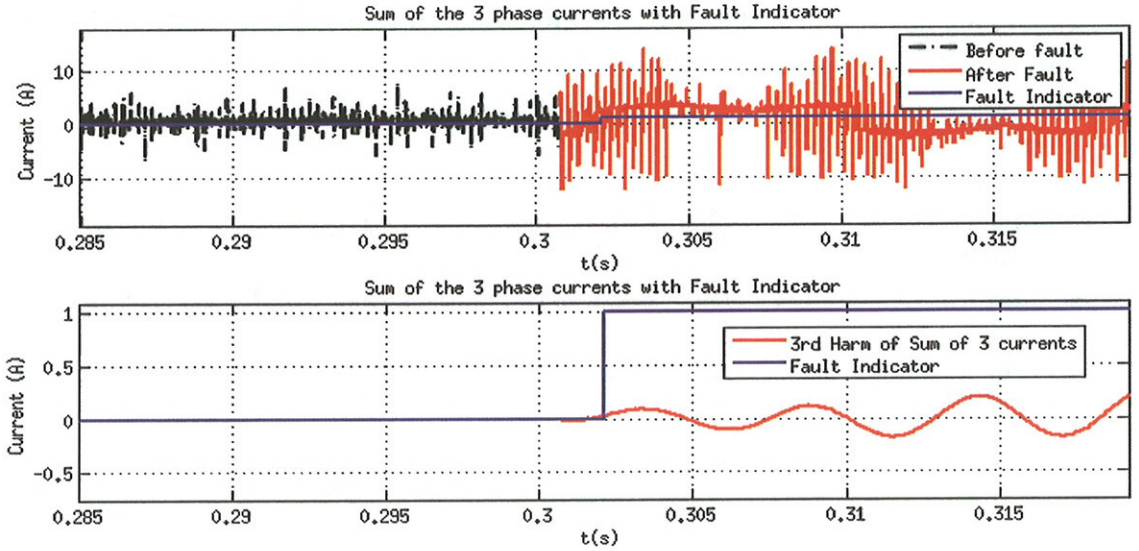

Fig. 10.6. Test 2: Detail of Fig 10.5

Test 3: the operating frequency of the inverter was set at 60 Hz. The length of the electric cables was 100 ft. A fault was asserted right at the terminals of the inverter at instant 0.6 s. The fault path resistance was set to 42 Ω. The record length was 2 s.

The fault was detected in less than 3 ms. When this case is compared to the 2 previous ones in which the cable length was 800 ft, the difference is clear before the occurrence of the fault. The current flowing through stray inductances is much larger for the previous 2 cases.

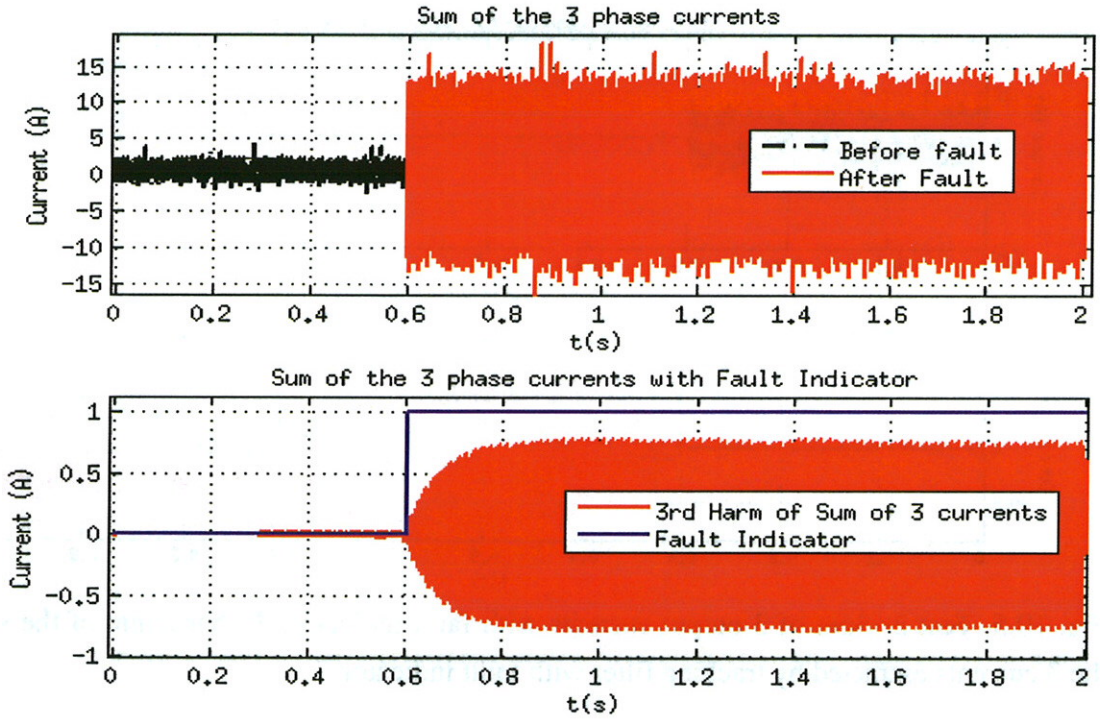

Fig. 10.7. Test 3: Sum of 3 output currents with fault indicator, 3rd harmonic of the sum of the 3 currents extracted by tracking filter with fault indicator

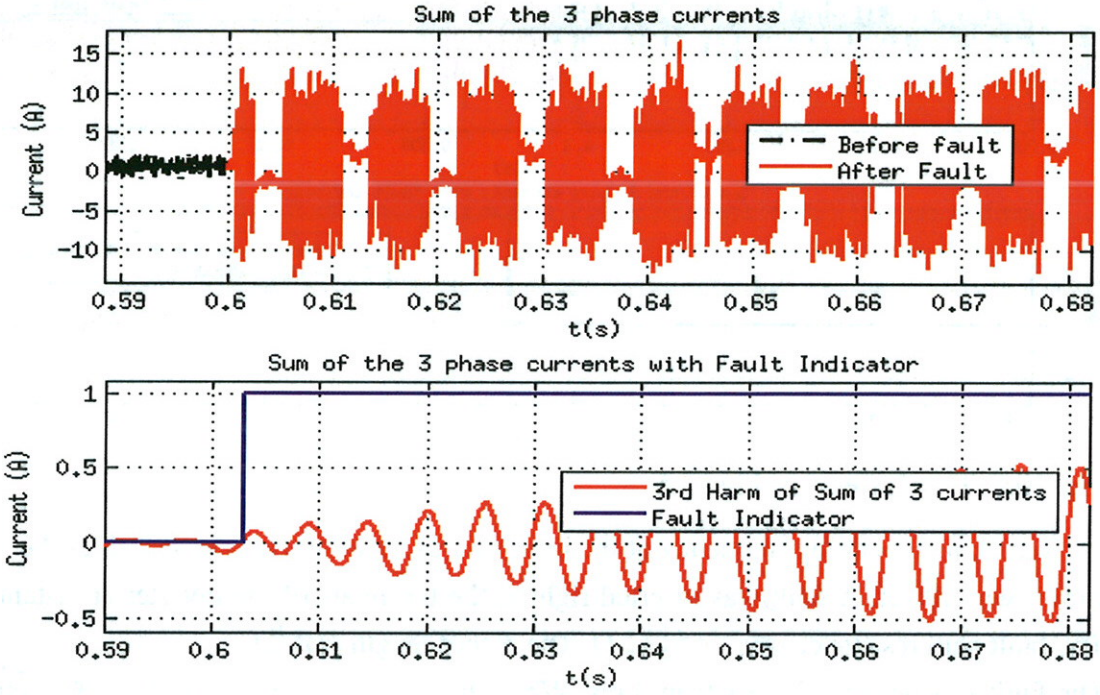

Fig. 10.8. Test 3: Detail of Fig. 10.7

Test 4: the operating frequency of the inverter was set at 37 Hz. The length of the electric cables was 800 ft. A fault was asserted right at the terminals of the motor. The fault path

resistance was set to 42 Ω. The record length was 1 s and the fault occurred at t=0.3008 s. The fault was detected in about 15 ms.

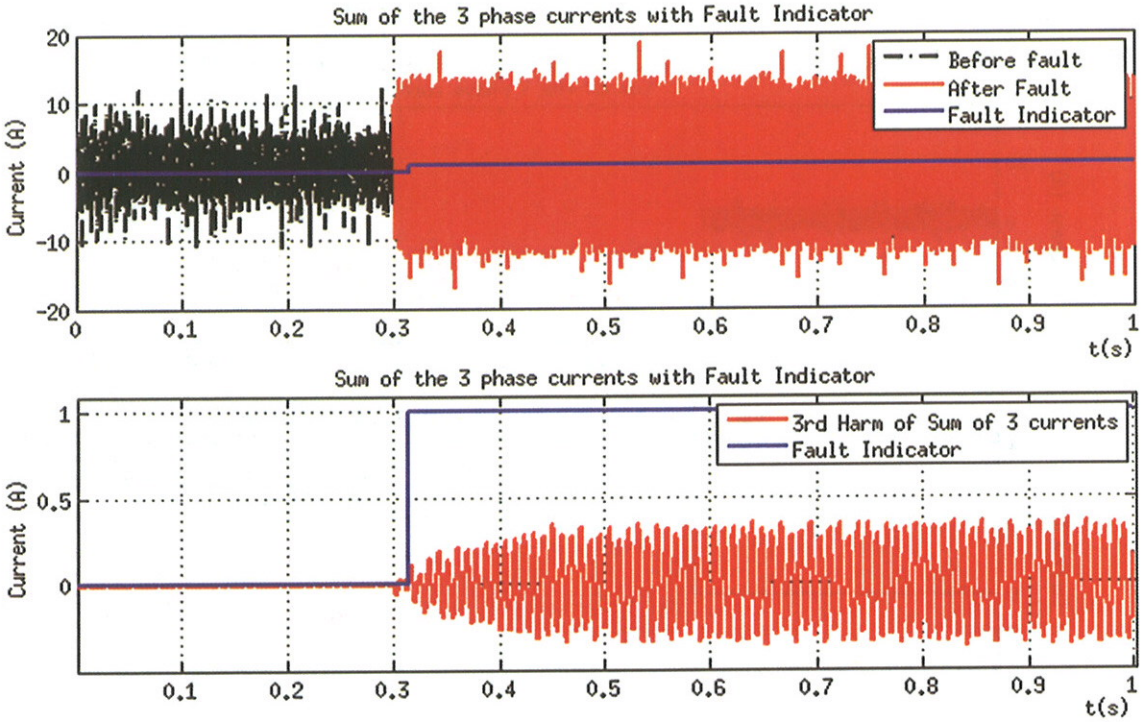

Fig. 10.9. Test 4: Sum of 3 output currents with fault indicator, 3rd harmonic of the sum of the 3 currents extracted by tracking filter with fault indicator

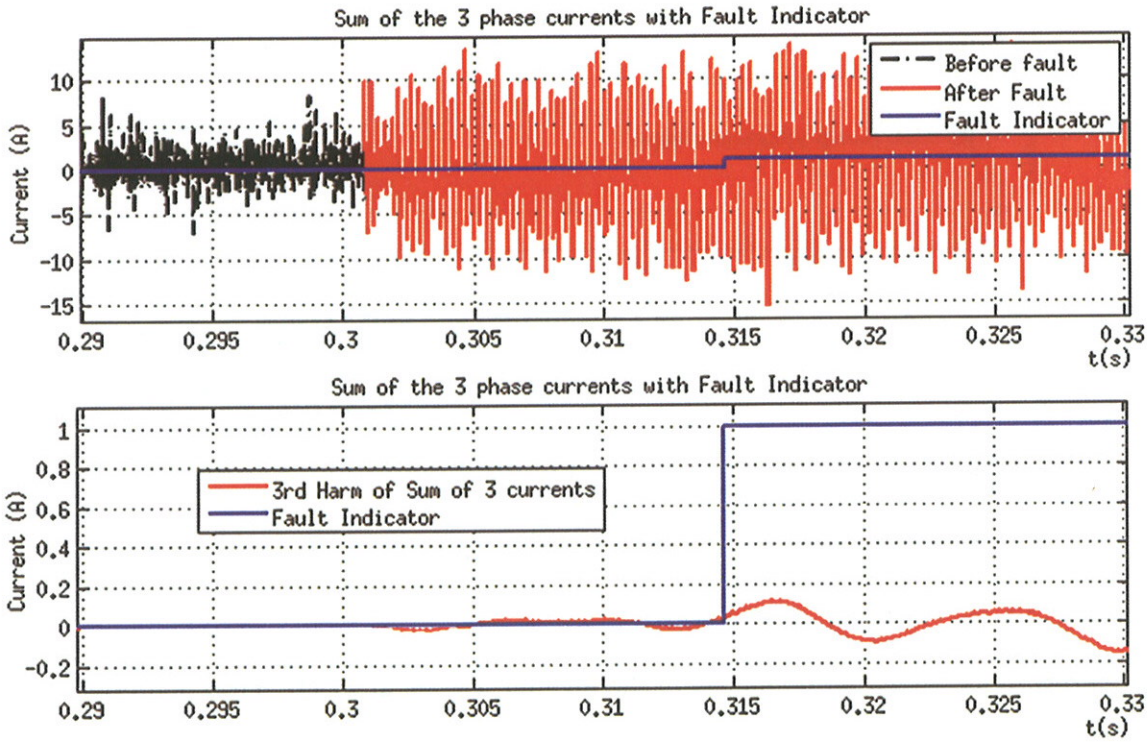

Fig. 10.10. Test 4: Detail of Fig. 10.8

Test 5: the operating frequency of the inverter was set at 37 Hz. The length of the electric cables was 100 ft. A fault was asserted right at the terminals of the inverter. The fault path resistance was set to 42 Ω. The record length was 1 s and the fault occurred at t=0.3008 s. The fault was detected in about 5 ms. Corresponds to this test Figs. 10.10-11

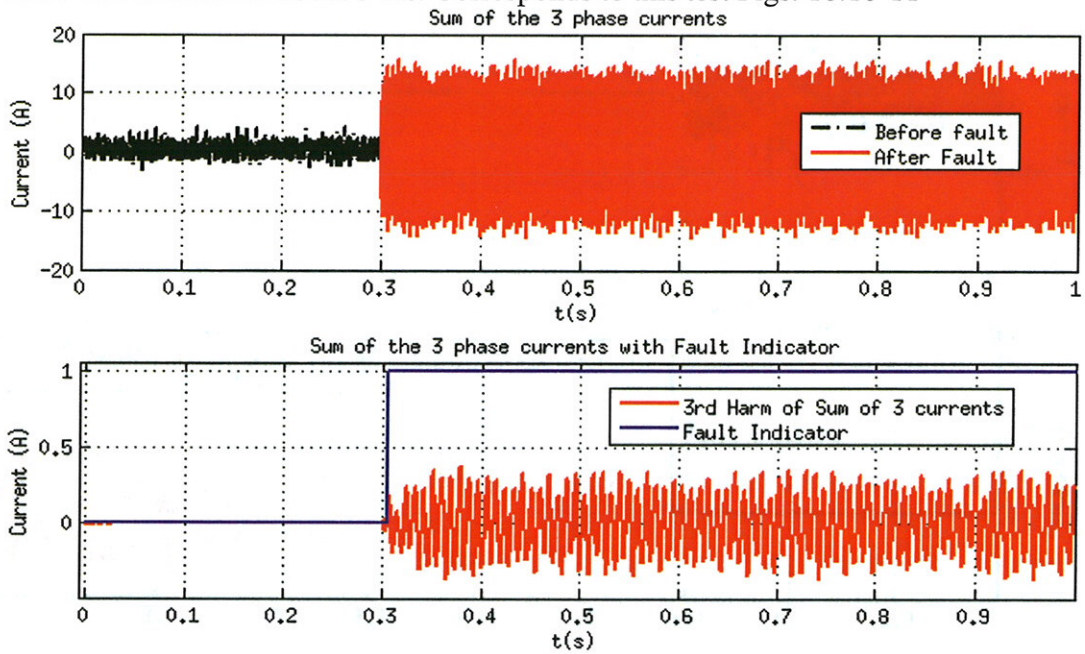

Fig. 10.11. Test 5: Sum of 3 output currents with fault indicator, 3rd harmonic of the sum of the 3 currents extracted by tracking filter with fault indicator

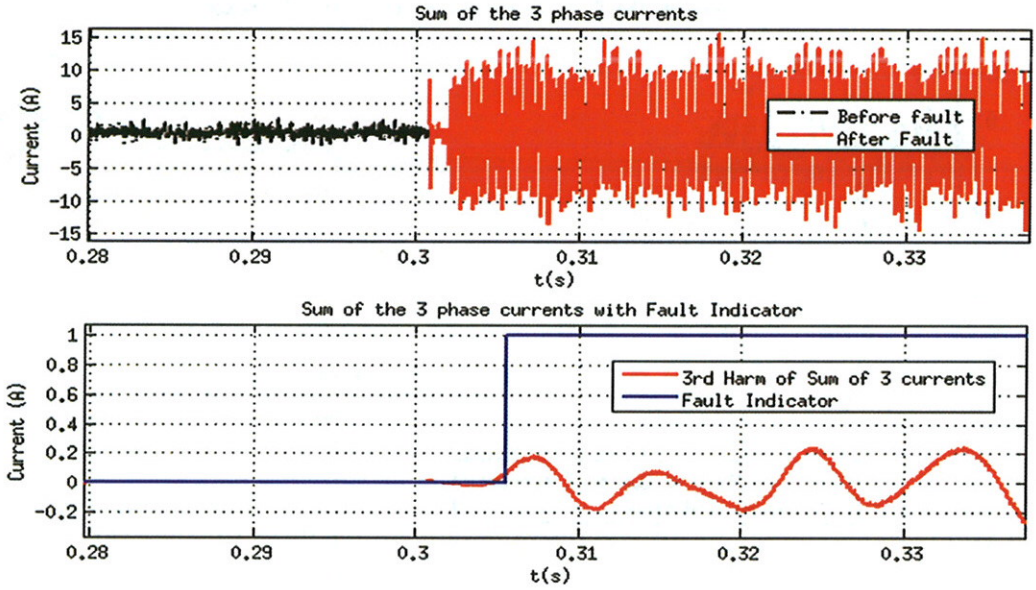

Fig. 10.12. Test 5: Detail of Fig. 10.10

Test 6: the operating frequency of the inverter was set at 17 Hz. The length of the electric cables was 100 ft. A fault was asserted right at the terminals of the inverter. The fault path

resistance was set to 7 Ω. The record length was 1 s and the fault occurred at t=0.3008 s. The fault was detected in about 8 ms.

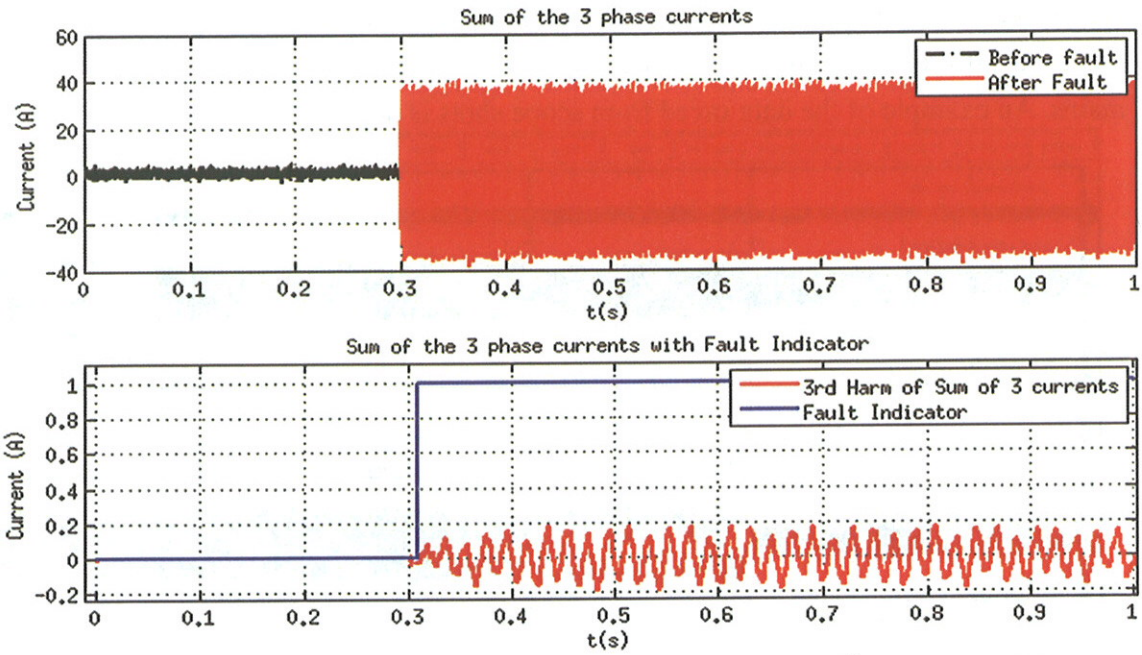

Fig. 10.13. Test 6: Sum of 3 output currents with fault indicator, 3rd harmonic of the sum of the 3 currents extracted by tracking filter with fault indicator

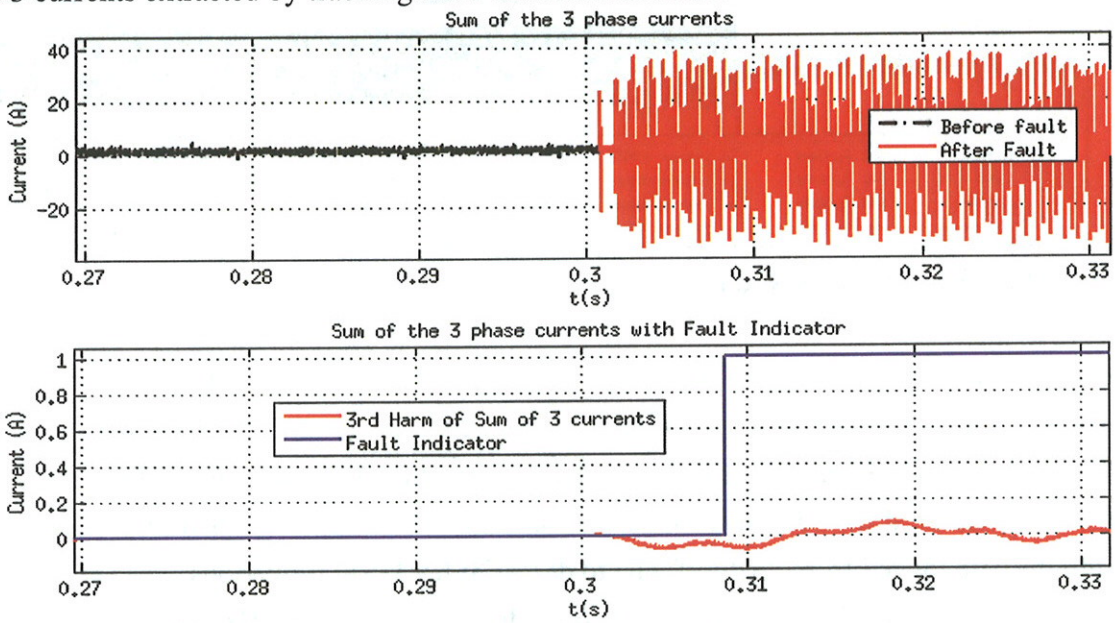

Fig. 10.14. Test 6: Detail of Fig. 10.12

10.2. Experimental results with 2 ASDs in parallel

The fault scenarios include hard and soft types of faults, R_f =42 Ω, R_f = 10 Ω. In all cases, the length of the electric cable connected to the non-faulted drive is 800 ft. This is done to

amplify stray capacitance effects. The cable connected to the non-faulted drive is 25 ft. In all cases, the fault is asserted at the terminals of the motor. The operating frequencies of the drives are set: 1) different from each other and different from the mains, 2) equal to each other but different than the mains, 3) equal to each other and equal to the frequency of the mains. An example of the data saved from scope shots is depicted in Fig. 10.15.

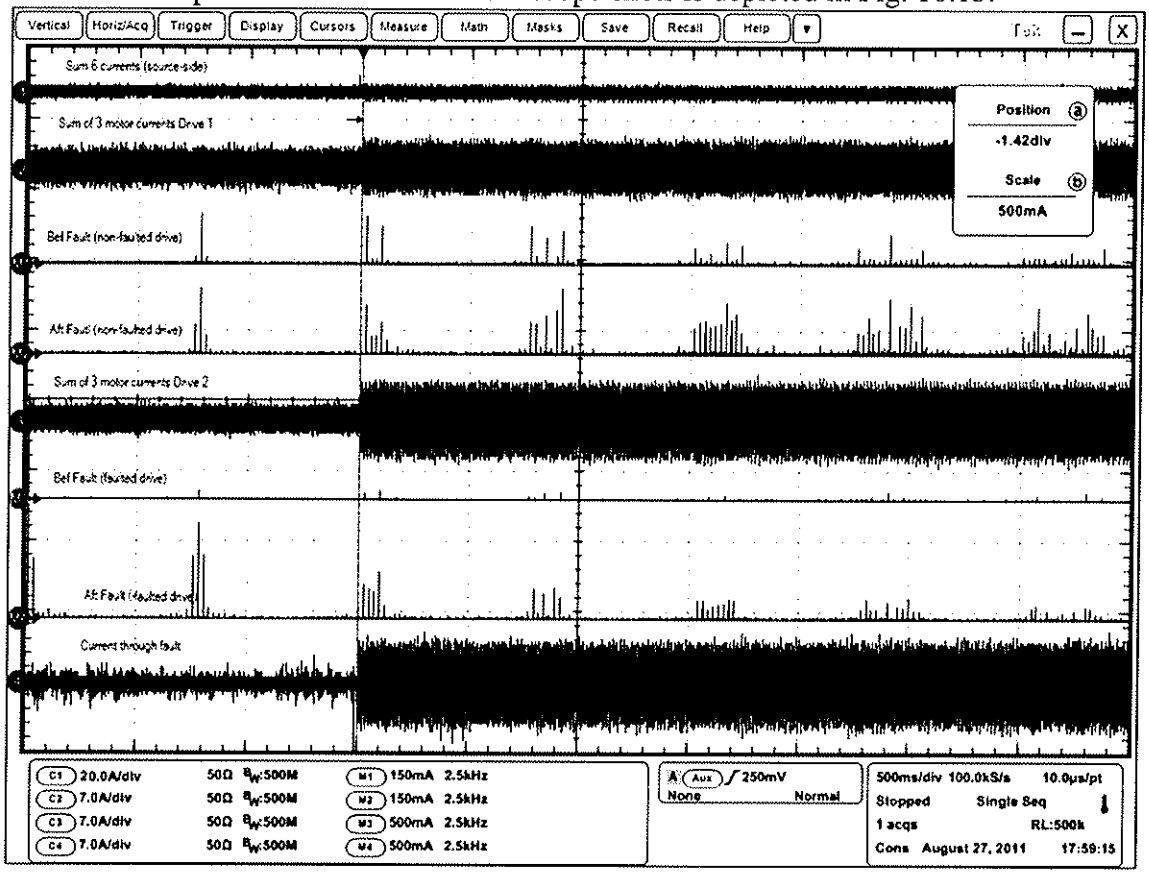

Fig. 10.15. Test 1: Data saved from scope shots

Data saved include: a) Sum of 6 currents at the source-side, b) Sum of the 3 output currents of the non-faulted drive and magnitude spectrum before and after the fault has occurred, c) Sum of the 3 output currents of the faulted drive and magnitude spectrum before and after the fault has occurred d) Current through the fault path. Data saved is post-processed together with the data logged from dSPACE due to dSPACE hardware limitations.

Test 1: The Op. Freq. of the non-faulted drive was set at 60 Hz. The Op. Freq. of the faulted drive was set at 60 Hz. The fault path resistance R_f =42 Ω.

In Fig. 10.16, the sum of the 3 inverter currents for the non-faulted drive and the faulted drive are presented together with a linear magnitude spectrum of such signals before and after the occurrence of the line-to-ground fault. A detail is provided in the same Fig. for the low-frequency harmonic content.

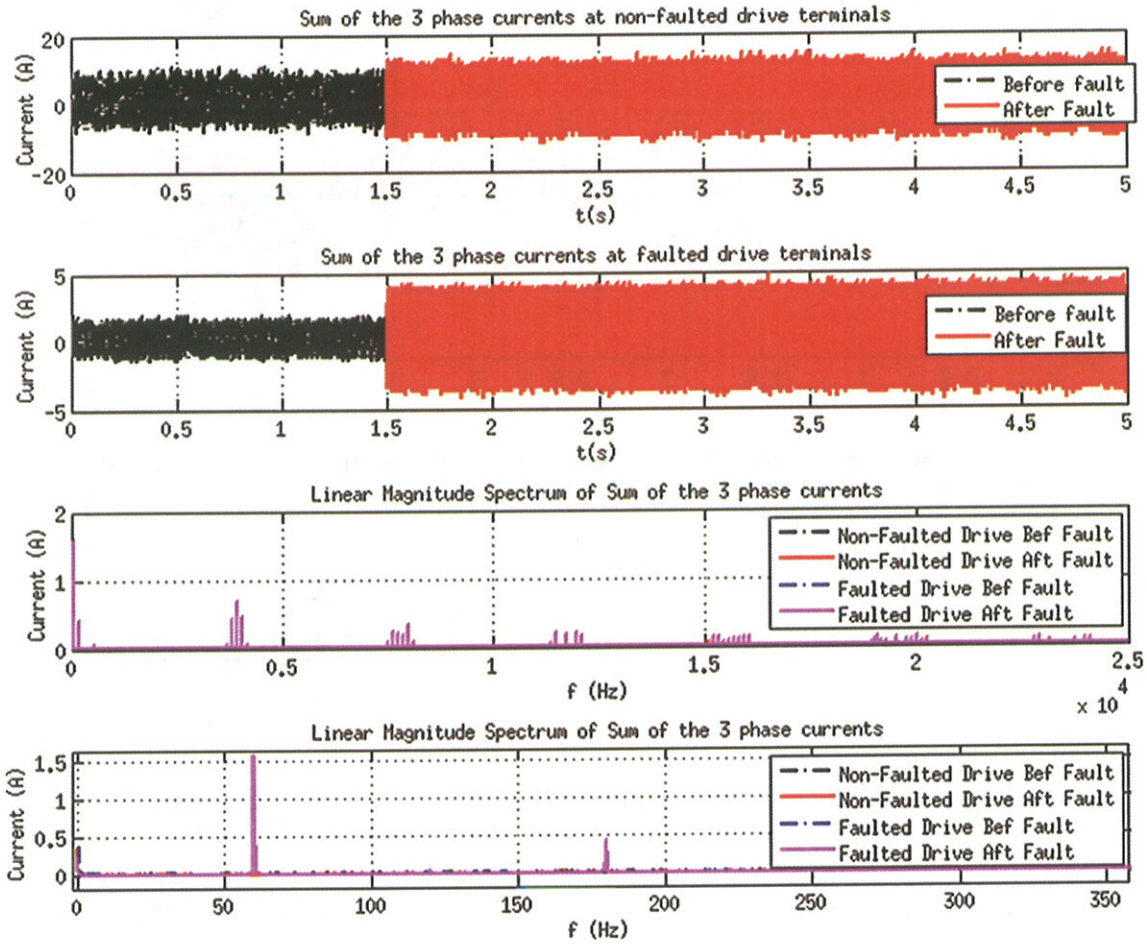

Fig. 10.16. Test 1: Sum of the 3 output currents at non-faulted drive terminals, sum of the 3 output currents at the faulted drive terminals, linear magnitude spectrum of the sum of the 3 output currents and detail of the magnitude spectrum at tracked frequency

In Fig. 10.17 the 3rd harmonic of the sum of the 3 output currents as tracked by the tracking filter is depicted for the drive with no fault and the drive on which terminals a line-to-ground fault has been asserted. The fault indicator signals the detection of a line-to-ground fault only in the drive on which terminals the fault occurred.

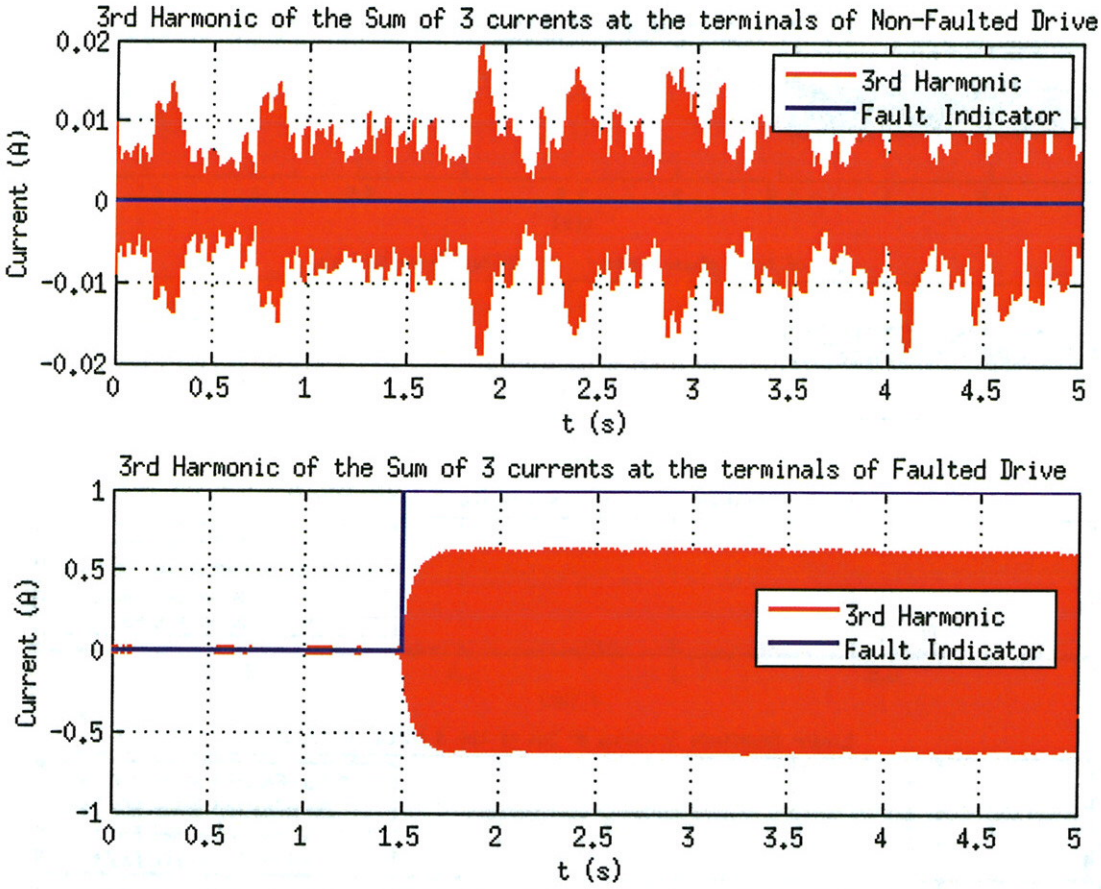

Fig. 10.17. Test 1: 3rd harmonic of the sum of the currents at the terminals of the non-faulted drive (in red) with fault indicator (in blue), 3rd harmonic of the sum of the currents at the terminals of the faulted drive (in red) with fault indicator (in blue)

Test 2: The operating frequency of the non-faulted drive was set at 60 Hz. The operating frequency of the faulted drive was set at 60 Hz. The fault path resistance R_f =10 Ω. The detection time was 5 ms.

By comparing the 3rd harmonic of the sum of the 3 output currents tracked in Test 1 and in Test 2, it is apparent the presence of a varying phase shift between the CMV of the inverter and the CMV of the converter. This has been identified to be generated by the control of the inverter that uses an unbalanced set of currents to generate a balance set of modulated voltages. Further refinement of the control of the inverter is beyond the scope of this dissertation.

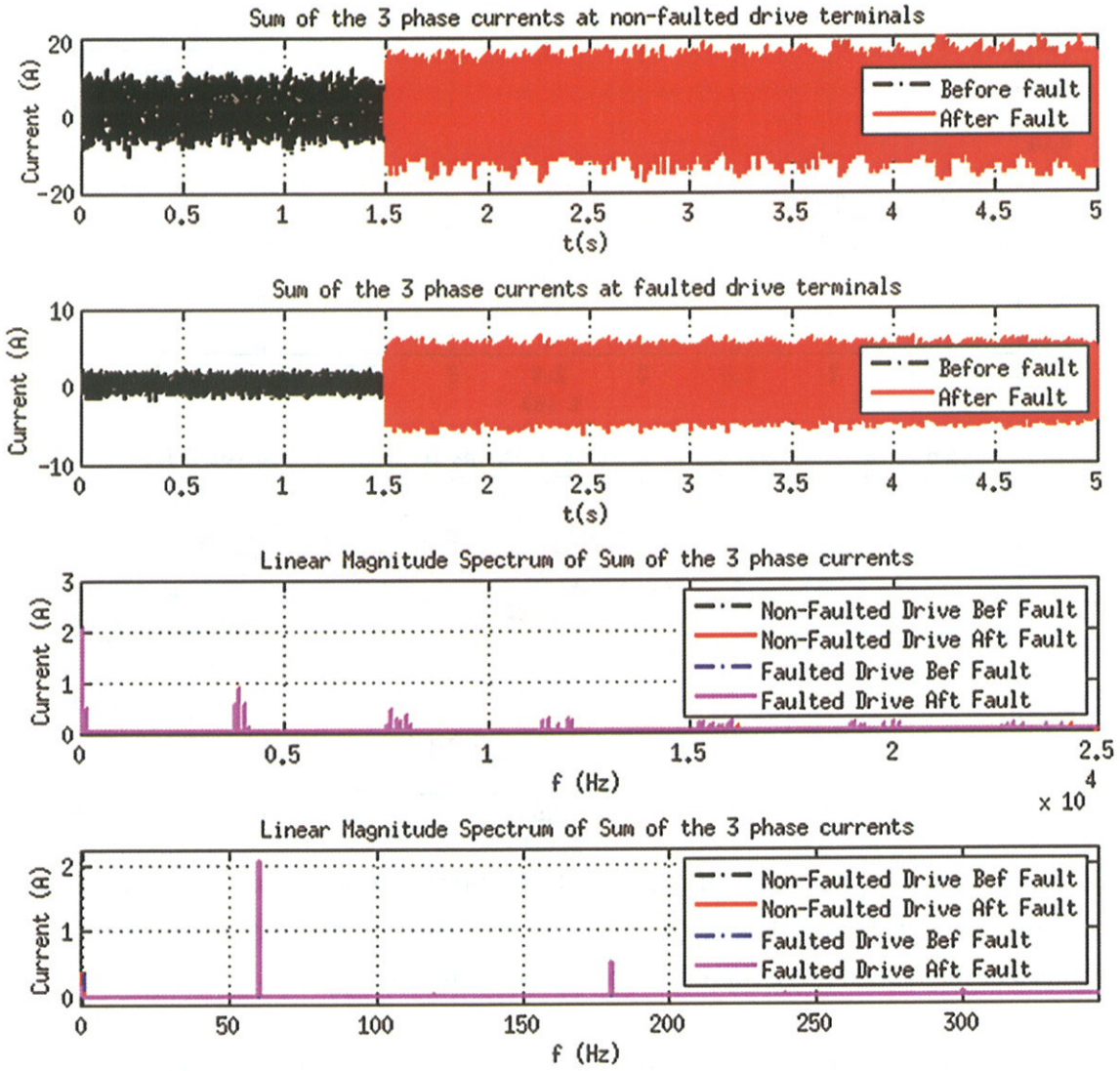

Fig. 10.18. Test 2: Sum of the 3 output currents at non-faulted drive terminals, sum of the 3 output currents at the faulted drive terminals, linear magnitude spectrum of the sum of the 3 output currents and detail of the magnitude spectrum at tracked frequency

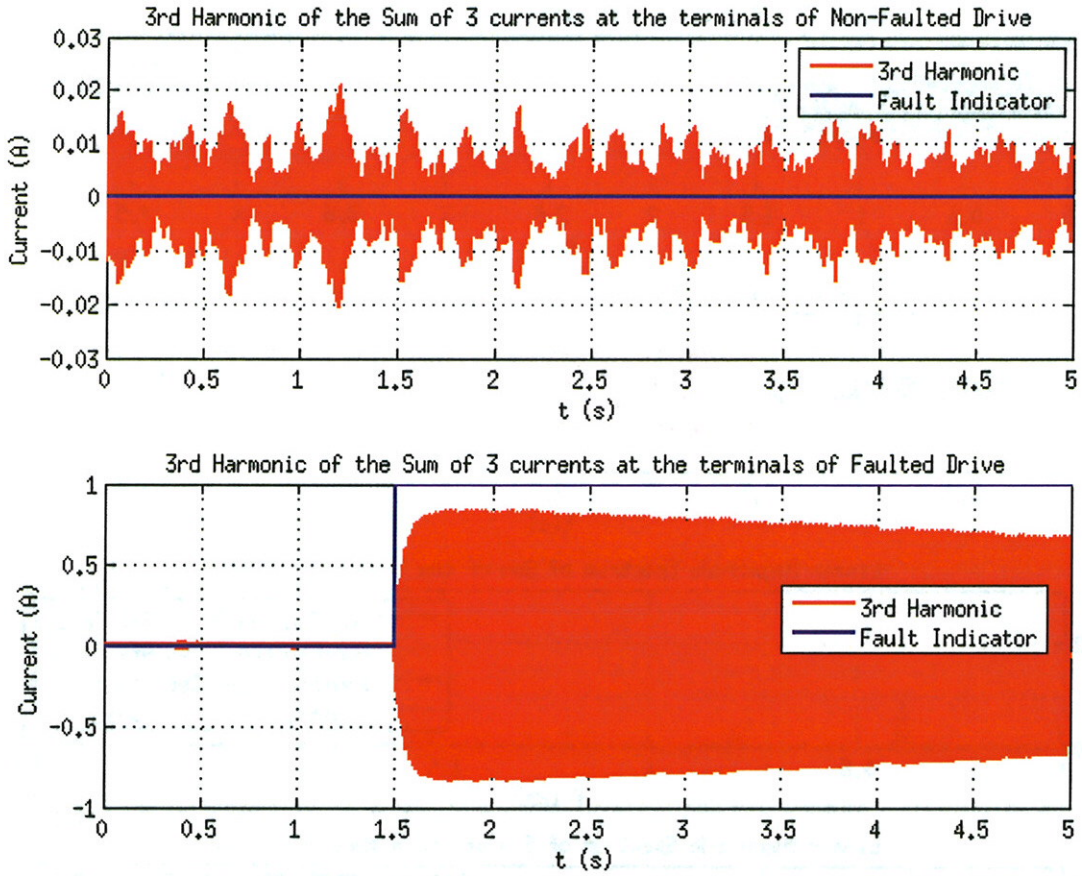

Fig. 10.19. Test 2: 3rd harmonic of the sum of the currents at the terminals of the non-faulted drive (in red) with fault indicator (in blue), 3rd harmonic of the sum of the currents at the terminals of the faulted drive (in red) with fault indicator (in blue)

Test 3: The operating frequency of the non-faulted drive was set at 47 Hz. The operating frequency of the faulted drive was set at 17 Hz. The fault path resistance was R_f =10 Ω. The detection time was roughly 1.9 ms. Figs. 10.20-21 correspond to this test.

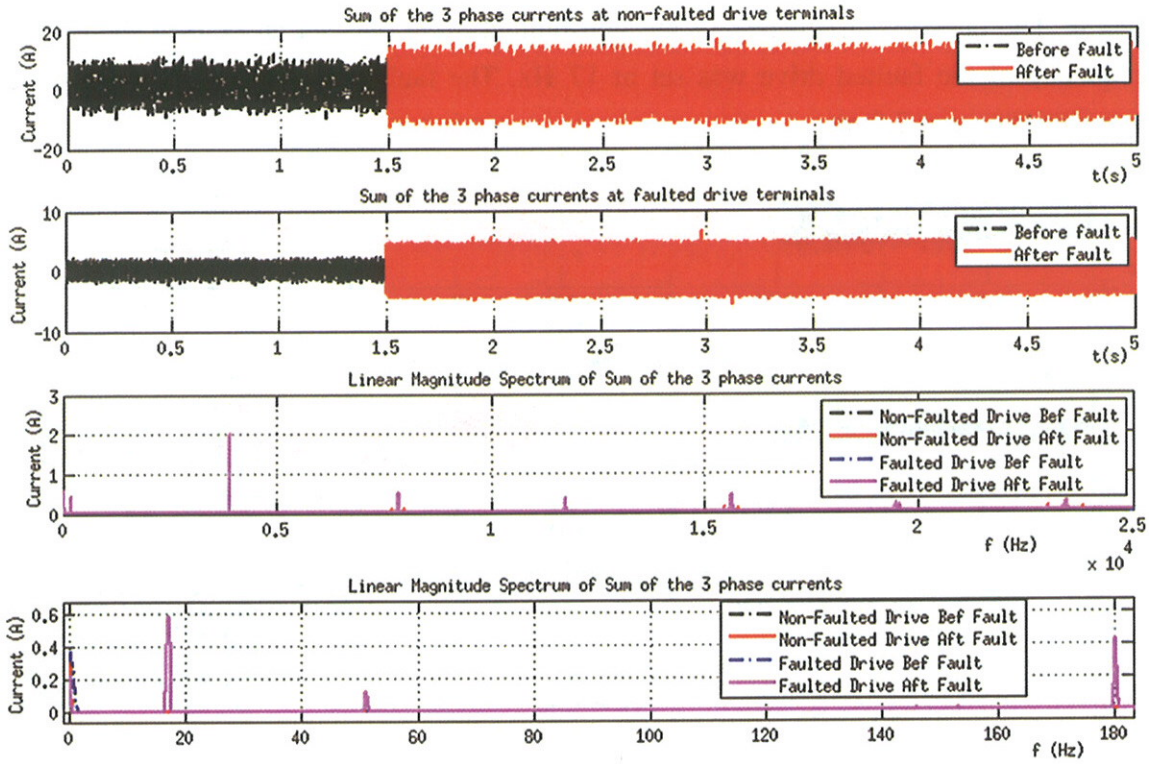

Fig. 10.20. Test 3: Sum of the 3 output currents at non-faulted drive terminals, sum of the 3 output currents at the faulted drive terminals, linear magnitude spectrum of the sum of the 3 output currents and detail of the magnitude spectrum at tracked frequency

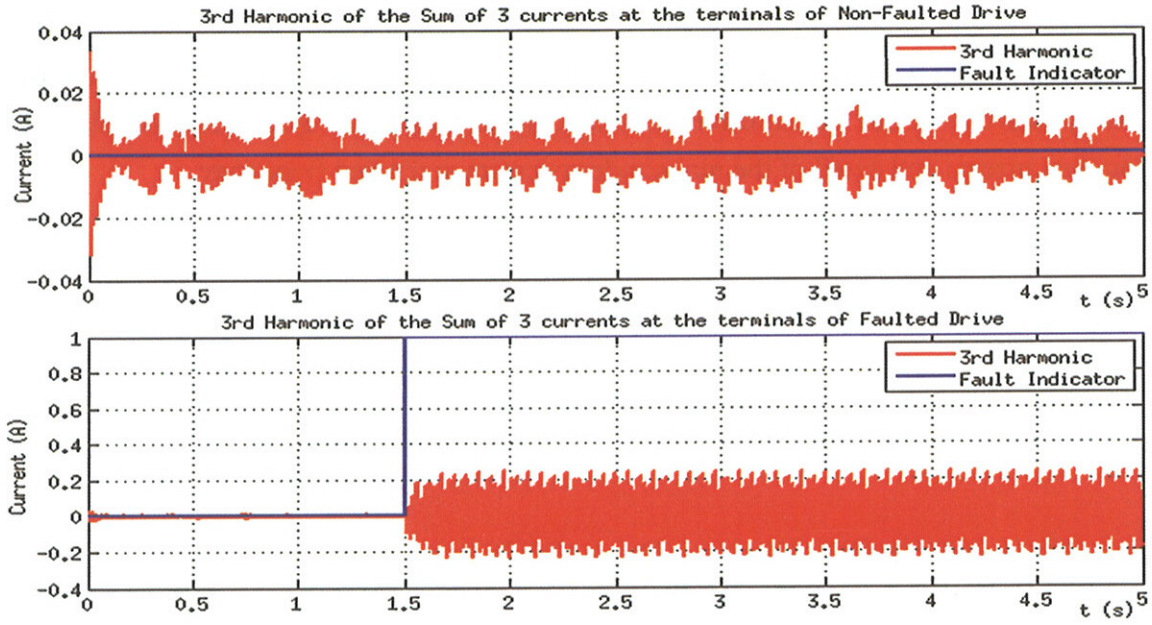

Fig. 10.21. Test 3: 3rd harmonic of the sum of the currents at the terminals of the non-faulted drive (in red) with fault indicator (in blue), 3rd harmonic of the sum of the currents at the terminals of the faulted drive (in red) with fault indicator (in blue)

Test 4: The operating frequency of the non-faulted drive was set at 17 Hz. The operating frequency of the faulted drive was set at 17 Hz. The fault path resistance R_f =10 Ω. The detection time was 2.8 ms.

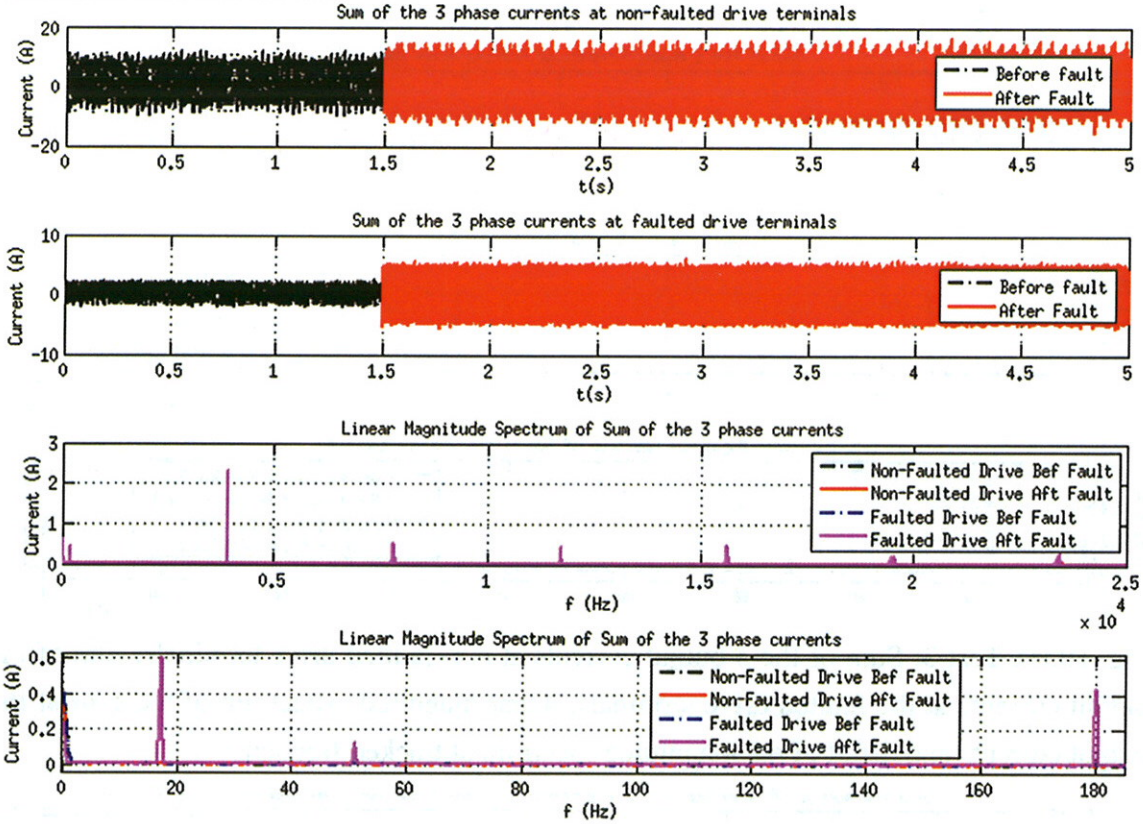

Fig. 10.22. Test 4: Sum of the 3 output currents at non-faulted drive terminals, sum of the 3 output currents at the faulted drive terminals, linear magnitude spectrum of the sum of the 3 output currents and detail of the magnitude spectrum at tracked frequency

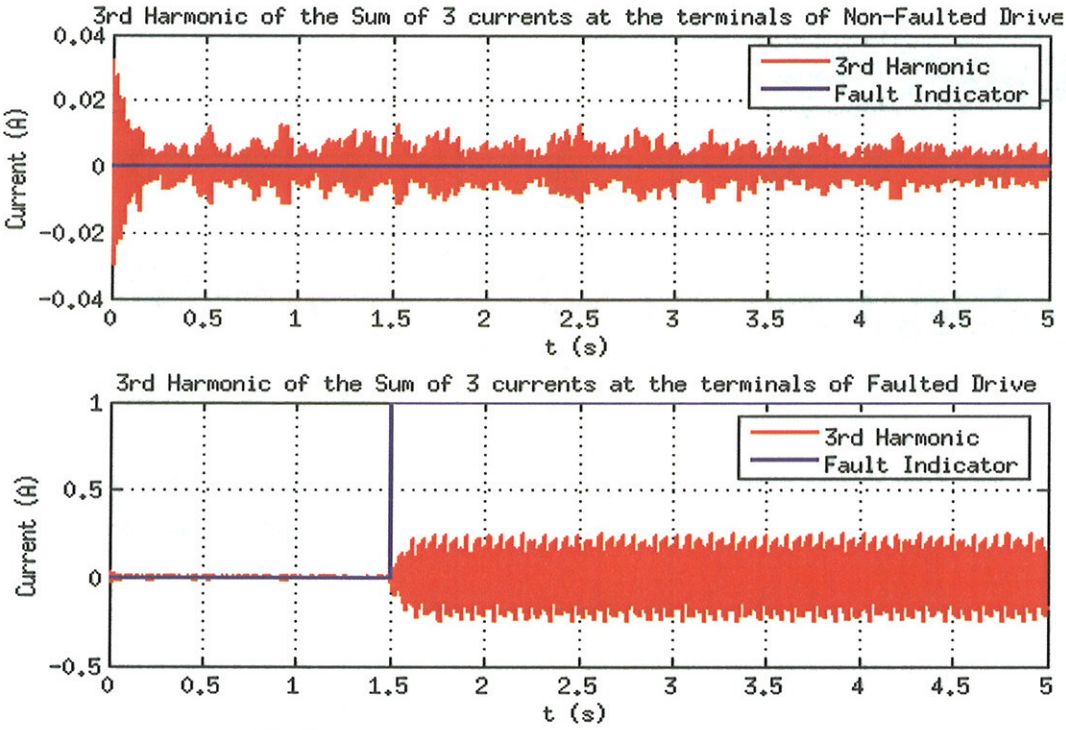

Fig. 10.23. Test 4: 3rd harmonic of the sum of the currents at the terminals of the non-faulted drive (in red) with fault indicator (in blue), 3rd harmonic of the sum of the currents at the terminals of the faulted drive (in red) with fault indicator (in blue)

Test 5: The operating frequency of the non-faulted drive was set at 17 Hz. The operating frequency of the faulted drive was set at 17 Hz. The fault path resistance R_f =42 Ω. The detection time was 1.2 ms. The threshold was 39 mA without delay for initialization time and 15 mA when the delay was applied.

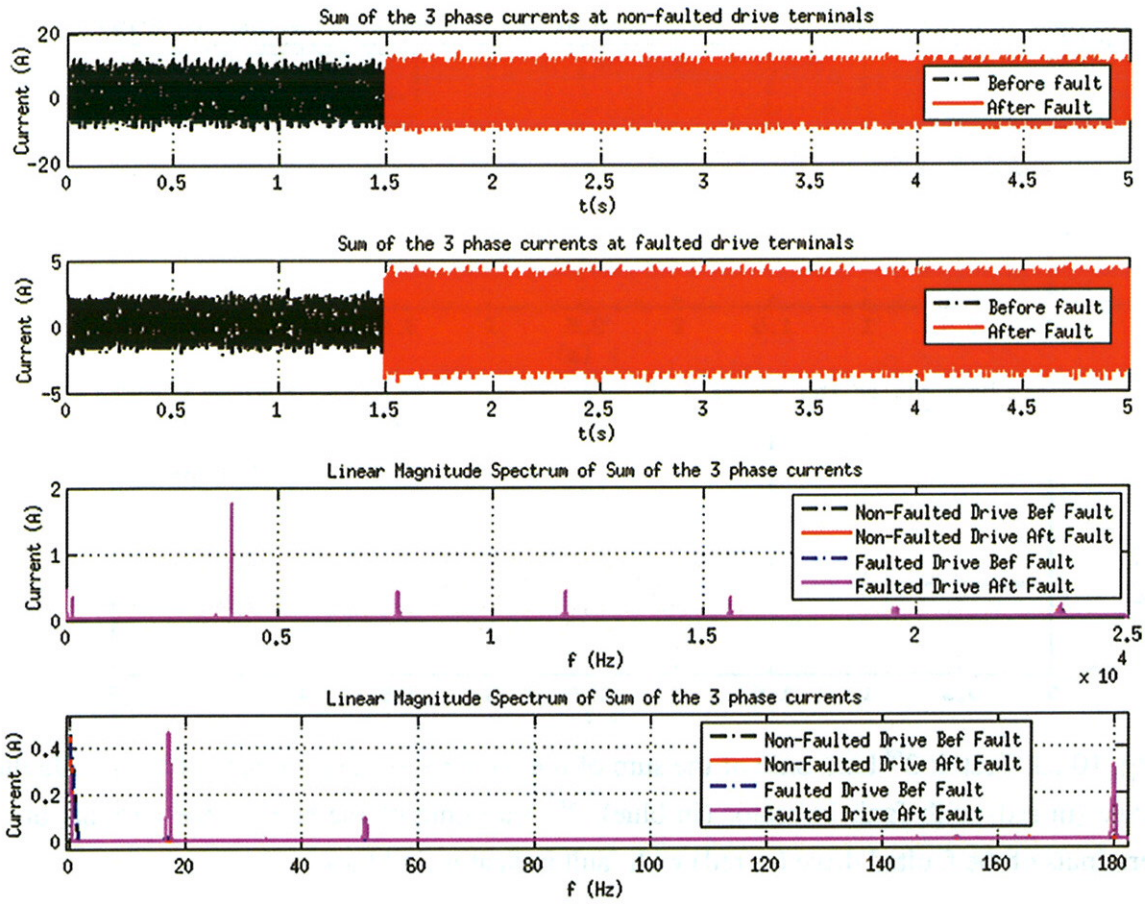

Fig. 10.24. Test 4: Sum of the 3 output currents at non-faulted drive terminals, sum of the 3 output currents at the faulted drive terminals, linear magnitude spectrum of the sum of the 3 output currents and detail of the magnitude spectrum at tracked frequency

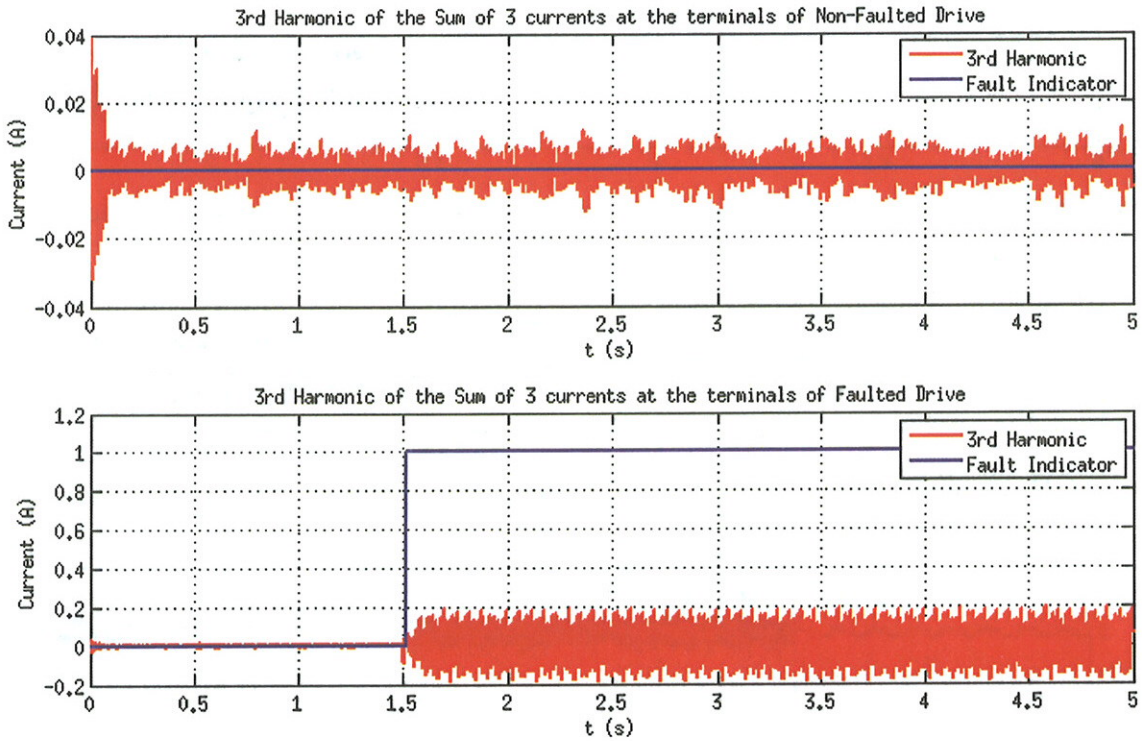

Fig. 10.25. Test 4: 3rd harmonic of the sum of the currents at the terminals of the non-faulted drive (in red) with fault indicator (in blue), 3rd harmonic of the sum of the currents at the terminals of the faulted drive (in red) with fault indicator (in blue)

10.3. Comparison of simulation and experimentation results

In this section, a comparison of simulation and experimentation results is made for 2 drives operating in parallel. For this case, both drives, faulted and non-faulted, were operated at 17 Hz. Both setups are similar to the one used in the previous section.

In Fig. 10.26, the tracked 3rd harmonic of the sum of the 3 output currents at the terminals of the non-faulted drive and the fault indicator are depicted. In Fig. 10.27, the tracked 3rd harmonic of the sum of the 3 output currents at the terminals of the faulted drive and the fault indicator are depicted. In Fig 10.28, the tracked 3rd harmonic of the sum of the output currents and the fault indicator for the experimental faulted drive are shown. In Figs 10.29-31 details of Figs. 10.26-28, respectively, are presented.

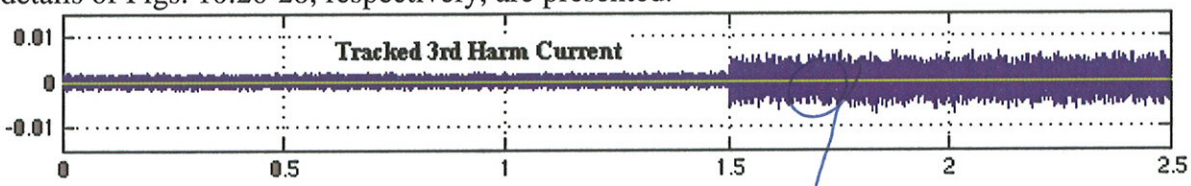

Fig. 10.26. Simulation, non-faulted drive: Tracked 3rd harmonic of the sum of output currents and fault indicator

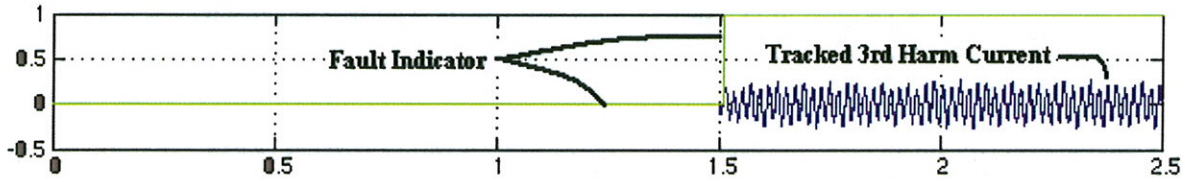

Fig. 10.27. Simulation, faulted drive: Tracked 3rd harmonic of the sum of the output currents and fault indicator

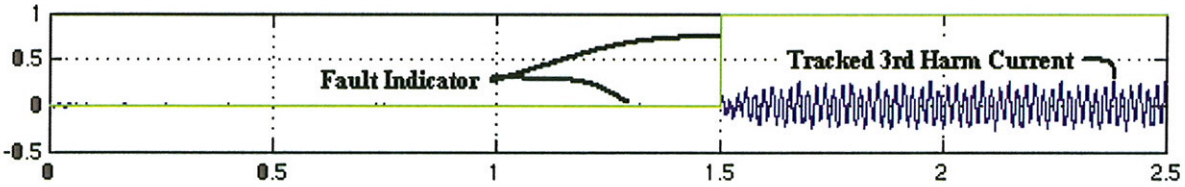

Fig. 10.28. Experimentation, faulted drive: Tracked 3rd harmonic of the sum of the output currents and fault indicator

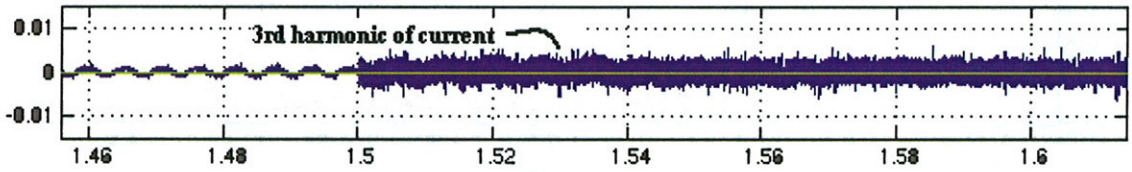

Fig. 10.29. Simulation, non-faulted drive: Detail of Fig. 10.26

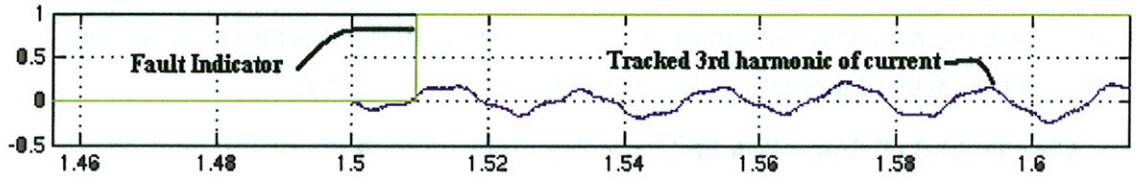

Fig. 10.30. Simulation, faulted drive: Detail of Fig. 10.27

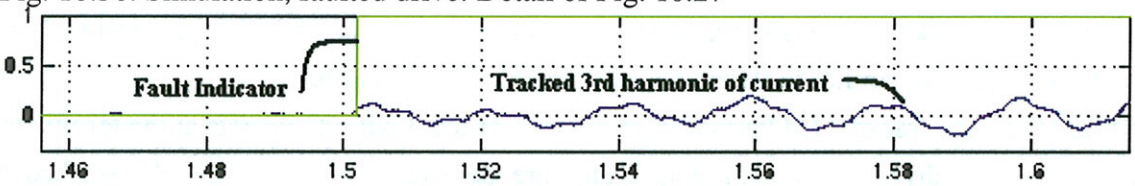

Fig. 10.31. Experimentation, faulted drive: Detail of Fig. 10.28

11. CONCLUSIONS AND FUTURE RESEARCH

A line-to-ground fault detection method that has desirable characteristics like immunity to ground loops magnetic contamination, modularity, ~~easiness to set threshold~~ ~~with~~ no additional costs ~~added~~ has been developed. In Table 11.1, a comparison between the 5 current-signature-based line-to-ground fault detection methods listed in Chapter 3 (M1-M5) and the method developed in this dissertation (M6) is presented.

The characteristics evaluated of the several methods are: 1) ~~Reliability, which answers~~ the question is detection affected by ground loops?, 2) Modularity, which answers the question is it possible to detect which drive has the fault in a multi-drive system?, 3)Easiness to set threshold, which answers the question is it easy to set the threshold of the signal used for detection in a multi-drive and reconfigurable (any ASD turned-on or turned-off at any instant), 4) Extra DSP, which answers the question is it required to have extra digital signal processing capability to detect the occurrence of a line-to-ground fault?, 5) Extra HW, which answers the question is it required to add hardware to the system in order to detect the occurrence of the line-to-ground fault?

The reliability of method M1 depends on the signal that is chosen to be utilized for detection of the occurrence of the fault. The recommended signal is the fundamental of the operating frequency of the drive which is hard to determine in multi-drive systems and it is signature affected by ground loops. Method M3 is modular, but uses signature that corresponds to the fundamental of the operating frequency of the inverter.

Method M2 is reliable, modular and the threshold of the signal used for detection is easy to set. However, its reliability depends on the signal injected. As a rule of thumb, a high frequency signal is preferred. Furthermore, though the method is modular, it requires trained personnel to determine the occurrence of the fault, which could take a long time. Finally, the easiness to set the threshold depends on the signal selected to be injected. In many cases such a signal is determined by trial and error with more trial and error if the topology of the system changes due to expansion, for instance.

Methods M4 and M5 present most of the disadvantages of any of the methods compared. The reliability to detect a fault based on any of these 2 methods depends on the accuracy with which the threshold is set. In multi-drive systems with long cables, this is difficult and requires trial and error or extensive simulation and tweaking.

Method M6, the one developed in this dissertation is the one with the most advantages among the methods compared. As it was demonstrated in Chapter 7, this method is immune to contamination magnetically coupled due to ground loops. It is modular and easily applicable to multi-drive systems as it was discussed in Chapter 8. The threshold is easy to set because the signature selected has been shown to be the least prone to be affected by ground loops, operating conditions of the ASD and topology of a multi-drive system. Furthermore, the signature selected is low-frequency which does not require extra digital signal processing capability or added hardware.

Table 11.1. Comparison of current-signature-based line-to-ground fault detection methods

	Reliable?	Modular?	Easy to set threshold level?	Extra DSP?	Extra HW?
M1	Yes.	No.	No.	Yes.	Yes.
M2	Yes.	Yes.	Yes.	Yes.	Yes.
M3	No.	Yes.	No.	No.	Yes.
M4	No.	No.	No.	Yes.	Yes.
M5	No.	No.	No.	Yes.	Yes.
M6	Yes.	Yes.	Yes.	No.	No.

11.1. Conclusions of this dissertation

11.2. Future research

APPENDICES

APPENDIX A
FEA FOR CABLES

A.1. Comparison of cable electric parameters: 1) measured with an LCR and 2) calculated using FEA

A.1.1. Measurement of cable electric parameters using LCR meter

An LCR meter (HP 4284A: Freq. range 20 Hz-1MHz) and Kelvin clip leads (HP16089A leads: Freq. range 10 Hz – 100 kHz) used to measure cable parameters) was used to measure the resistance, inductance and capacitance parameters of the 3-phase cables as a function of the frequency in various differential-mode and common-mode configurations as shown in Figs. A.1-3. A detailed test procedure is provided in section A.4. The computer simulation models for common-mode analysis use the parameters of the line-ground 3-wire configurations.

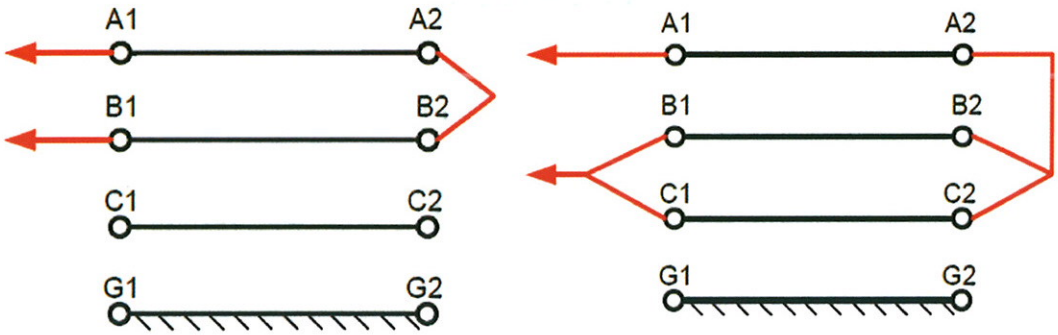

Fig. A.1. Differential Mode cable configurations to determine inductance and series resistance (Ls, Rs): (a) Line-line 2-wire and (b) Line-line 3-wire

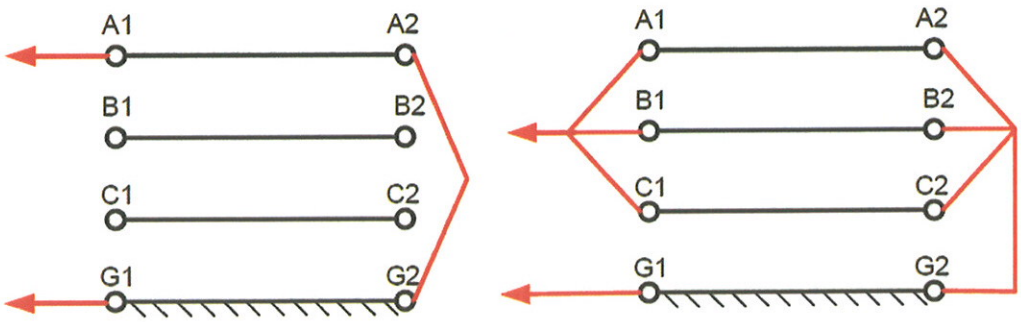

Fig. A.2. Common Mode cable configurations to determine inductance and series resistance (Ls, Rs): (a) Line-to-ground 1-wire and (b) Line-to-ground 3-wire

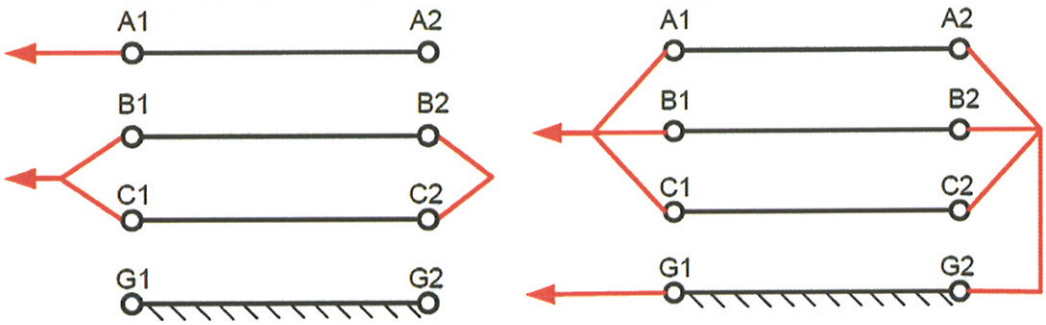

Fig. A.3. Cable configurations to measure capacitance (Cp, Rp): (a) Differential-mode line-line 3-wire and (b) Common-mode line-ground 3-wire.

The **R** and **L** parameters of a cable can be represented by 5 X 5 symmetrical matrices and the **C** parameters can be represented by a 3 X 3 symmetric matrix as follows. The off-diagonal elements in **R** are due to proximity effect; and they are neglected. In the **L** matrix, the diagonal elements represent the self-inductances and the off-diagonal elements represent the mutual inductances. It has been shown in [27] that the **R** and **L** matrices vary with frequency while the **C** matrix does not show significant change with frequency.

$$\mathbf{R} = \begin{bmatrix} R_{Ar} & R_{Arg} & R_{Aru} & R_{Arv} & R_{Arw} \\ R_{Arg} & R_{g} & R_{gu} & R_{gv} & R_{gw} \\ R_{Aru} & R_{gu} & R_{u} & R_{uv} & R_{uw} \\ R_{Arv} & R_{gv} & R_{uv} & R_{v} & R_{vw} \\ R_{Arw} & R_{gw} & R_{uw} & R_{vw} & R_{w} \end{bmatrix} \tag{A.1}$$

$$\mathbf{L}=\begin{bmatrix} L_{Ar} & M_{Arg} & M_{Aru} & M_{Arv} & M_{Arw} \\ M_{Arg} & L_g & M_{gu} & M_{gv} & M_{gw} \\ M_{Aru} & M_{gu} & L_u & M_{uv} & M_{uw} \\ M_{Arv} & M_{gv} & M_{uv} & L_v & M_{vw} \\ M_{Arw} & M_{gw} & M_{uw} & M_{vw} & L_w \end{bmatrix} \quad \text{(A.2)}$$

$$\mathbf{C}=\begin{bmatrix} C_{ug} & C_{uv} & C_{uw} \\ C_{uv} & C_{vg} & C_{vw} \\ C_{uw} & C_{vw} & C_{wg} \end{bmatrix} \quad \text{(A.3)}$$

The measured inductance (L_{eff}) and capacitance (C_{eff}) for configurations shown in Figures 2-4 can be related to the L matrix of (1) as follows, assuming symmetry between the 3 phases

Line-line 3-wire

$$L_{eff}=\frac{1}{3}(La-Mab) \quad \text{(A.4)}$$

$$C_{eff}=2C_{ab}+\frac{2}{3}C_{ag} \quad \text{(A.5)}$$

Line-to-ground 3-wire

$$L_{eff}=\frac{1}{3}\left(L_u+M_{uv}+M_{uw}-M_{gv}-M_{gw}\right)+\frac{1}{2}\left(L_g-M_{Aru}+M_{Arg}\right)-\frac{5}{6}M_{ug} \quad \text{(A.6)}$$

$$C_{eff}=3C_{ug} \quad \text{(A.7)}$$

A.1.2. Calculation of cable electric parameters using FEA [27]

A.1.1.1. Cable structure for FEA

FEA 2D modeling software was focused on a 2 AWG cross-linked polyethylene (XLPE) 3-conductor cable (stranded) with 3 symmetrical bare grounds (stranded) and 2-mil copper foil tape shield. The FE software uses an electrostatic field solver to determine the capacitance matrix and eddy current solver to determine inductance and series resistance matrices as a function of frequency. Skin and proximity effects are included in the solution. The simplified geometry shown in Fig. A.4(c) drastically reduced simulation time without significantly compromising on accuracy. Cable parameter matrices were obtained at frequencies ranging from DC-1 MHz.

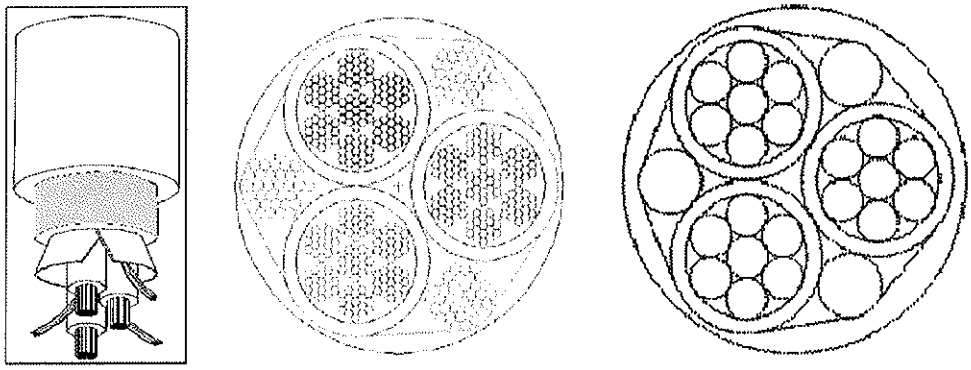

Fig. A.4. Shielded and bundled cable studied for FEA parameter extraction: (a) 3D physical outline (b) Detailed cross-sectional geometry showing stranded wire (c) Simplified geometry for FEA simulation.

A.1.1.2. Resistance / Inductance Matrices of Cable vs. Frequency

The **R** and **L** matrices obtained from FEA at different frequencies (100 Hz, 1 KHz, 10 KHz, 100 KHz, 1 MHz) are similar to those presented in (A.1-3). Computer simulations require **R** and **L** matrices corresponding to the cable oscillation frequency to obtain correct reflected wave peak voltage, damping and common-mode current. It was noted that the off-diagonal elements in the **R** matrix are small and can be neglected for simulation.

A.1.1.3. Cable Capacitance Matrix

The FEA electrostatic field solver cannot compute variation of capacitance with frequency. It was confirmed by laboratory measurements that the C matrix has negligible change with frequency. The FEA output **C** matrix has an interpretation based on solving for electrostatic charge (Q) using the equations $Q = CV$ and $\sum Q = 0$ in Fig. A.5 [95]. The system of Fig. A.5 can be represented by 3 linear equations expressing charge (Q) as a function of voltage (V).

$$\begin{aligned} Q_1 &= c_{11}V_1 + c_{12}V_2 + c_{13}V_3 \\ Q_2 &= c_{21}V_1 + c_{22}V_2 + c_{23}V_3 \\ Q_3 &= c_{31}V_1 + c_{32}V_2 + c_{33}V_3 \end{aligned} \tag{A.8}$$

The electrostatic solver output capacitance matrix contains coefficients c_{ii} called coefficients of capacitance while the off diagonal c_{ij} are called coefficients of induction,

which interestingly have negative values. If a (+) Q_i exists on the i^{th} conductor, then V_i will be (+), but charge Q_j induced on the j^{th} conductor will be (-). Hence, c_{ii} coefficients of capacitance are positive, while coefficients of induction c_{ij} are negative. Also, from symmetry $c_{ij} = c_{ji}$. System of equations (A.8) can be rewritten based on Fig. A.5 as in (A.9)

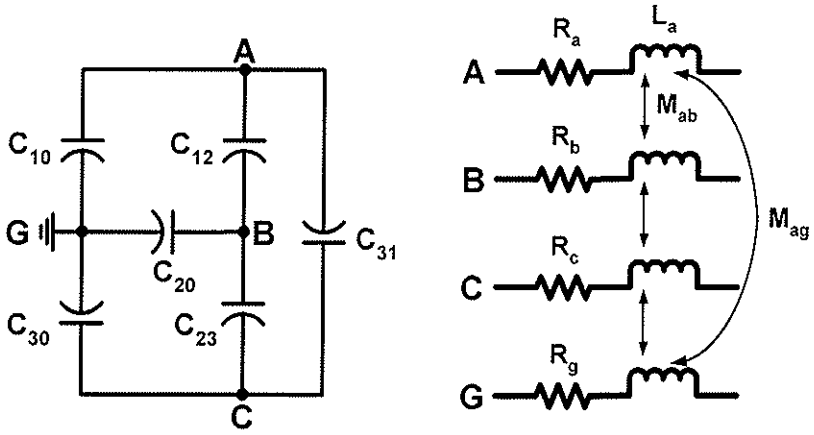

Fig. A.5. Circuit schematic showing the different parameters that can be obtained from the FEA solver.

$$\begin{aligned} Q_1 &= C_{10}V_1 + C_{12}(V_1 - V_2) + C_{13}(V_1 - V_3) \\ Q_2 &= C_{12}(V_2 - V_1) + C_{20}V_2 + C_{23}(V_2 - V_3) \\ Q_3 &= C_{13}(V_3 - V_1) + C_{23}(V_3 - V_2) + C_{30}V_3 \end{aligned} \tag{A.9}$$

In (5) the conductor-to-ground capacitances (C_{10}, C_{20}, C_{30}) are called self-partial capacitances and the line-line capacitances (C_{ij}) are called mutual partial capacitances. Equation (A.9) can be rearranged to form a Y-coefficient matrix as in (A.10).

$$\begin{aligned} Q_1 &= (C_{10} + C_{12} + C_{13})V_1 - C_{12}V_2 - C_{13}V_3 \\ Q_2 &= -C_{12}V_1 + (C_{20} + C_{12} + C_{23})V_2 - C_{23}V_3 \\ Q_3 &= -C_{13}V_1 - C_{23}V_2 + (C_{30} + C_{13} + C_{23})V_3 \end{aligned} \tag{A.10}$$

The coefficients in (A.8) can thus be related to the capacitances shown in Fig. A.5 using (A.8) and (A.9) to obtain (A.11)

$$\begin{aligned} c_{11} &= C_{10} + C_{12} + C_{13} & c_{12} &= -C_{12} \\ c_{22} &= C_{12} + C_{20} + C_{23} & c_{23} &= -C_{23} \\ c_{33} &= C_{13} + C_{23} + C_{30} & c_{13} &= -C_{13} \end{aligned} \tag{A.11}$$

Thus, the coefficient of capacitance c_{ii} is equal to the total capacitance between conductor i and ground, with all other conductors shorted to ground in Fig. A.5. The c_{ij} coefficients of induction are the negative of the mutual partial capacitances C_{ij}.

However, nodal circuit simulation programs require a physical realizable matrix of the form in (A.1-3) using C_{10}, C_{20}, and C_{30} conductor-to-ground self-partial capacitances and C_{ij} line-line mutual partial capacitances. The C_{ij} terms can be determined from above. Conductor-to-ground self-partial capacitances for the nodal matrix are:

$$\begin{aligned} C_{10} &= c_{11} + c_{12} + c_{13} \\ C_{20} &= c_{12} + c_{22} + c_{23} \\ C_{30} &= c_{13} + c_{23} + c_{33} \end{aligned} \qquad \mathbf{C} = \begin{bmatrix} C_{ag} & C_{ab} & C_{ac} \\ C_{ab} & C_{bg} & C_{bc} \\ C_{ac} & C_{bc} & C_{cg} \end{bmatrix} = \begin{bmatrix} C_{10} & C_{12} & C_{13} \\ C_{12} & C_{20} & C_{23} \\ C_{13} & C_{23} & C_{30} \end{bmatrix} \tag{A.11}$$

Once the C matrix similar to (A.1-3) is obtained in (A.12), a 3-phase drive-cable-motor simulation program such as PSpice™ or Simplorer™ can utilize these R, L and C transmission line cable parameters [27] with a 3-phase induction motor model [31] for computer simulations of peak motor voltage and common-mode current.

A.1.3. Comparison of some results

Parameters of a 2-mil, 2 AWG copper tape shielded cable were measured using an LCR meter, in a frequency range from 20 Hz to 1 MHz and also modeled in FE software to obtain the R, L and C matrices.

Plots of inductance and series resistance vs. frequency are shown in Figs. A.6-7. for line-line 3-wire DM and line-ground 3-wire CM configurations. The series resistance and inductance values show similar parameter trends with measured data, with a difference of about 15 % - 20 % for the inductance at high frequencies. Inductance and resistance differences can be attributed to several factors including limitations of 2-D modeling (cannot account for 3-D effects such as twisting of conductors), accuracy of FEA simulation (typically about 5%), LCR meter measurement accuracy and the fact that solid-grouped conductor approximations were used in lieu of the multi-strand wires.

Inductances ~~trend toward a plateau value~~ decrease at high frequency due to internal self inductances of the wire tends toward zero due to skin effect, so only external self and mutual inductances remain. Skin and proximity effects of the resistance at higher

frequency are clearly seen and would require modeling the finer strands more accurately to improve on the error. Differences between LCR measurements and FEA inductance/resistance simulations are about 5 – 10 %.

a)

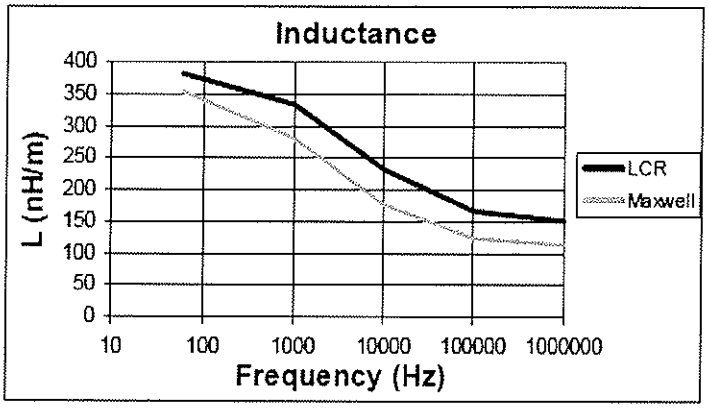

b)

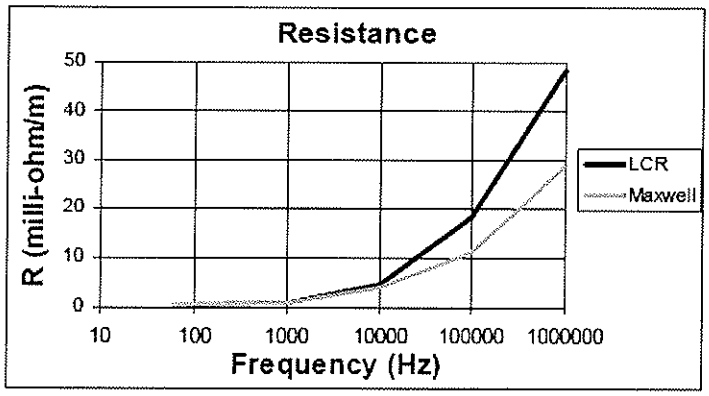

Fig. A.6. Focus cable: a) Inductance, b) resistance for line-line 3-wire differential mode

The 3-wire common mode capacitance of focus cable predicted by FEA was within 5% of measured LCR values. The 3-wire DM capacitance of the focus cable FEA prediction was within 20 % of the measured LCR value. Differences can be attributed to several factors including value of dielectric constant of conductor insulation, accuracy of FE simulation (typically about 5%) and LCR meter measurement accuracy. The cable capacitance does not change with frequency.

Table A.1: Capacitance of focus cable

Configuration	LCR measurement (pF/m)	Maxwell (pF/m)
Line-line 3-wire	196	244
Line-to-ground 3-wire	717	751

a)

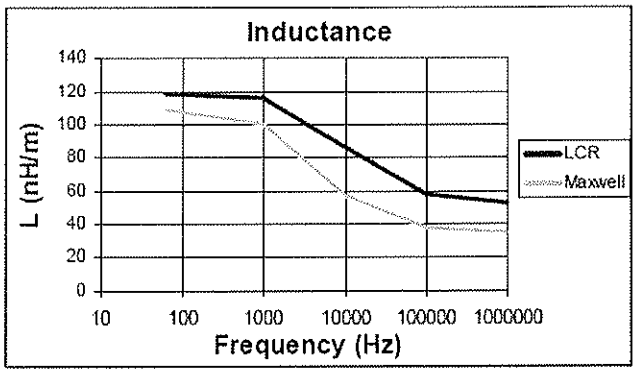

b)

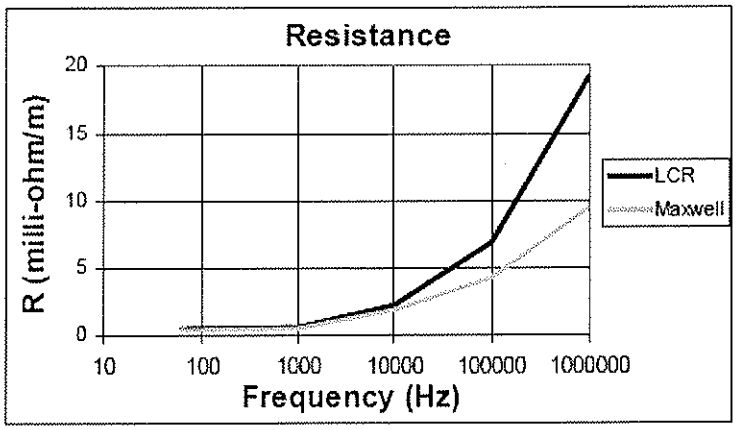

Fig. A.7. Focus cable: a) Inductance and b) resistance for line-line 3-wire common mode.

The cable characteristic impedance (Zc) plotted in Fig. A.8 is calculated from line-line two-wire inductance and line-ground capacitance as Zc = $\sqrt{L/C}$. Zc is about 45 Ω at 60 Hz fundamental frequency and reduces to about 30 Ω in the 100 KHz – 1 MHz range due to variation of inductance with frequency as described earlier.

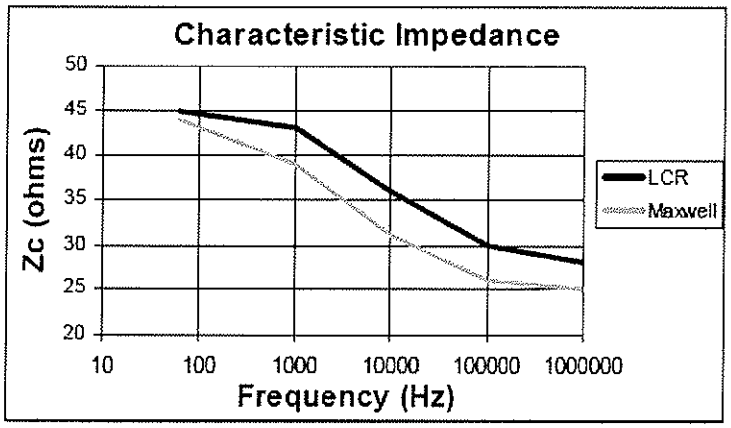

Fig. A.8. Focus cable: Characteristic Impedance.

A.2. Procedure for Cable Impedance Measurements with HP 4284A / HP 4285 LCR Meter

A.2.1. Choosing length of cable

In very short cables accurate measurement of cable parameters is difficult due to the resolution of the LCR meter. In [96], 45 m of cable is used for accuracy of the measurement. In very long cables, reflected wave phenomena need to be accounted for [18]. In [96], it is shown that if the PWM pulses take longer than one-third the rise time to travel from the inverter to the motor, then a full reflection will occur at the motor and the pulse amplitude will approximately double. Moreover, the speed of the PWM pulses in an electric cable is approximately half the speed of light (150 m/μs – 200 m/μs). Therefore, if 400 ns rise/fall edges are being used a maximum length of about 150 m/μs*400 ns = 60 m should be used, being recommended around 50 m.

A.2.2. LCR meter set-up

- Calibrate the LCR meter per manufacturer specifications. Perform the OPEN, SHORT and CABLE correction tests to calibrate the meter.
- Use the highest frequency rated terminal fixtures possible. The HP16089A fixture (Kelvin clip leads) is rated at 100 kHz with a 1m long cable. The HP47047C is rated at 40 MHz, but has no cable, which makes it difficult to connect to the device under test.

- Set the following measurement options: Test Signal Level = 1 V, Range = AUTO, Delay Time = 0 and Integration Time = MED or LONG
- Choose the {Rs, Ls} mode for measuring cable inductance and {Rp, Cp} mode for measuring cable capacitance.

A.2.3. Cable set-up

Connect the cable in the desired common-mode or differential-mode configurations to measure inductance or capacitance, as depicted in Figures A.1-3. Connect the cable to the terminal fixture on the LCR meter.

A.2.4. Record Impedance Measurements

- Make the measurements at the following frequencies over the instrument's range: (HP 4284A: 20, 100, 200, 500, 1K, 2K, 5K, 10K, 20K, 50K, 100K, 200K, 500K, 1M) (HP4285: 75K, 100K, 200K, 500 K, 1M, 2M, 5M, 10M, 20M, 30M)
- For inductance measurements, record the {Rs, Ls} values and for capacitance measurements, record the {Rp, Cp} values. (NOTE: Record only the positive values, negative values are erroneous data)

A.3. Cable electric parameters for 3 conductor-3 ground, symmetrical cable

In this section, electric cable distributed parameters are given for several cable gauges. These parameters are calculated at an operating frequency of 10 KHz.

Table A.2. Some cable dimensions

Cable	R_c (mm)	D_i (mm)	D (mm)	R_g (mm)
500 MCM	10.3505	1.651	24.003	3.759
350 MCM	8.6485	1.651	20.599	3.759
4_0	6.7185	1.397	16.231	2.9845
3_0	5.9815	1.397	14.757	2.362
2_0	5.334	1.397	13.462	2.362
1_0	4.75	1.397	12.294	2.362
1	4.229	1.397	11.252	2.362
4	2.9845	1.143	8.255	1.854
6	2.362	1.143	7.01	1.486
8	1.854	1.143	5.994	1.486
10	1.486	0.762	4.496	1.181

12	1.181	0.762	3.886	0.94
14	0.9398	0.762	3.4036	0.7365

A.3.1. 500 MCM

Table A.3. Capacitance **C** matrix (pF/m)

	A	B	C
A	290.1	45	45
B	45	290.1	45
C	45	45	290.1

Table A.4. Inductance **L** matrix (uH/m)

	Ar	G	A	B	C
Ar	1.196	1.197	1.197	1.197	1.197
G	1.197	1.328	1.255	1.255	1.255
A	1.197	1.255	1.435	1.216	1.216
B	1.197	1.255	1.216	1.435	1.216
C	1.197	1.255	1.216	1.216	1.435

Table A.5. Resistance **R** matrix (mΩ/m)

	Ar	G	A	B	C
Ar	0.179	0	0	0	0
G	0	0.13	0	0	0
A	0	0	0.051	0	0
B	0	0	0	0.051	0
C	0	0	0	0	0.051

A.3.2. 350 MCM

Table A.6. Capacitance **C** matrix (pF/m)

	A	B	C
A	265.4	40.1	40.1
B	40.1	265.4	40.1
C	40.1	40.1	265.4

Table A.7. Inductance **L** matrix (uH/m)

	Ar	G	A	B	C
Ar	1.226	1.227	1.227	1.227	1.227
G	1.227	1.342	1.279	1.279	1.279
A	1.227	1.279	1.471	1.247	1.247
B	1.227	1.279	1.247	1.471	1.247
C	1.227	1.279	1.247	1.247	1.471

Table A.8. Resistance **R** matrix (mΩ/m)

	Ar	G	A	B	C
Ar	0.21	0	0	0	0
G	0	0.13	0	0	0
A	0	0	0.074	0	0
B	0	0	0	0.074	0
C	0	0	0	0	0.074

A.3.3. 4_0

Table A.9. Capacitance **C** matrix (pF/m)

	A	B	C
A	252	37.8	37.8
B	37.8	252	37.8
C	37.8	37.8	252

Table A.10. Inductance **L** matrix (uH/m)

	Ar	G	A	B	C
Ar	1.235	1.237	1.237	1.237	1.237
G	1.237	1.352	1.289	1.289	1.289
A	1.237	1.289	1.485	1.258	1.258
B	1.237	1.289	1.258	1.485	1.258
C	1.237	1.289	1.258	1.258	1.485

Table A.11. Resistance **R** matrix (mΩ/m)

	Ar	G	A	B	C
Ar	0.26	0	0	0	0
G	0	0.21	0	0	0
A	0	0	0.12	0	0
B	0	0	0	0.12	0
C	0	0	0	0	0.12

A.3.4. 3_0

Table A.12. Capacitance **C** matrix (pF/m)

	A	B	C
A	234.2	34.2	34.2
B	34.2	234.2	34.2

C	34.2	34.2	234.2

Table A.13. Inductance **L** matrix (uH/m)

	Ar	G	A	B	C
Ar	1.253	1.255	1.255	1.255	1.255
G	1.255	1.386	1.315	1.315	1.315
A	1.255	1.315	1.508	1.277	1.277
B	1.255	1.315	1.277	1.508	1.277
C	1.255	1.315	1.277	1.277	1.508

Table A.14. Resistance **R** matrix (mΩ/m)

	Ar	G	A	B	C
Ar	0.287	0	0	0	0
G	0	0.33	0	0	0
A	0	0	0.154	0	0
B	0	0	0	0.154	0
C	0	0	0	0	0.154

A.3.5. 2_0

Table A.15. Capacitance **C** matrix (pF/m)

	A	B	C
A	221.1	31.8	31.8
B	31.8	221.1	31.8
C	31.8	31.8	221.1

Table A.16. Inductance **L** matrix (uH/m)

	Ar	G	A	B	C
Ar	1.226	1.228	1.228	1.228	1.228
G	1.228	1.35	1.284	1.284	1.284
A	1.228	1.284	1.486	1.251	1.251
B	1.228	1.284	1.251	1.486	1.251
C	1.228	1.284	1.251	1.251	1.486

Table A.17. Resistance **R** matrix (mΩ/m)

	Ar	G	A	B	C
Ar	0.314	0	0	0	0
G	0	0.33	0	0	0
A	0	0	0.194	0	0
B	0	0	0	0.194	0
C	0	0	0	0	0.194

A.3.6. 1_0

Table A.18. Capacitance **C** matrix (pF/m)

	A	B	C
A	208	29.4	29.4
B	29.4	208	29.4
C	29.4	29.4	208

Table A.19. Inductance **L** matrix (uH/m)

	Ar	G	A	B	C
Ar	1.217	1.219	1.219	1.219	1.219
G	1.219	1.331	1.272	1.272	1.272
A	1.219	1.272	1.483	1.242	1.243
B	1.219	1.272	1.242	1.483	1.242
C	1.219	1.272	1.243	1.242	1.483

Table A.20. Resistance **R** matrix (mΩ/m)

	Ar	G	A	B	C
Ar	0.342	0	0	0	0
G	0	0.33	0	0	0
A	0	0	0.244	0	0
B	0	0	0	0.244	0
C	0	0	0	0	0.244

A.3.7. 1 AWG

Table A.21. Capacitance **C** matrix (pF/m)

	A	B	C
A	196.5	27.2	27.2
B	27.2	196.5	27.2
C	27.2	27.2	196.5

Table A.22. Inductance **L** matrix (uH/m)

	Ar	G	A	B	C
Ar	1.233	1.235	1.235	1.235	1.235
G	1.235	1.338	1.284	1.284	1.284
A	1.235	1.284	1.505	1.259	1.259
B	1.235	1.284	1.259	1.505	1.259
C	1.235	1.284	1.259	1.259	1.505

Table A.23. Resistance **R** matrix (mΩ/m)

	Ar	G	A	B	C
Ar	0.372	0	0	0	0
G	0	0.33	0	0	0
A	0	0	0.308	0	0
B	0	0	0	0.308	0
C	0	0	0	0	0.308

A.3.8. 4 AWG

Table A.24. Capacitance **C** matrix (pF/m)

	A	B	C
A	180.5	24.5	24.5
B	24.5	180.5	24.5
C	24.5	24.5	180.5

Table A.25. Inductance **L** matrix (uH/m)

	Ar	G	A	B	C
Ar	1.291	1.294	1.294	1.294	1.294
G	1.294	1.392	1.342	1.342	1.342
A	1.294	1.342	1.575	1.321	1.321
B	1.294	1.342	1.321	1.575	1.321
C	1.294	1.342	1.321	1.321	1.575

Table A.26. Resistance **R** matrix (mΩ/m)

	Ar	G	A	B	C
Ar	0.499	0	0	0	0
G	0	0.535	0	0	0
A	0	0	0.619	0	0
B	0	0	0	0.619	0
C	0	0	0	0	0.619

A.3.9. 6 AWG

Table A.27. Capacitance **C** matrix (pF/m)

	A	B	C
A	158.6	20.3	20.3
B	20.3	158.6	20.3

C	20.3	20.3	158.6

Table A.28. Inductance **L** matrix (uH/m)

	Ar	G	A	B	C
Ar	1.209	1.213	1.213	1.213	1.213
G	1.213	1.32	1.266	1.266	1.266
A	1.213	1.266	1.51	1.242	1.242
B	1.213	1.266	1.242	1.51	1.242
C	1.213	1.266	1.242	1.242	1.51

Table A.29. Resistance **R** matrix (mΩ/m)

	Ar	G	A	B	C
Ar	0.581	0	0	0	0
G	0	0.833	0	0	0
A	0	0	0.989	0	0
B	0	0	0	0.989	0
C	0	0	0	0	0.989

A.3.10. 8 AWG

Table A.30. Capacitance **C** matrix (pF/m)

	A	B	C
A	133.5	17.1	17.1
B	17.1	133.5	17.1
C	17.1	17.1	133.5

Table A.31. Inductance **L** matrix (uH/m)

	Ar	G	A	B	C
Ar	1.235	1.24	1.24	1.24	1.24
G	1.24	1.333	1.29	1.29	1.29
A	1.24	1.29	1.56	1.274	1.274
B	1.24	1.29	1.274	1.56	1.274
C	1.24	1.29	1.274	1.274	1.56

Table A.32. Resistance **R** matrix (mΩ/m)

	Ar	G	A	B	C
Ar	0.663	0	0	0	0
G	0	0.833	0	0	0
A	0	0	1.605	0	0
B	0	0	0	1.605	0
C	0	0	0	0	1.605

A.3.11. 10 AWG

Table A.33. Capacitance **C** matrix (pF/m)

	A	B	C
A	133.6	19.9	19.9
B	19.9	133.6	19.9
C	19.9	19.9	133.6

Table A.34. Inductance **L** matrix (uH/m)

	Ar	G	A	B	C
Ar	1.223	1.229	1.229	1.229	1.229
G	1.229	1.326	1.286	1.286	1.286
A	1.229	1.286	1.546	1.274	1.274
B	1.229	1.286	1.274	1.546	1.274
C	1.229	1.286	1.274	1.274	1.546

Table A.35. Resistance **R** matrix (mΩ/m)

	Ar	G	A	B	C
Ar	0.836	0	0	0	0
G	0	1.318	0	0	0
A	0	0	2.498	0	0
B	0	0	0	2.498	0
C	0	0	0	0	2.498

A.3.12. 12 AWG

Table A.36. Capacitance **C** matrix (pF/m)

	A	B	C
A	133.8	16.4	16.4
B	16.4	133.8	16.4
C	16.4	16.4	133.8

Table A.38. Inductance **L** matrix (uH/m)

	Ar	G	A	B	C
Ar	1.255	1.261	1.261	1.261	1.261
G	1.261	1.365	1.32	1.32	1.32
A	1.261	1.32	1.591	1.303	1.303
B	1.261	1.32	1.303	1.591	1.303
C	1.261	1.32	1.303	1.303	1.591

Table A.39. Resistance **R** matrix (mΩ/m)

	Ar	G	A	B	C
Ar	0.989	0	0	0	0
G	0	2.081	0	0	0
A	0	0	3.955	0	0
B	0	0	0	3.955	0
C	0	0	0	0	3.955

A.3.13. 14 AWG

Table A.40. Capacitance **C** matrix (pF/m)

	A	B	C
A	119.2	13.4	13.4
B	13.4	119.2	13.4
C	13.4	13.4	119.2

Table A.41. Inductance **L** matrix (uH/m)

	Ar	G	A	B	C
Ar	1.1971	1.204	1.204	1.204	1.204
G	1.204	1.324	1.272	1.272	1.272
A	1.204	1.272	1.557	1.249	1.249
B	1.204	1.272	1.249	1.557	1.249
C	1.204	1.272	1.249	1.249	1.557

Table A.42. Resistance **R** matrix (mΩ/m)

	Ar	G	A	B	C
Ar	1.111	0	0	0	0
G	0	3.39	0	0	0
A	0	0	6.243	0	0
B	0	0	0	6.243	0
C	0	0	0	0	6.243

A.4. Alcatel 12AWG PVC Cable Shielded Asymmetrical, 4-conductor cable

A.4.1 12 AWG

Table A.40. Capacitance **C** matrix (pF/m) - diagonal values are capacitances to shield

	A	**B**	**C**	**Shield**
A	201	75.8	75.8	2.2
B	75.8	201	2.2	75.8

C	75.8	2.2	201	75.8
Shield	2.2	75.8	75.8	201

Table A.41. Inductance **L** matrix (uH/m)

	A	**B**	**C**	**G**	**Shield**
A	1.143	0.899	0.899	0.829	0.86
B	0.899	1.143	0.829	0.899	0.86
C	0.899	0.829	1.143	0.899	0.86
G	0.829	0.899	0.899	1.143	0.86
Shield	0.86	0.86	0.86	0.86	0.86

Table A.42. Resistance **R** matrix (mΩ/m)

	A	**B**	**C**	**G**	**Shield**
A	3.94	0	0	0	0
B	0	3.94	0	0	0
C	0	0	3.94	0	0
G	0	0	0	3.94	0
Shield	0	0	0	0	5.62

APPENDIX B

MOTOR PARAMETERS FOR MOTOR MODEL USED IN CHAPTER 2

The parameters for different power ratings of the motor model (5 HP, 10 HP, 20 HP, 60 HP) developed in [31] are presented herein. Magnitude and phase response corresponding to the 15 HP motor are depicted in Figs. B.1-2.

Table B.1. Motor used in implemented test-beds: 5 HP

C_1	0.27 nF
C_2	0.87 nF
R_1	9 Ω
R_2	500 Ω
R_3	7000 Ω
R_4	0.5 Ω
L_1	2.45 mH
L_2	5.2 mH
L_3	44 nH

Table B.2. Motor used in implemented test-beds: Reliance Electric L0194A, 10 HP

C_1	0.5 nF
C_2	1.15 nF
R_1	100 Ω
R_2	190 Ω
R_3	2000 Ω
R_4	0.5 Ω
L_1	10.8 mH
L_2	6.85 mH
L_3	100 nH

Table B.3. Motor used in implemented test-beds: 20 HP

C_1	0.41 nF
C_2	1.08 nF
R_1	7 Ω
R_2	340 Ω
R_3	4400 Ω
R_4	0.5 Ω
L_1	2 mH
L_2	4.6 mH
L_3	280 nH

Table B.4. Motor used in implemented test-beds: 60 HP

C_1	1.28 nF
C_2	2.7 nF
R_1	8 Ω
R_2	710 Ω
R_3	4 Ω
R_4	0.5 Ω
L_1	0.05 mH
L_2	2.2 mH
L_3	260 nH

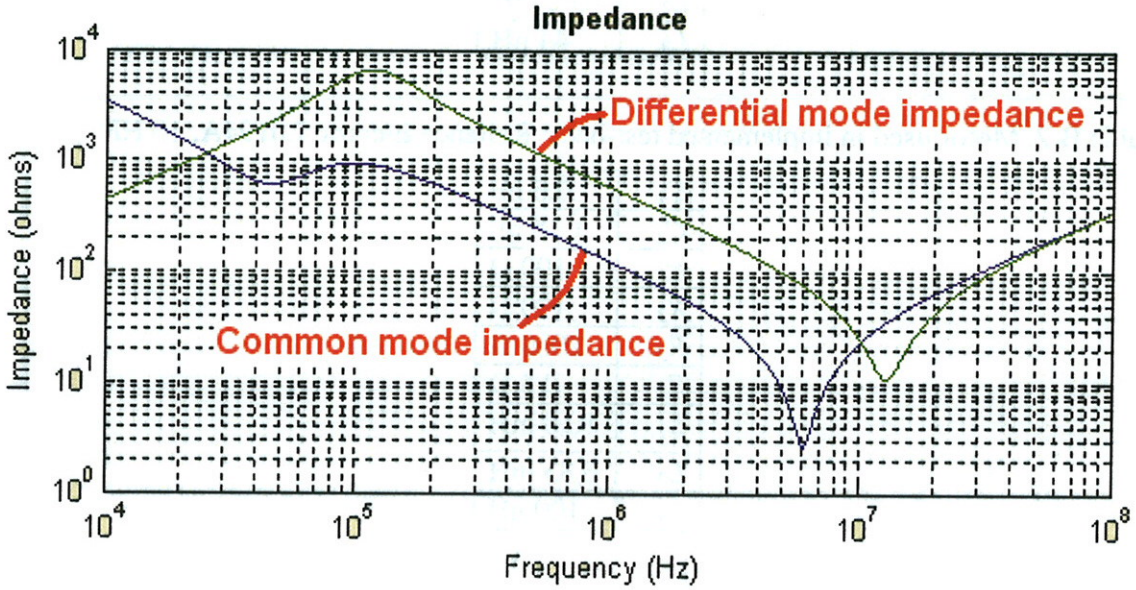

Fig. B.1. Magnitude response of the impedance of the 15 HP motor

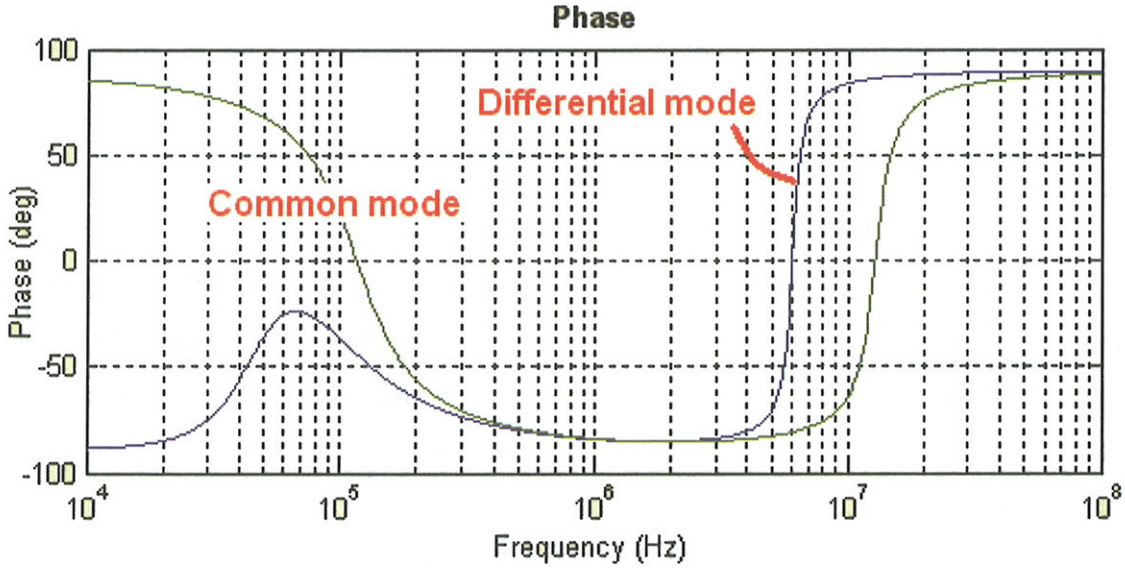

Fig. B.1. Phase response of the impedance of the 15 HP motor

APPENDIX D

FREQUENCY-BASED MODEL OF THE INVERTER

Communications theory [97], [98] is used. The thought process starts defining the sampling technique to be utilized: 1) natural or 2) regular (sample-and-hold). The sample-and-hold (S/H) technique is chosen since it makes digital implementations simpler. The carrier that the modulated signal is compared with is chosen to be a triangular waveform.

The S/H can be performed at: 1) every peak or every valley of the carrier (symmetrical S/H) or 2) at every peak and every valley (asymmetrical S/H). Only the case 1) is analyzed. Two time-variables, shown in (D.1) and in (D.2) are defined.

$$x(t) = \omega_c t + \theta_c \tag{D.1}$$

$$y(t) = \omega_{\text{mod}} t + \theta_{\text{mod}} \tag{D.2}$$

In (D.1), $\omega_{\text{mod}} = 2\pi / T_{\text{mod}}$ is the period of the fundamental waveform and θ_{mod} is an arbitrary phase offset of the angle of the fundamental waveform. In (D.2), ω_c and θ_c are similar variables for the carrier, as the ones defined for the modulated waveform. The time-variables $x(t)$ and $y(t)$ represent the time-variation of the carrier and the modulated waveform respectively. Each one of these is considered as independently periodic. The geometric wall method described initially by [99] and further expanded upon by [100] and [101], [102] is utilized to find the Fourier series of this double-variable-controlled waveform[1].

Assuming Dirichlet´s conditions for the existence of the Fourier series for the modulated waveform and the carrier hold (which for this case do), a Fourier series expansion can be determined for the double-variable-controlled waveform $f(x, y) = f(x(t), y(t))$, as shown in (D.3).

---

[1] The interested reader is prompted to specialized literature [HOLMES 2003] to understand the method of geometric wall, although, the author of this dissertation has had difficulties implementing the results presented in Section 6.4 of [HOLMES 2003].

$$f(t)=\frac{a_{00}}{2}+\sum_{n=1}^{\infty}\left(a_{0n}\cos(ny)+b_{0n}\sin(ny)\right)+\sum_{m=1}^{\infty}\left(a_{m0}\cos(mx)+b_{m0}\sin(mx)\right)+$$
$$+\sum_{m=1}^{\infty}\sum_{\substack{n=-\infty\\(n\neq 0)}}^{\infty}\left(a_{mn}\cos(mx+ny)+b_{mn}\sin(mx+ny)\right) \tag{D.3}$$

The first term in (D.3) is the DC-offset. The second term represents the fundamental component and baseband harmonics. The third term contains the carrier harmonics. And the fourth term represents the sideband harmonics. The magnitudes of the harmonic components must be evaluated for particular values of m and n. In complex form ($j=\sqrt{-1}$), such coefficients can be found from (D.4).

$$a_{mn}+jb_{mn}=\frac{1}{2\pi^2}\int_{-\pi}^{\pi}\int_{-\pi}^{\pi}f(x,y)e^{j(mx+ny)}dxdy \tag{D.4}$$

In this process, the inner and outer double Fourier integral limits for the SVPWM will be defined, which contain sinusoidal functions. When these limits are replaced in (D.4), exponential modulation (i.e., frequency modulation), as found in [97], [98] results. The Jacobi-Anger expansion [103], given in (D.5), provides a relationship between exponential modulation and Bessel functions of the first kind (J_n).

$$e^{jz\cos\theta}=J_0(z)+2\sum_{n=1}^{\infty}j^nJ_n(z)\cos(n\theta) \tag{D.5}$$

The expression in (D.5) can be manipulated to obtain (D.6).

$$\cos\left(\alpha+z\sin(\theta)\right)=\sum_{k=-\infty}^{\infty}J_k(z)\cos(\alpha+k\theta) \tag{D.6}$$

Now, using (D.5) and (D.6) in (D.4), the coefficients a_{mn} and b_{mn} can be found for the case of the inverter line-to-neutral voltage, which includes the inverter CMV, as shown in (D.7).

$$a_{mn}+jb_{mn}=$$
$$-j\frac{V_{Cap}rT_{mn}}{s\pi^2}\left(\begin{array}{l}\left(1+(-1)^n\right)\left(\left(J_0(\mu_1)-J_0(\mu_2)\right)\sin\left(\frac{n\pi}{3}\right)+J_0(\mu_2)\sin\left(\frac{n\pi}{2}\right)\right)+\\ \frac{2}{n}\sum_{k=1}^{\infty}\left(j^k\left(1+(-1)^{k+n}\right)\left(P_{1kn}J_k(\mu_1)+P_{2kn}J_k(\mu_2)\right)\right)\end{array}\right) \tag{D.7}$$

In (D.7), V_{Cap} is defined as the DC-link voltage. $r = \omega_c / \omega_{\text{mod}}$ is the ratio between carrier frequency and modulated frequency, $s = mr + n$. $M_i = 2V_{l0} / V_{Cap}$ is the modulation index (i.e., M_i=4/πM), with V_{l0} defined as the amplitude of the line-to-virtual neutral voltage of the modulator. The Bessel functions of the first type are evaluated at $\mu_1 = \sqrt{3} M \pi s / (4r)$ and $\mu_2 = 3M \pi s / (4r)$. Also, $T_{mn} = t_1 e^{-j\frac{n\pi}{r}} - (-1)^n t_2$, with $t_1 = e^{j\frac{3s\pi}{2r}}$ and $t_2 = e^{j\frac{s\pi}{2r}}$ is defined. The integrals $P_{1kn} = \int_0^{\frac{\pi}{3}} \cos(ny) \cos\left(k\left(y - \frac{\pi}{6}\right)\right) dy$ and $P_{2kn} = \int_{\frac{\pi}{3}}^{\frac{\pi}{2}} \cos(ny)\cos(ky) dy$ and (D.7) are evaluated for the case in which $k \neq |n|$.

Since (D.7) is valid only for $n \neq 0$, no carrier harmonics can be calculated (incomplete inverter CMV and line-to-neutral spectra). It is necessary to find an expression for n=0, in order to have a complete spectra of the line-to-neutral voltage and the inverter CMV after modulation.

$$a_{m0,odd} + jb_{m0,odd} = -\frac{4E}{m\pi}\sin\left(m\frac{\pi}{2}\right)\left(\begin{array}{l}\frac{1}{3}\left(2J_0(\eta_1) + J_0(\eta_2)\right) + \\ \frac{4}{\pi}\sum_{k=1}^{\infty}\left(\frac{(-1)^k}{k}\sin\left(\frac{k\pi}{3}\right)\left(J_{2k}(\eta_1) - J_{2k}(\eta_2)\cos\left(\frac{k\pi}{3}\right)\right)\right)\end{array}\right) \quad \text{(D.8)}$$

In (D.8), $\eta_1 = \sqrt{3} Mm\pi / 4$ and $\eta_2 = 3Mm\pi / 4$. The value of $a_{m0,odd} + jb_{m0,odd}$ is zero for even values of m. Expressions (D.7-8) define the full spectrum content of the line-to-middle-point-of the-DC-link-capacitor voltage. Then, the harmonic spectrum for the CMV, the line-to-line voltages and the line-to-virtual-neutral voltages can be calculated for different values of m and n. As it was established before, this calculation is valid for asymmetrical regular S/H. The cases: 1) m=0 and n=3,9,15, etc., which corresponds to 3rd harmonic and its baseband harmonics, as given by (1.17), and 2) m=1 and n=0,3,9,15, etc., which corresponds to the carrier and sideband harmonics, are found.

APPENDIX E

LCR MOTOR COMMON MODE IMPEDANCE MEASUREMENT

Table E.1. Three-wire common mode impedance for a Y-connected 5 HP, 460 V motor

F (Hz)	Z (Ω)	Theta (deg)	Z (db)
20	1.96E+06	-89.7	1.26E+02
50	7.86E+05	-89.7	1.18E+02
60	6.55E+05	-89.7	1.16E+02
100	3.94E+05	-89.7	1.12E+02
200	1.97E+05	-89.7	1.06E+02
500	7.90E+04	-89.7	9.80E+01
1000	3.96E+04	-89.6	9.20E+01
2000	1.98E+04	-89.6	8.59E+01
5000	7.90E+03	-89.4	7.80E+01
10000	3.90E+03	-88.7	7.18E+01
20000	1.89E+03	-86.5	6.55E+01
50000	660	-72.7	5.64E+01
60000	532	-64.9	5.45E+01
80000	417.8	-44.8	5.24E+01
100000	427	-27.1	5.26E+01
120000	500	-19.2	5.40E+01
150000	613	-22.5	5.57E+01
200000	615	-37	5.58E+01
250000	562	-43	5.50E+01
300000	534	-50	5.46E+01
400000	431	-64	5.27E+01
500000	330	-71	5.04E+01
600000	261	-73	4.83E+01
800000	182	-72	4.52E+01
1000000	144	-67	4.32E+01

Table E.2. Three-wire common mode impedance for a Y-connected, 20 HP, 460 V motor

f (Hz)	Z (kΩ)	theta (degrees)
100	130	-89.2
200	65.5	-89.3
500	26.4	-89.4
1000	13.3	-89.5
2000	6.6	-89.5
5000	2.7	-89.4
10000	1.3	-89.1
20000	0.649	-88.1
50000	0.23	-82
60000	0.181	-78
70000	0.141	-72

80000	0.119	-65.9
100000	0.0896	-44.8
120000	0.0899	-18.6
150000	0.139	0
160000	0.163	-0.6
166000	0.179	-2.5
200000	0.233	-22.6
250000	0.195	-47.6
300000	0.155	-54.5
500000	0.0832	-60.4

Table E.3. Three-wire CM impedance for a Y-connected, 100 HP, 460 V motor

f (Hz)	**Z (Ω)**	Theta (degrees)
100	72980	-88.46
200	36900	-88.65
500	14930	-88.85
1000	7520	-88.97
2000	3790	-89.05
5000	1520	-89.07
10000	761	-88.9
20000	374.2	-88
50000	134.74	-82.05
60000	107.05	-78.53
75000	79.59	-71.03
100000	56.57	-51.2
120000	53.29	-32.2
150000	65.34	-14.65
160000	71.41	-12.79
200000	94.04	-17.12
240000	104.46	-29.23
300000	97.51	-46.5
333333	88.83	-53
400000	73.2	-60.84
480000	60.2	-65.73
600000	46.28	-70.24
800000	34.43	-71.35
1000000	26.4	-72.6
1200000	24.47	-71.2
1500000	13.17	-64
2000000	7.27	-52.9
2250000	4.5	-46.8
2400000	2.9	-30.1
2450000	2.52	-19.7
2500000	2.26	-6.1
2626000	2.35	30.6
2750000	3.17	53.83
3000000	5.37	72.2
4000000	14.45	84.8
5000000	23.14	85.1
10000000	17.8	84.5

Table E.4. Three-wire CM impedance for a Δ-connected, 100 HP, 460 V motor

f (Hz)	Z (Ω)	Theta (degrees)
100	73000	-88.46
200	36900	-88.64
500	14930	-88.85
1000	7530	-89
2000	3790	-89.05
5000	1530	-89.1
10000	766.4	-89.02
20000	382.48	-88.71
50000	147.69	-86.8
60000	120.76	-85.76
75000	93.37	-83.66
100000	65.52	-78
120000	51.95	-70.47
150000	43.44	-52.12
160000	44.35	-45.93
200000	58.2	-41.1
240000	60.73	-55.1
250000	59	-58.1
300000	48	-67.2
400000	34.13	-70.19
500000	27.4	-70.2
800000	16.51	-74.6
1000000	11.35	-73.3
1200000	8.1	-69.6
1500000	4.84	-57.4
1600000	4	-52.38
1700000	3.19	-45.6
1800000	2.44	-34.1
1850000	2.13	-25.6
1900000	1.9	-14.8
1950000	1.75	-1.8
2000000	1.71	12.6
2100000	1.95	39.1
2200000	2.5	56.3
2400000	3.9	72
2500000	4.64	75.6
3000000	8.25	83.2
4000000	15.03	86.5
5000000	22.3	86.9
10000000	66	84.5

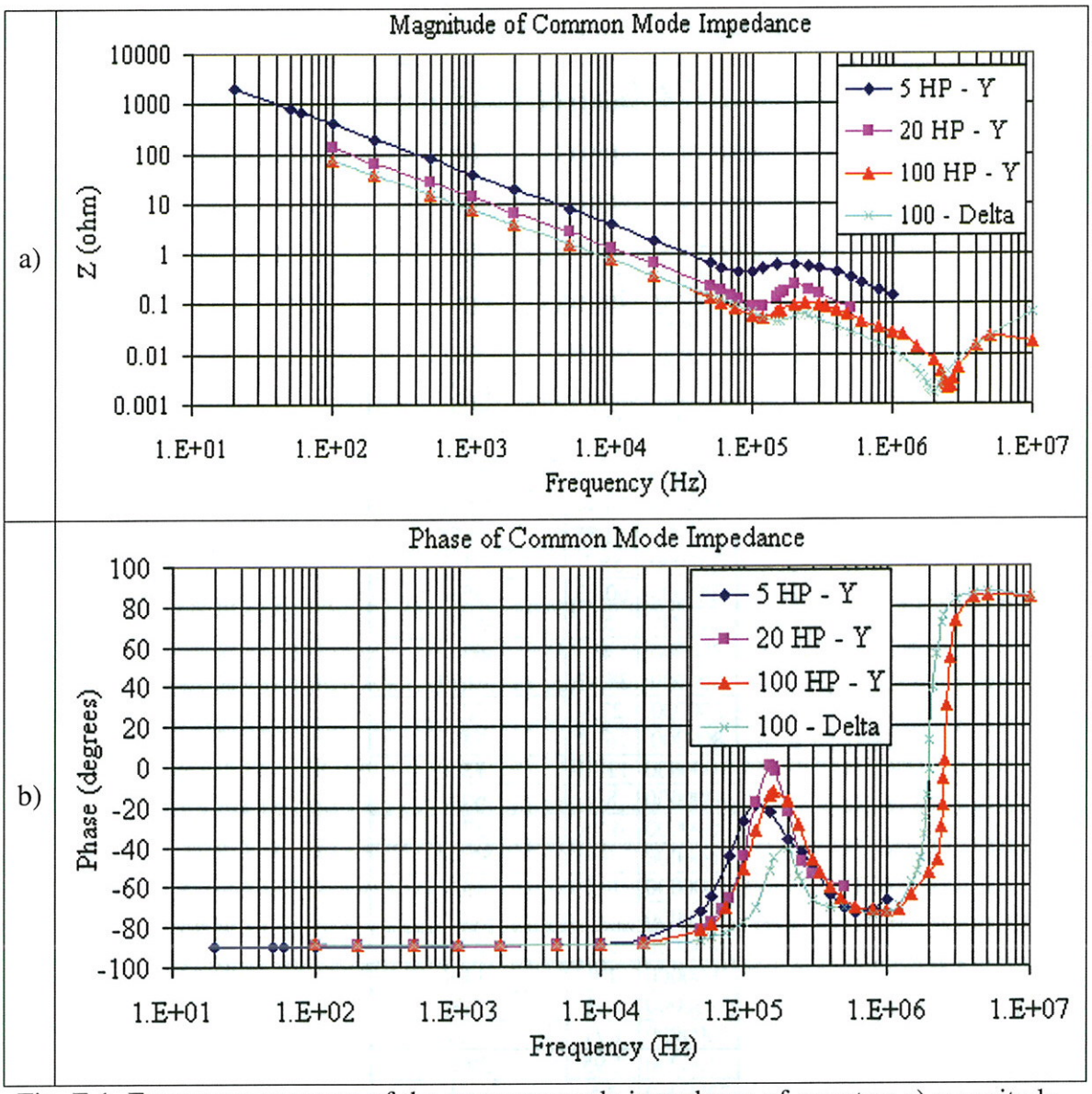

Fig. E.1. Frequency response of the common mode impedance of a motor: a) magnitude, b) phase

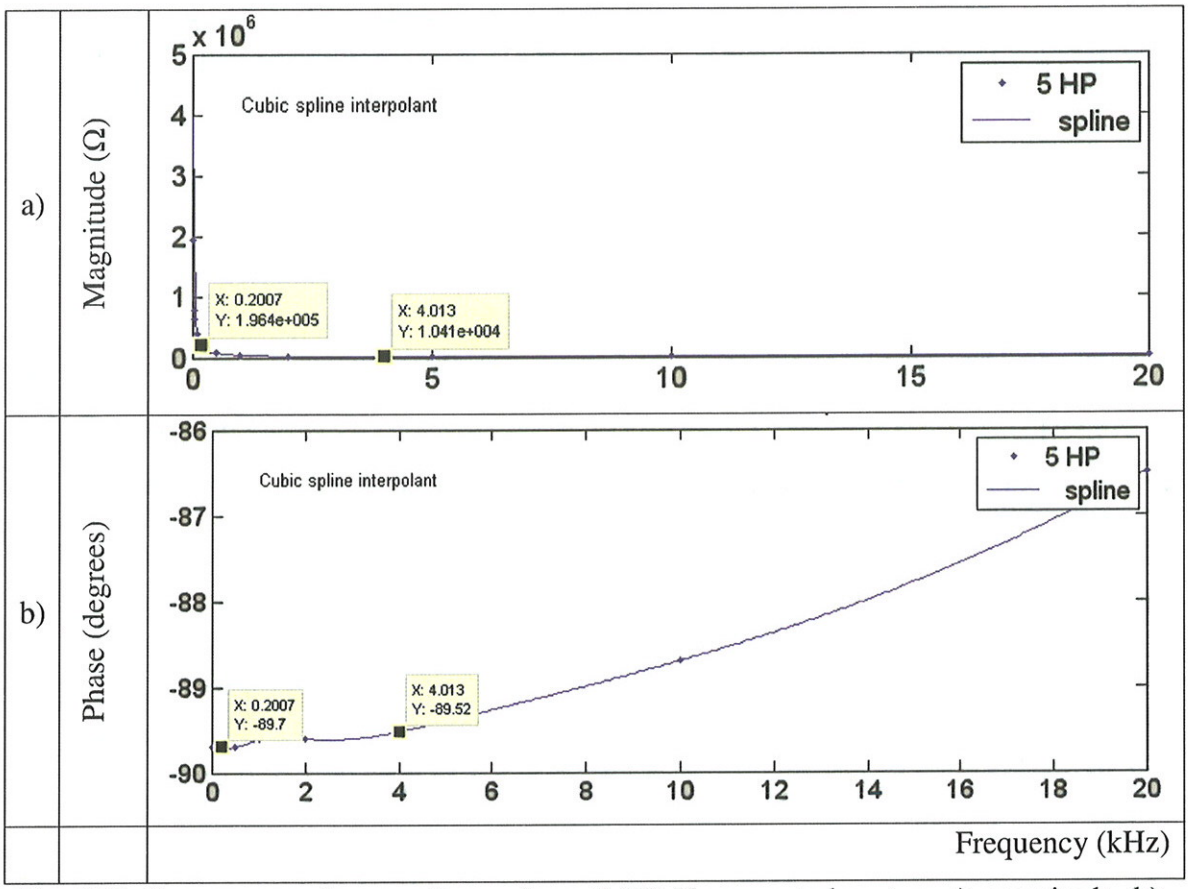

Fig. E.2. Common mode capacitance for a 5 HP Y-connected motor: a) magnitude, b) phase

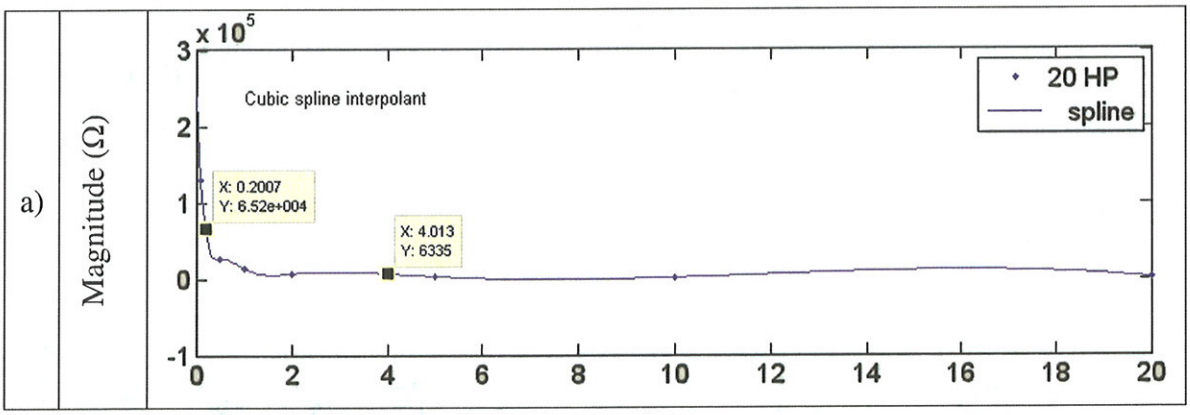

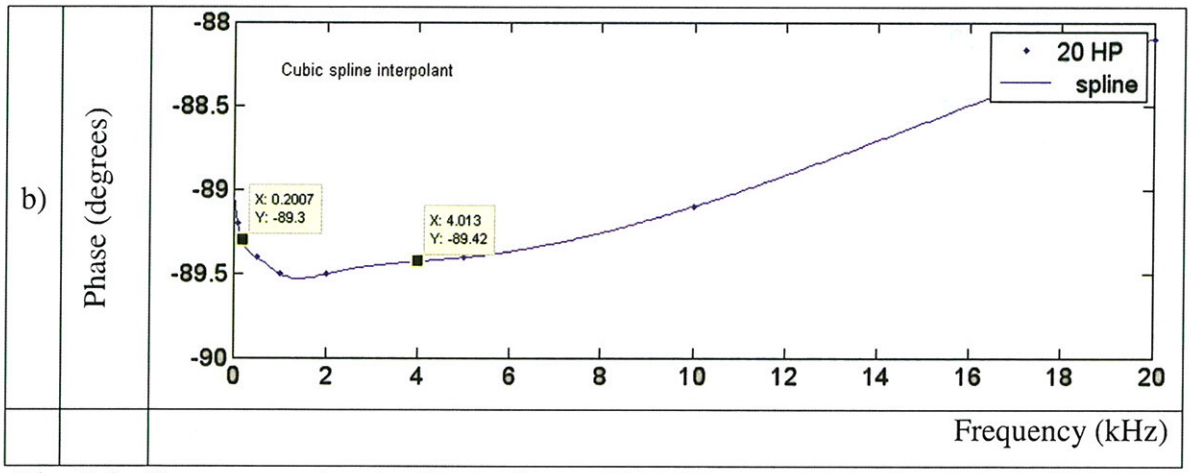

Fig. E.3. Common mode capacitance for a 20 HP Y-connected motor: a) magnitude, b) phase

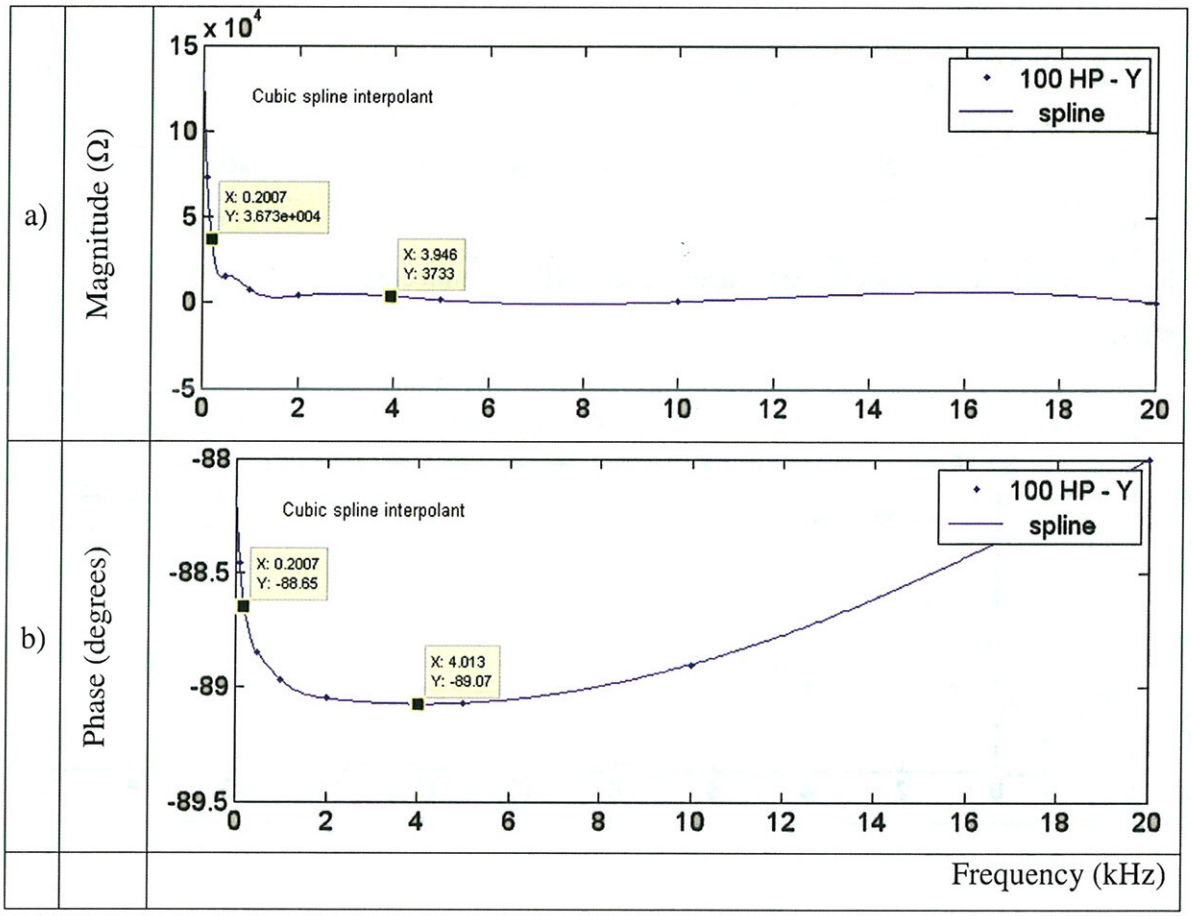

Fig. E.4. Common mode capacitance for a 100 HP Y-connected motor: a) magnitude, b) phase

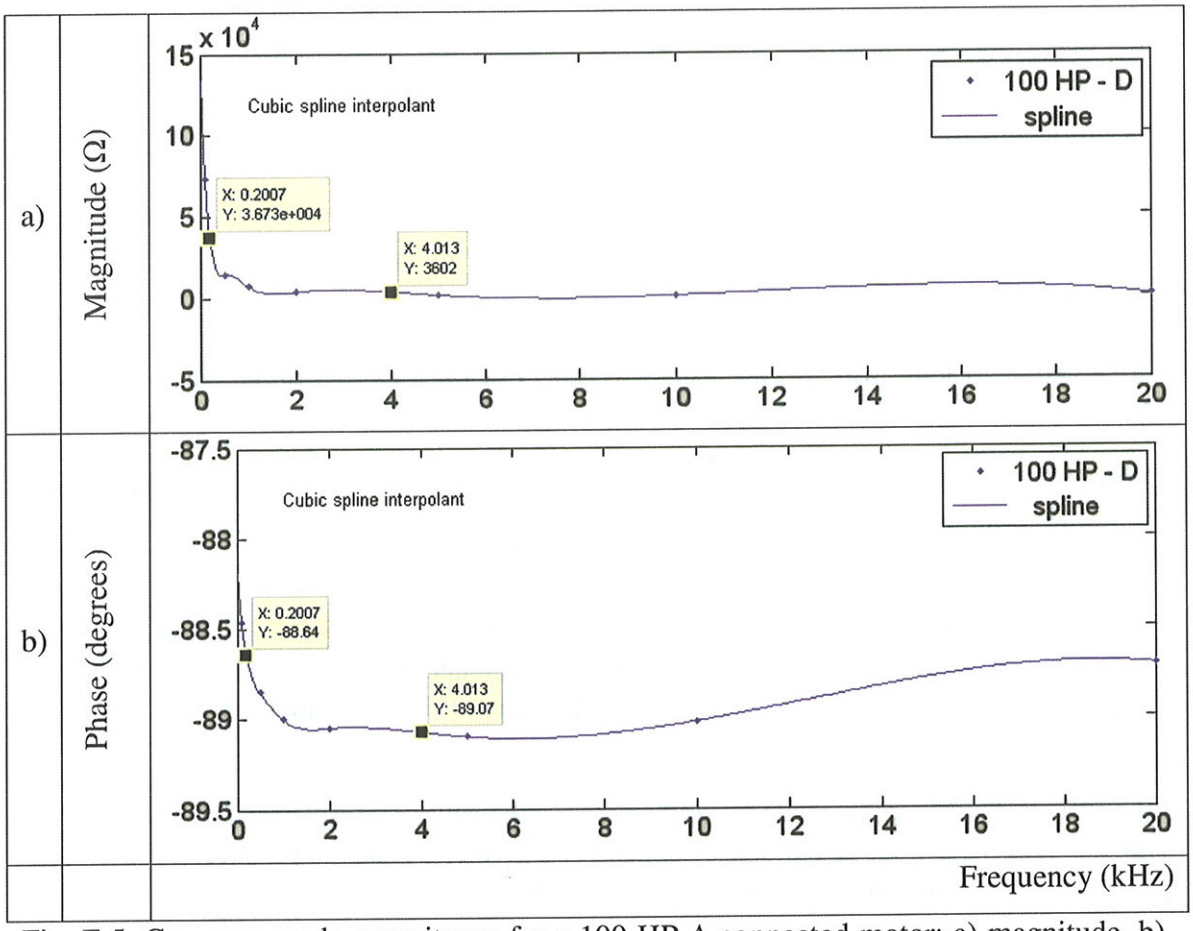

Fig. E.5. Common mode capacitance for a 100 HP Δ-connected motor: a) magnitude, b) phase

Table E.1. Common mode impedances for different motors

	5 HP motor (Y)		**20 HP motor (Y)**		**100 HP motor (Y)**		**100 HP motor (Δ)**	
	f=180	**f=4 k**	**f=180**	**f=4 k**	**f=180**	**f=4 k**	**f=180**	**f=4 k**
Z(Ω)	196,400	10,410	65,200	6,335	36,700	3,733	36,700	3,602

Table E.2. Some other calculated motor frames and parasitic capacitance

Motor power (HP)	Parasitic capacitance (nF)
10	21
20	54
30	90
50	150

LIST OF REFERENCES

[1] "SME: Mining Enginering Handbook," Society for Mining Metallurgy & Exploration; 2nd revised edition, Apr 20th, 1992

[2] H. L. Floyd II, B.J. Nenninger, "Personnel safety and plant reliability considerations in the selection and use of voltage test instruments," IEEE Transaction on Industry Applications, Vol 33, Iss 2, Mar/Apr 1997, pp 367-373

[3] W.G. Zanardelli, E.G. Strangas, and S. Aviyente, "Identification of Intermittent Electrical and Mechanical Faults in Permanent-Magnet AC Drives Based on Time–Frequency Analysis," IEEE Transactions on Industry Applications, Vol 43, No 4, Jul/Aug 2007

[4] M. Valdes, T. Papallo, B. Premerlani, "Finding Fault - Locating a ground fault in low-voltage, high-resistance grounded systems via the single-processor concept for circuit protection", *IEEE Industry Applications Magazine*, Sep/Oct 2007

[5] G. L. Skibinski, B. M. Wood, J. J. Nichols and L. A. Barrios, "Effect of Adjustable Speed Drives on the Operation of Low-Voltage Ground-Fault Indicators," IEEE Transactions on Industry Applications, Vol. 37, No. 5, Sep/Oct 2001

[6] A. Greenwood, "Electrical Transients in Power Systems," 2nd Ed., 1991, Pub. John Wiley and Sons Inc., pp.126-128

[7] J. R. Dunki-Jacobs, "The reality of High-Resistance Grounding," IEEE Tran. Ind. App., Vol IA-13, No.5, Sep/Oct 1977

[8] J. Foster, W. Brown and L. Pryor, "High Resistance Grounding in the Cement Industry – A User's Experience," IEEE Cement Industry Conference, May 19-24, 1985.

[9] "Recommended Practice for the Protection and Coordination of Industrial and Commercial Power Systems," IEEE STANDARD 242-1986, section 7.2.5

[10] National Electrical Code (NEC), Article 250.36 High Impedance Grounded Neutral Systems

[11] W. C. Bloomquist, K. J. Owen, R. L. Gooch, "High-Resistance Grounded Power Systems-Why Not?", IEEE Tran. Ind. App., vol IA-12, No. 6, Nov/Dec 1976

[12] J. R. Holmquist, "An Update of Grounding Experience," Conference Record of 1995 Annual Pulp and Paper Industry Technical Conference, 12-16 Jun 1995, pp 101-106

[13] B. Bridger, "What to know about High Resistance Grounding", EC&M, July 1994, pp 37-41

[14] R. G. Minullin, Yu. Ya. Petrushenko, I. Sh. Fardiev, E. I. Lukin and G. V. Lukina, "Ways to detect single-line-to-ground faults in electricity transmission lines using the location method," Russian Electrical Engineering, Pub. Allerton Press, Inc., Volume 79, Number 12 / December, 2008

[15] Zoran Vrankovic, Lixiang Wei, C. Winterhalter and G. Skibinski, "A Method for Ground Fault Detection and Diagnostics in High Resistance Ground AC Motor Drive System," Innovation Disclosure for Patent Application 2009, Kinetix, Rockwell Automation

[16] Rockwell Automation – Allen Bradley, "E3 and E3 Plus Solid State Overload Relay," www.rockwellautomation.com, 2008

[17] Zhencun Pan, Chengshan Wang, Wei Cong and Fan Zhang, "Single Phase-to-Ground Fault Line Identification and Section Location Method for Non-Effectively Grounded Distribution Systems Based on Signal Injection," Transactions of Tianjin University, Vol. 14, No 2, February, 2008, pp. 92-96

[18] C. Rodríguez Valdez, Tallam, R.M., R.J. Kerkman, "New Frequency-Dependent Model for Cables," IEEE International Conference on Electro/Information Technology, 2008

[19] P.C. Krause, O. Wasynczuk, S. D. Sudhoff, "Analysis of Electric Machinery and Drive Systems," 2nd Ed., 2002, Ed. Wiley-Interscience

[20] A. Hava, "Carrier Based PWM-VSI Drives In The Overmodulation Region," Ph.D. dissertation, University of Wisconsin-Madison, Dec. 1998

[21] D. Leggate, R. J. Kerkman, "Pulse-based dead time compensator for PWM voltage inverters," IEEE Transactions on Industrial Electronics, Vol. 44, No. 2, April 1997, 191-197

[22] Alessandro F. Moreira, Thomas A. Lipo, Giri Venkataramanan, Steffen Bernet, "High-Frequency Modeling for Cable and Induction Motor Overvoltage Studies in Long Cable Drives," *IEEE Transactions on Industry Applications*, Vol. 38, No. 5, Sep/Oct 2002, pp. 1297-1306

[23] G. L. Skibinski, "Design Methodology of a Cable Terminator to Reduce Reflected Voltage on AC motors," *Industry Applications Conference,* Vol. 1, pp. 153 – 161, Oct. 1996

[24] G. Skibinski, R. Kerkman, D. Leggate, J. Pankau, D. Schlegel, "Reflected Wave Modeling Techniques for PWM AC Motor Drives," *Applied Power Electronics Conference (APEC,)* 1998

[25] D.G. Holmes, T.A. Lipo, "Pulse Width Modulation for Power Converters: Principles and Practice," IEEE Press Series on Power Engineering, 2003

[26] Charlotte Wire Catalog, online reference at charlottewire.com

[27] G. Skibinski, R. Tallam, R. Reese, B. Buchholz, R. Lukaszewski, "Common Mode and Differential Mode Analysis of Three Phase Cables for PWM AC Drives," Conference Record of the 2006 IEEE Industry Applications Conference, Oct. 2006, Vol. 2, pp. 880-888

[28] C.M. Ong, "Dynamic Simulation of Electric Machinery: using Matlab/Simulink," Ed. Prentice Hall PTR, 1998, Section 3.5

[29] C. Rodríguez Valdez, R. M. Tallam, R. J. Kerkman, "A New Frequency-Dependent-Model for Electric Conductors", *Integrated Computer-Aided Engineering (ICAE),2008*

[30] K.L. Kaiser, "Electromagnetic Compatibility Handbook," Chapter 12, CRC Press, 1st Ed., 2004

[31] M. Schinkel, S. Weber, S. Guttowski, W. John Fraunhofer, "Efficient HF Modeling and Model Parameterization of Induction Machines for Time and Frequency Domain Simulations," IEEE Applied Power Electronics Conference and Exposition, 2006

[32] M. Liserre, A. Dell'Aquila, F. Blaabjerg, "Genetic algorithm-based design of the active damping for an LCL-filter three-phase active rectifier," IEEE Transactions on Power Electronics, Vol. 19, Iss. 1, Jan. 2004, pp. 76–86

[33] M. Liserre, F. Blaabjerg, S. Hansen, "Design and control of an LCL-filter-based three-phase active rectifier," IEEE Transactions on Industry Applications, Vol. 41, Iss. 5, Sep-Oct 2005, pp. 1281–1291

[34] R. Teodorescu, F. Blaabjerg, U. Borup, M. Liserre, "A new control structure for grid-connected LCL PV inverters with zero steady-state error and selective harmonic compensation," 19th Annual IEEE Applied Power Electronics Conference and Exposition, APEC '04, Vol. 1, 2004, pp. 580-586

[35] F. Blaabjerg, E. Chiarantoni, A. Dell'Aquila, M. Liserre, S. Vegura, "Analysis of the grid side behavior of a LCL-filter based three-phase active rectifier," IEEE International Symposium on Industrial Electronics, ISIE '03, Vol. 2, 9-11 Jun, 2003, pp. 775-780

[36] M. Liserre, F. Blaabjerg, R. Teodorescu, "Grid Impedance Estimation via Excitation of LCL -Filter Resonance," IEEE Transactions on Industry Applications, Vol. 43, Iss. 5, Sep-Oct 2007, pp. 1401 – 1407

[37] Shaotang Chen, T.A.Lipo, D.W. Novotny, "Circulating type motor bearing current in inverter drives," Conference Record of the 1996 IEEE Industry Applications Conference, pp. 162 – 167, Vol. 1, 1996

[38] B. T. Ooi et. al., "An integrated AC drive system using a current-controlled PWM rectifier-inverter link," Conf. Rec. IEEE Industry Applications Society Annual Meeting, 1986, pp. 685-691

[39] R. Wu, S. B. Dewan and G. R. Slemon, "A PWM AC-DC Converter with Fixed Switching Frequency," IEEE Transactions on Industry Applications, Sept./Oct. 1990, pp. 880-885

[40] S. Hiti and D. Boroyevich, "Control of Front-End Three Phase Boost Rectifier," Applied Power Electronics Conference, 1994, pp. 927-933

[41] R. Uhrin and F. Profumo, "Performance Comparison of Output Power Estimators used in AC/DC/AC converters," Conf. Rec. IEEE Industry Applications Society Annual Meeting, 1994, pp. 344-348

[42] T. Baldwin, F. Renovich Jr., L.F. Saunders, D. Lubkeman, "Fault locating in ungrounded and high-resistance grounded systems", *IEEE Transactions on Industry Applications*, Vol. 37, pp. 1152 – 1159, Issue 4, Jul/Aug 2001

[43] A. Hava, R. J. Kerkman and T. A. Lipo, "Dynamic Overmodulation Characteristics of Triangle Intersection PWM Methods," IEEE Industry Application Society Conference, New Orleans, LA, pp. 1520-1528, Oct 2-6, 1997

[44] A. Hava, R. J. Kerkman and T. A. Lipo, "A High Performance Generalized Discontinuous PWM Algorithm," IEEE Applied Power Electronics Conference, Atlanta, GA, Feb 23-27, 1997, pp. 886-891. and IEEE Transactions on Industry Applications, Vol. 34, No. 5, pp 1059-1071, Sep/Oct 1998

[45] A. M. Hava, R. J. Kerkman and T. A. Lipo, "Carrier Based PWM-VSI Overmodulation Strategies: Analysis, Comparison, and Design," IEEE Transactions on Power Electronics, Vol. 13, No. 4, July 1998.

[46] A. M. Hava, R. J. Kerkman and T. A. Lipo, "Simple Analytical and Graphical Methods for Carrier Based PWM VSI Drives," IEEE Transactions on Power Electronics, Vol. 14, No. 1, Jan 1999

[47] K.G. King, "A Three Phase Transistor Class-b Inverter with Sinewave Output and High Efficiency," Inst. Elec. Eng. Conf. Publ. 123, pp 204-209, 1974

[48] H. Van Der Broeck, H. Skudelny and G. Stanke, "Analysis and Realization of a Pulse Width Modulator Based on Voltage Space Vectors," IEEE-IAS Conf. Records, pp 244-251, Denver, USA, 1986

[49] D.C. Aliprantis, "Advances in Electric Machine Modeling and Evolutionary Parameter Identification," Ph.D. Thesis, Purdue 2003

[50] D.S Brereton, "High–resistance grounding for industrial power systems", Distribution, July-Oct 1957

[51] F.K. Fox, H.J. Grotts, and C.H. Tipton, "High-resistance grounding of 2400-Volt delta systems with ground –fault alarm and traceable signal to fault", IEEE Trans Industrial General Applications, Oct, 1965, Vol. IGA-1

[52] F.K. Fox and L.B. McClung, "Ground-fault tests on high-resistance grounded 13.8 kV electrical distribution system of a modern large chemical plant, Part I", IEEE Trans Industrial Applications, Sept/Oct, 1974, Vol. IA-10, pp. 581-600

[53] L.B. McClung and B.W. Whittington, "Ground-fault tests on high-resistance grounded 13.8 kV electrical distribution system of a modern large chemical plant, Part II", IEEE Trans Industrial Applications, Sept/Oct, 1974, Vol. IA-10, pp 601-617

[54] W.C. Bloomquist, K.J. Owen, R.L. Gooch, "High-Resistance Grounded Power Systems – Why Not?", IAS Transactions, Vol. IA-12, Number 6, November/December, 1976, pp. 574-580

[55]J.R. Dunki-Jacobs, "The reality of high resistance grounding", IEEE Trans. Ind. Applications, Vol. IA-13, No.5, pp. 469-475, Sept/Oct., 1977

[56] B. Bridger, "The How's and Why's of High Resistance Grounding", Electrical Construction & Maintenance magazine, April 1978

[57] D.S. Baker, "Charging Current Data for Guess work-Free Design of High Resistance Grounded Systems", IEEE Transactions on Industry Applications Society, Vol. IA-15, No. 2, pp 136-140, March/April, 1979

[58] R.West,"Grounding for Emergency and Standby Power Systems," IEEE Trans. Ind. Application, Vol. IA-15, No. 2, March/April , 1979

[59] B.Bridger, "High resistance grounding", IEEE Transactions Applications Industry, Vol. 1A-19, No. 1 , Jan / Feb, 1983

[60] L. Yu, R. Henriks, "Selection of neutral grounding resistor and ground fault protection for industrial power systems", IEEE PCIC Petro-Chemical Industry Conf, Sept 1991, pp. 147-153

[61] B. Bridger, "What to know about High Resistance Grounding"; EC&M magazine, July, 1994

[62] J. Nelson, P. Sen, "High –resistance grounding of low voltage systems: A standard for the petroleum and chemical industry", IEEE Transactions Industry Applications, Vol. 35, No. 4, pp. 941-948, July/Aug, 1999

[63] J. Nelson, "System grounding and ground fault protection in the petrochemical industry: a need for better understanding", IEEE Trans. Ind. Applications, Vol. 38, No. 6, pp. 1633, Nov/Dec, 2002

[64] T. Baldwin, F. Renovich, L. Saunders, "Directional ground fault indicator for high resistance grounded systems, IEEE Transactions Industry Applications, Vol. 39, No. 2, pp. 325, Mar/April, 2003

[65] T. Novak, J.Basar, J.Sottile, J. Kohler, "The effect of cable capacitance on longwall power systems", IEEE Transactions on Industry Applications Society, Vol. 40.No. 5 , pp. 1406-1412, Sept. / Oct., 2004

[66] D. Moody, V. Shipp, W. Vilcheck, T. Natali, "Hybrid grounding system", IEEE IAS magazine, pp 40-48, May/June, 2004

[67] R. Beltz, I. Peacock, W. Vilcheck, "High resistance ground retrofits in Pulp and paper mills", IEEE Industry Applications Magazine, pp.19-27, March/April, 2001

[68] "Neutral grounding resistors technical information and application guidelines", www.i-gard.com

[69] L. Powell, "Influence of third harmonic circulating currents in selecting grounding devices", IEEE Trans. Ind. Apps., Nov/Dec, 1973, Vol. IA-9

[70] IEC 60364-1 Fourth Edition 2001-08, Electrical Installations of Buildings – Part 1: Fundamental Principles, Assessment of General Characteristics, Definitions.

[71] IEEE Standard 141-1993 (Red Book), Section 7.2.1 to 7.3 Grounding

[72] ANSI/IEEE 141-1993, (red book) Recommended Practice for Electric power distribution fro industrial plants (ANSI) Section 7.2

[73] ANSI/IEEE 142-1991, (green book) Recommended Practice for Grounding of Industrial & Commercial Power Systems. Section 1.4.3

[74] ANSI/IEEE 242-1986, (Buff book) Recommended Practice for protection and Coordination of Industrial and Commercial Power Systems, Section 8.2.5

[75] Insulated Power Cable Engineers Association (IPCEA) Standard No. S-61-401, NEMA WCS (1979), "Thermoplastic Insulated Wire for Transmission and Distribution of Electrical Energy"

[76] IPCEA Standard S-666-24, NEMA WC7-1991, "Cross-Linked Thermosetting Polyethylene Insulated Wire for the Transmission and Distribution of Electrical Energy," Rev. 5, Oct 1976

[77] ANSI/ IEEE standard 32 -1972 (R1990), Terminology and test procedures for neutral grounding devices

[78] E. Bulington, S. Abney, G. Skibinski, "Cable Alternative for PWM AC Drive Applications", IEEE Petroleum & Chemical Conference, 1998

[79] G. Skibinski, Z. Liu, R. van Lieshout, R. Lukaszewski, M. Tuchalski, "Part I: Application Guidelines for High Resistance Grounding of Low Voltage Common AC Bus & Common DC Bus PWM Drive Systems," IEEE IAS Pulp & Paper Industry Conference, 2008

[80] W. Wichakool, J. Paris, Al-Thaddeus Avestruz, S.B. Leeb, "High-Resolution Physically-Windowed Sensors for Power Electronics Applications," Proc. of 25th Applied Power Electronics Conference and Exposition, pp. 580-587, Feb. 2010.

[81] C.F. Wagner and R.D. Evans, "Symmetrical Components: As Applied to the Analysis of Unbalanced Electrical Circuits," Pub. Robert E. Krieger Publishing Company, Inc., 1933, Rep. 1982, Copyright by McGraw-Hill Book Company, Inc.

[82] G.B. Kliman, W.J. Premerlani, R.A. Koegl and D. Hoeweler, "A New Approach to On-line Turn Fault Detection in AC Motors," Conference Record of the IEEE Industry Applications Society, Vol. 1, pp 687-693, 1996

[83] J. Sottile, F.C. Trutt and J.L. Kohler, "Experimental Investigation of On-line Methods for incipient fault detection," Conference Record of the IEEE Industry Applications Society, Vol. 4, pp. 2682-2687, 2000

[84] S.B. Lee, R.M. Tallam and T.G. Habetler, "A Robust Turn-Fault Detection Technique for Induction Machines Based on Monitoring the Sequence-Component Impedance Matrix," Proceedings of the IEEE Power Electronics Specialists Conference, pp. 2217-2223, 2001

[85] Rangarajan M. Tallam, "Current-Based Sensorless Detection of Stator Winding Turn Faults in Induction Machines," Ph.D. Thesis, Georgia Tech, 2001

[86] C.D. Rodríguez-Valdez, R.J. Kerkman, "Method to detect line-to-ground faults," 2010 ECCE

[87] L. Wei, T. Liu, B. Brown, D. Kirschnik, R.J. Kerkman and C.D. Rodríguez-Valdez, "HRG Ground Fault Measurement Method," US patent application, Oct. 2010

[88] D. Busse, J. Erdman, R. J. Kerkman, D. Schlegel and G. Skibinski, "An Evaluation of the Electrostatic Shielded Induction Motor: A Solution for Rotor Shaft Voltage Buildup and Bearing Current," *IEEE Transactions on Industry Applications*, Vol. 33, No. 6, pp. 1563-1570, Nov/Dec 1997

[89] D. Busse, J. Erdman, R. J. Kerkman, D. Schlegel and G. Skibinski, "System Electrical Parameters and Their Effects on Bearing Currents," Transactions on Industry Applications, Vol. 33, No. 2, pp. 577-584, Mar/Apr 1997

[90] D. Busse, J. Erdman, R. J. Kerkman, D. Schlegel and G. Skibinski, "Bearing Currents and Their Relationship to PWM Drives," IEEE Transactions on Power Electronics, Vol. 12, No. 2, pp. 243-252, Mar 1997

[91] G. Preisinger, M. Gröschl and H. Köttritsch, "Prevention of Electric Erosion in Bearings," Evolution 2001, No. 2, p. 21, web page: evolution.skf.com

[92] D. Dahl, D. Sosnowski, D. Schlegel, R.J. Kerkman, M. Pennings, "Field Experience Identifying Electrically Induced Bearing Failures," 2007 IEEE PPIC Conference

[93] L. Asiminoaei, F. Blaabjerg, S. Hansen, "Detection is Key: Harmonic Detection Methods for Active Power Filter Applications," IEEE Industry Applications Magazine, Jul-Aug 2007, pp. 22-33

[94] M. Ciubotaru, R. Teodorescu, F. Blaabjerg, "A New Single-Phase PLL Structure Based on Second Order Generalizad Integrator," PESC, Jun. 2006

[95] D.Cheng, Field and Wave Electromagnetics, Addison Wesley, 1990

[96] A. von Jouanne, D.A. Rendusara, P.N. Enjeti and W. Gray, "Filtering Techniques to Minimize the Effect of Long Motor Leads on PWM Inverter-Fed AC Motor Drive Systems," IEEE Transactions on Industry Applications, Jul/Aug 1996, Vol. 32, No. 4, pp. 919-926

[97] B. Carlson, "Communication Systems," McGraw Hill, Jan 1968, pp. 221-270

[98] B.P. Lathi, "Modern Digital and Analog Communication Systems," Oxford University Press, 3rd Edition, Feb. 1998, chapter 5, pp. 208-250

[99] W.R. Bennett, "New Results in the Calculation of Modulation Products," Bell Systems Tech. J., 1933, pp. 228-243

[100] H.S. Black, "Modulation Theory," Pub. Van Nostrand, N.Y., 1953

[101] S.R. Bowes, "New Sinusoidal Pulsewidth Modulated Inverter," IEE Proc., Vol.122, No. 11, 1975, pp. 1279-1285

[102] S.R. Bowes, "Novel Approach to the Analysis and Synthesis of Modulation Processes in Power Converters," IEE Proc., Vol.122, No. 5, 1975, pp. 507-513

[103] E.W. Weisstein, "Jacobi-Anger Expansion," MathWorld—A Wolfram Web Resource, http://mathworld.wolfram.com/Jacobi-AngerExpansion.html

[104] Hewlett Packard 4284A and 4285 LCR Impedance Analyzer Users Manual, Hewlett Packard Co.